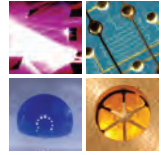


SCHRIFTEN DES INSTITUTS FÜR MIKROSTRUKTURTECHNIK  
AM KARLSRUHER INSTITUT FÜR TECHNOLOGIE (KIT)



Band 42

HOSSEIN DAVOODI

## NMR micro-detectors tailored for multinuclear and electrochemistry lab-on-a-chip applications





Hossein Davoodi

**NMR micro-detectors tailored for multinuclear  
and electrochemistry lab-on-a-chip applications**

Schriften des Instituts für Mikrostrukturtechnik  
am Karlsruher Institut für Technologie (KIT)  
Band 42

Hrsg. Institut für Mikrostrukturtechnik

Eine Übersicht aller bisher in dieser Schriftenreihe  
erschienenen Bände finden Sie am Ende des Buchs.

# **NMR micro-detectors tailored for multinuclear and electrochemistry lab-on-a-chip applications**

by  
Hossein Davoodi

Karlsruher Institut für Technologie  
Institut für Mikrostrukturtechnik

NMR micro-detectors tailored for multinuclear  
and electrochemistry lab-on-a-chip applications

Zur Erlangung des akademischen Grades eines Doktor-Ingenieurs  
von der KIT-Fakultät für Maschinenbau des Karlsruher Instituts für  
Technologie (KIT) genehmigte Dissertation

von Hossein Davoodi

Tag der mündlichen Prüfung: 08. März 2021

Referent: Prof. Dr. Jan G. Korvink

Korreferent: Prof. Dr. Andrew G. Webb

#### Impressum



Karlsruher Institut für Technologie (KIT)  
KIT Scientific Publishing  
Straße am Forum 2  
D-76131 Karlsruhe

KIT Scientific Publishing is a registered trademark  
of Karlsruhe Institute of Technology.  
Reprint using the book cover is not allowed.

[www.ksp.kit.edu](http://www.ksp.kit.edu)



*This document – excluding parts marked otherwise, the cover, pictures and graphs –  
is licensed under a Creative Commons Attribution-Share Alike 4.0 International  
License (CC BY-SA 4.0): <https://creativecommons.org/licenses/by-sa/4.0/deed.en>*



*The cover page is licensed under a Creative Commons  
Attribution-No Derivatives 4.0 International License (CC BY-ND 4.0):  
<https://creativecommons.org/licenses/by-nd/4.0/deed.en>*

Print on Demand 2021 – Gedruckt auf FSC-zertifiziertem Papier

ISSN 1869-5183

ISBN 978-3-7315-1118-2

DOI 10.5445/KSP/1000136014





# Abstract

Each individual isotope has a certain precessing frequency when exposed to an external static magnetic field. Nevertheless, the actual magnetic field, which each nucleus experiences, depends on its chemical and physical environment. Thus, under different environmental conditions, the precessing frequency of the nucleus is slightly different and it can be used to "spy" on the chemical and physical properties of the medium. Nuclear magnetic resonance (NMR) relies on the same principle to detect the precessing frequency, using a radio-frequency (RF) magnetic field interface. Since NMR technique suffers from low sensitivity, a good communication between the sensor (also known as the coil) and the nuclei, as well as efficient signal transfer between the sensor and the rest of signal processing systems, is of great importance. This thesis introduces and studies three novel solutions to improve NMR performance for different applications.

One of NMR bottlenecks is the incompatibility of the technique with conductive elements inside the NMR detection region. Because of their shielding properties, conductive elements have a considerable impact on the magnetic field link between the NMR sensor and the sample. This issue influences a wide range of potentially interesting NMR applications, e.g., electrochemistry reactions, electrophoresis, and dielectrophoresis. As the first sub-topic of this thesis, different potential electrode designs are suggested in order to overcome this challenge. The theoretical and experimental evaluation of these potential solutions for an already-available Helmholtz coil offers two compatible electrode geometries, namely ultra-thin planar disk and side-wall electrodes.

As the second focus point, this thesis tackles multinuclear detection challenges. In a standard NMR system, the detection bandwidth is traded in the favour of power transfer between the sensor and other hardware. However, this thesis considers the other way around. The penalty is evaluated and the sensor geometry is optimised to reduce the cost. It is shown that not only can the broadband detectors push the limits of the total number of detected nuclei but also these detectors exhibit an acceptable sensitivity.

In parallel, a low-cost, broadband solution is introduced to enhance the sensitivity of standard NMR saddle coils when a small sample volume is available. This solution is based on a passive element which focuses the coil field of view at the sample volume. Additionally, this add-on flips the magnetic field so that it penetrates through the sample volume from a different direction. This achievement allows an efficient NMR experiment on the samples with hard geometries, e.g., thin films, thin slices, etc., or with conductive elements.

In summary, this thesis offers three solutions tailored to their specific applications in order to enhance NMR performance. Furthermore, it has been shown how different figures of merit (excitation efficiency, RF field homogeneity, signal-to-noise ratio, and spectral resolution) can benefit from optimising the geometry of the system based on the requirements.



# Zusammenfassung

Das Magnetfeld, das ein Isotopenkern erfährt, bestimmt in Abhängigkeit von seiner chemischen und physikalischen Umgebung seine Präzessionsfrequenz. Diese Frequenz ist daher unter verschiedenen Umgebungsbedingungen leicht unterschiedlich. Dieser wenn auch geringe Unterschied kann dazu genutzt werden, um die chemischen und physikalischen Eigenschaften des Mediums zu ermitteln. Auf genau diesem Prinzip beruht die Kernspinresonanz (Nuclear Magnetic Resonance NMR): Mit Hilfe einer Hochfrequenz (HF-) - Magnetschnittstelle wird die Präzessionsfrequenz der Atomkerne eines Isotops ermittelt. Leider ist die Sensitivität der NMR-Technik gering, so dass eine gute, schnelle und sichere Informationsübertragung zwischen den Isotopenkernen und dem Sensor (auch als Magnetspule bekannt) sowie eine hocheffiziente Signalübertragung zwischen dem Sensor und den weiteren Komponenten des Signalverarbeitungssystems von größter Bedeutung.

In der vorliegenden Arbeit werden drei neuartige Lösungsansätze zur Verbesserung der Leistung der NMR-Technik für verschiedene Anwendungen vorgestellt und detailliert untersucht.

Einer der Hemmschuhe für die NMR-Technik ist die Inkompatibilität von elektrisch leitenden Elementen innerhalb des NMR-Detektionsbereichs. Aufgrund ihrer abschirmenden Eigenschaften weisen elektrisch leitende Elemente einen erheblichen Einfluß auf die Verknüpfung von NMR-Sensor und Probe durch das Magnetfeld auf. Hierdurch wird eine Vielzahl von potentiell interessanten NMR-Anwendungen eingeschränkt, so z.B. elektrochemische Reaktionen, Elektrophorese oder Dielektrophorese.

In einem ersten thematischen Schwerpunkt werden daher verschiedene Elektrodendesigns vorgeschlagen, mit denen der oben genannten Herausforderung möglicherweise begegnet werden kann. Für eine bereits existierende Helmholtz-Magnetspule können mittels theoretischer und experimenteller Bewertung zwei kompatible Elektrodengeometrien ermittelt werden; dies sind zum einen ultra-dünne planare Scheibenelektroden, zum anderen Seitenwand-Elektroden.

Ein zweiter thematischer Schwerpunkt der vorliegenden Arbeit ist die Herausforderung, mehrerer unterschiedliche Kerne parallel zu detektieren. In einem Standard-NMR-Gerät wird üblicherweise die Detektionsbandbreite zu Gunsten einer besseren Leistungsübertragung zwischen dem Sensor und anderer Hardware verringert. In der vorliegenden Arbeit wird der umgekehrte Weg beschritten: Die Herabsetzung der Leistungsfähigkeit bei gleicher Bandbreite wird evaluiert und anschließend die Sensorgeometrie optimiert, um auf diese Weise eine höhere Detektionsqualität zu erzielen und gleichzeitig die Kosten zu reduzieren. Es wird gezeigt, dass mit den verwendeten Breitbanddetektoren nicht nur die Anzahl der detektierbaren Kerne gesteigert werden kann sondern dass diese Detektoren gleichzeitig auch eine akzeptable Sensitivität aufweisen. Parallel zu den genannten Themenschwerpunkten wird eine kostengünstige Lösung für Standard-NMR-Sattelspulen eingeführt, die es erlaubt, die Sensitivität des NMR-Systems bei einem kleinen vorliegenden Probenvolumen zu erhöhen. Diese Lösung basiert hierzu auf einem passiven Element, welches das Sichtfeld der Spule auf das Probenvolumen fokussiert. Dieses zusätzliche Element dreht hierbei das Magnetfeld, so dass das Probenvolumen aus einer anderen Richtung als zuvor durchdrungen wird. Das Ergebnis dieser Technologie ist eine Steigerung der Effizienz der NMR-Experimente für Proben mit festen Geometrien wie z.B. dünne Filme, dünne Scheiben oder leitfähige Elemente. Zusammenfassend werden daher mit der vorliegenden Arbeit drei spezifische Lösungsvorschläge für spezielle Anwendungen gezeigt, mit denen sich jeweils die NMR-Leistung steigern läßt. Darüber hinaus wurde gezeigt, dass und in welcher Weise verschiedene NMR-Leistungsmerkmale (Erregungseffizienz, RF-Feldhomogenität, Signal-Rausch-Verhältnis und spektrale Auflösung) von einer

Optimierung der Geometrie des Systems auf die jeweiligen Anwendungsanforderungen profitieren können.



# Nomenclatures

## Abbreviations

<i>2D</i>	Two Dimensional
<i>3D</i>	Three Dimensional
<i>LC</i>	An electric circuit consisting of an inductor and a capacitor
<i>LCC</i>	An electric circuit consisting of an inductor and two capacitors.
<i>ppb</i>	Part per billion
<i>ppm</i>	Part per million
$\mu$ TAS	Micro total analysis system
ADC	Analogue to digital converter
CS	Chitosan
DNP	Dynamic nuclear polarisation
EC	Electro-chemistry
EMF	Electromagnetic force
FEM	Finite element method
FID	Free induction decay
FLASH	Fast low-angle shot
FOM	Figure of merit
FOV	Field of view
FWHM	Peak width at its half-height
GE	Gradient echo
HF	High frequency
HH	Helmholtz
LF	Low frequency
LL	Lenz lens
LNA	Low noise amplifier

LOC	Lab on a chip
LOD	Limit of detection
MEMS	Micro electro-mechanical system
MF	Middle frequency
MRI	Magnetic resonance imaging
nLOD	normalised limit of detection
NMR	Nuclear magnetic resonance
PCB	Printed circuit board
PVD	Physical vapour deposition
RF	Radio frequency
ROI	Region of interest
SNR	Signal to noise ratio
TE	Echo time
TR	Relaxation time

## Constants

$\epsilon_0$	Vacuum permittivity
$\mu_0$	Vacuum permeability
$h$	Planck constant
$k$	Boltzmann constant

## Symbols

$\alpha$	Wave attenuation constant
$\beta$	Wave phase constant
$\chi$	Magnetic susceptibility
$\delta$	Skin depth
$\epsilon_r$	Relative permittivity
$\Gamma$	Wave propagation constant
$\gamma$	Gyromagnetic ratio
$\lambda$	Wavelength
$\mu_r$	Relative magnetic permeability
$\omega_0$	Larmor frequency

---

$\rho$	Specific electrical resistance
$\sigma$	Chemical shift
$\tau_{\pi/2}$	90° pulse width
$\vec{\mu}$	Magnetic moment
$\vec{S}$	Spin angular momentum
$\xi$	Induced voltage in the coil
$B_0$	Static magnetic field
$B_1$	RF magnetic field
$I$	Nuclear spin
$m$	Magnetic quantum number
$M_0$	Net magnetisation
$Q$	Quality factor
$S_{ij}$	S-parameter
$T$	Temperature
$T_1$	Longitudinal (spin-lattice) relaxation time constant
$T_2$	Spin-spin relaxation time constant





# Contents

<b>Abstract</b> . . . . .	<b>i</b>
<b>Zusammenfassung</b> . . . . .	<b>iii</b>
<b>Nomenclatures</b> . . . . .	<b>vii</b>
<b>1 Introduction</b> . . . . .	<b>1</b>
1.1 Motivation . . . . .	1
1.2 Thesis outline . . . . .	2
1.3 Publications . . . . .	3
1.3.1 In the scope of this thesis . . . . .	3
1.3.2 Side projects . . . . .	5
<b>2 Fundamentals</b> . . . . .	<b>7</b>
2.1 Overview . . . . .	7
2.2 Nuclear magnetic resonance principles . . . . .	8
2.2.1 NMR hardware . . . . .	15
2.2.2 MRI . . . . .	16
2.3 NMR figures of merit . . . . .	17
2.3.1 Excitation efficiency . . . . .	18
2.3.2 RF field uniformity . . . . .	19
2.3.3 Relative SNR . . . . .	19
2.3.4 Spectral resolution . . . . .	20
2.4 Miniaturisation . . . . .	20

2.5	Multinuclear NMR . . . . .	24
2.5.1	Multiresonant NMR detectors . . . . .	27
2.5.2	Broadband NMR detectors . . . . .	42
<b>3</b>	<b>Microfluidic platforms for <i>in situ</i> electrochemistry . . . . .</b>	<b>49</b>
3.1	Overview . . . . .	49
3.2	Introduction . . . . .	50
3.2.1	Experimental set-up . . . . .	53
3.2.2	Susceptibility challenges in micro-NMR . . . . .	54
3.2.3	RF field challenges in micro-NMR . . . . .	55
3.3	Theory . . . . .	56
3.3.1	Selection of the insert geometry . . . . .	56
3.3.2	Simulation settings . . . . .	59
3.3.3	Simulation results . . . . .	63
3.3.4	Post-processing the simulation data . . . . .	66
3.3.5	Evaluation of different configurations . . . . .	67
3.4	Fabrication . . . . .	69
3.4.1	Electrode-free insert . . . . .	70
3.4.2	Planar-electrode inserts . . . . .	71
3.4.3	Sidewall-electrode inserts . . . . .	73
3.5	Characterisation . . . . .	77
3.5.1	Sample preparation . . . . .	78
3.5.2	NMR . . . . .	78
3.5.3	MRI . . . . .	80
3.6	Application . . . . .	83
3.6.1	Monitoring <i>in situ</i> CS electrodeposition . . . . .	85
3.6.2	Multiplexed sensing . . . . .	87
3.7	Discussion and conclusion . . . . .	88
3.7.1	Challenges . . . . .	90
3.7.2	Suggestions . . . . .	90

---

<b>4</b>	<b>Broadband spiral micro-coils</b>	<b>93</b>
4.1	Overview	93
4.2	Introduction	94
4.2.1	Experimental set-up	96
4.3	Theory	97
4.3.1	Figures of merit	98
4.3.2	Pre-adjustments	102
4.3.3	Coil geometry optimisation	104
4.3.4	Microfluidics channel design	110
4.4	Fabrication	112
4.5	Characterisation	116
4.5.1	Benchtop measurements	116
4.5.2	MRI measurements	117
4.5.3	NMR measurements	119
4.6	Discussion and conclusion	128
4.6.1	Challenges and suggestions	128
<b>5</b>	<b>Broadband NMR stripline</b>	<b>131</b>
5.1	Overview	131
5.2	Introduction	132
5.2.1	Experimental set-up	134
5.3	Theory	135
5.3.1	Working principle of Lenz lenses	135
5.3.2	Figures of merit	137
5.3.3	Pre-adjustments	138
5.3.4	Geometry optimisation	139
5.4	Fabrication and assembly	144
5.4.1	PCB	144
5.4.2	Membrane	144
5.4.3	Holder	144

5.5	Characterisation . . . . .	145
5.5.1	Experiment configuration . . . . .	145
5.5.2	MRI results . . . . .	146
5.6	Discussion and conclusion . . . . .	147
5.6.1	Challenges . . . . .	148
5.6.2	Suggestions . . . . .	149
<b>6</b>	<b>Conclusion and outlook . . . . .</b>	<b>151</b>
6.1	Conclusion . . . . .	151
6.2	Outlook . . . . .	152
	<b>Bibliography . . . . .</b>	<b>155</b>
	<b>Publications . . . . .</b>	<b>183</b>
	<b>List of Figures . . . . .</b>	<b>185</b>
	<b>List of Tables . . . . .</b>	<b>187</b>
	<b>Appendix . . . . .</b>	<b>189</b>
A1	Material properties . . . . .	189
A2	Fabrication process details . . . . .	190
A3	Technical drawings . . . . .	193
A4	Matlab codes . . . . .	195
A5	RF field distribution for different electrode geometries . . . . .	200
A6	RF field distribution of the broadband spiral coil . . . . .	201
A7	Benchmarking experiments on borate-glucose complex . . . . .	202
	<b>Acknowledgement . . . . .</b>	<b>205</b>

# 1 Introduction

## 1.1 Motivation

Nuclear magnetic resonance (NMR) is the most powerful method for molecular structure elucidation and identification. Amongst other applications, investigation of proteins is one of the most interesting topics in molecular biology. Despite the popularity of protein-NMR methods, in these experiments, proteins do not experience the same situations as their living environment since the sample is an "unrealistically" large volume of an "artificially" concentrated medium. In fact, the investigation of the proteins in their "normal" life is still an open challenge because of several technical obstacles. The most crucial ones, to be overcome, are: i) a protein-friendly environment being maintained at the NMR field of view; ii) the detector geometry being compatible with the small-volume sample size; iii) the detector being capable of detecting several nuclei; iv) the detector offering good sensitivity and spectral resolution.

Chitosan gel is proved a suitable soft matter to host the proteins and localise that at the region of interest. Besides, chitosan can undergo gel-sol transition with control over the pH of the sample. It can be achieved using a pair of electrodes and applying an electric field. As the result, chitosan gel can be deposited. Relying on this feature, a lab-on-a-chip system consisting of a microfluidic environment equipped with addressable electrodes is required. Presence of the electrodes at the region of interest introduces shielding and susceptibility distortions, which undermines the detection performance. As the first objective of this work, such a lab-on-a-chip system for NMR application is considered in order to study and evaluate its NMR compatibility and find the best solutions, accordingly.

In parallel, the second objective of the work is to design and implement a micro-detector to detect multiple nuclei required for protein studies. The detector should consist of a coil and microfluidics to enable handling and analysis of micro-samples. Considering challenges arising when micro-coils are employed for multinuclear detection and the constraints imposed by the NMR sensitivity, a thorough study and analysis of different options seems necessary to select the best one. The potential solutions should be evaluated at different frequencies corresponding to different nuclei.

Having the final goal in mind, the main contribution of this research is to lay the ground for protein NMR application by studying and evaluating different building blocks individually and to pave the road for further progress in these directions. It is worth mentioning that the findings and devices, introduced here, are not limited to the protein applications but can be readily employed for several other applications, e.g., studying energy storage devices using NMR.

## 1.2 Thesis outline

This thesis consists of six chapters. While the first (current) chapter introduces the thesis, the second chapter presents a brief background about the nuclear magnetic resonance with a more in-depth discussion on the miniaturisation and the multi-nuclear NMR detection techniques. The next three chapters are (almost) independent discussions about three sub-projects. Each one of these chapters starts with a short introduction and continues with the theoretical and experimental analysis of the devices. The third chapter studies a lab-on-a-chip platform, compatible with NMR, in order to immobilise and analyse chitosan as the host for the enzymes and biological samples. Chapter four and five study two types of detectors enabling multinuclear detection, being compatible with microfluidic channels. The thesis is concluded in the sixth chapter with a brief discussion on the achievement of this work and giving an outlook.

## 1.3 Publications

### 1.3.1 In the scope of this thesis

The results relevant to the main subject of this thesis are concluded in six publications

#### **Broadband and multi-resonant sensors for NMR [HD1]:**

*Journal:* Progress in Nuclear Magnetic Resonance Spectroscopy (PN-MRS) 2019- Elsevier

*Authorship:* Lead author

*Content:* This article reviews all the published literature, addressing multi-nuclear NMR detection, employing single coil and from the hardware point-of-view. In addition, this work gives a thorough study of the topologies and methods implemented in the literature and categorise them, accordingly. The micro-coil based multi-nuclear NMR has been also studied by highlighting the differences between micro and macro regimes and providing a detailed analysis of the state-of-the-art.

*Contributions:* Conceptualisation, data curation, formal analysis, investigation, visualisation, writing.

#### **An NMR-compatible microfluidic platform enabling *in situ* electrochemistry [HD2]:**

*Journal:* Lab on a Chip (LoC) 2020- Royal Society of Chemistry (RSC)

*Authorship:* Lead author

*Content:* This article studies different solutions to integrate the metallic electrodes, required for electrochemistry experiments, inside an NMR detection zone for a micro-NMR applications. Based on the simulation toolkit introduced in this paper, different electrode geometries are evaluated. Experimental analysis was then performed on a selection of geometries, which exhibit the best performance based on the simulation results. According to both simulation and measurements, the sidewall electrodes show the best performance.

*Contributions:* Conceptualisation, data curation, formal analysis, investigation, software, validation, visualisation, writing.

**Untuned broadband spiral micro-coils achieve sensitive multi-nuclear NMR TX/RX from microfluidic samples [HD3]:**

*Journal:* Scientific Reports 2020- Springer Nature

*Authorship:* Lead author

*Content:* This paper starts with a comprehensive analysis of the spiral coils for the broadband applications. The optimum geometry of the coil is found based on the simulation results and a detector was fabricated accordingly. The performance of the system was verified experimentally at seven different frequencies.

*Contributions:* Conceptualisation, data curation, formal analysis, investigation, software, validation, visualisation, writing.

**Broadband NMR stripline [HD4]:**

*Publication:* European Union Patent-2020

*Authorship:* Co-inventor

*Content:* This patent introduces a new type of add-ons for the standard NMR detectors which enhances NMR sensitivity for micro-samples. In additions, this add-on flips the field at the detection region. Several NMR applications, e.g., energy storage, thin film, can benefit from this novel feature.

*Contributions:* Conceptualisation, data curation, formal analysis, investigation, software, validation, visualisation, writing.

**Real-Time NMR Monitoring of Spatially Segregated Enzymatic Reactions in Multilayered Hydrogel Assemblies [HD5]:**

*Journal:* Angewandte Chemie 2020- Wiley

*Authorship:* Third author

*Content:* This paper employs the electrochemistry lab-on-a-chip systems to form a multi-layered chitosan hydrogel assembly together with



immobilised enzymes in different layers. Accordingly, simultaneous monitoring of a multiple enzymatic process was achieved employing NMR spectroscopy.

*Contributions:* Data curation, investigation, software, validation, writing.

### 1.3.2 Side projects

Within the course of the Ph.D. career, multiple collaborations were established. These collaborations led to three peer-reviewed publications.

#### **A non-resonant kinetic energy harvester for bioimplantable applications**

[HD6]:

*Journal:* Micromachines 2019-MDPI

*Authorship:* Fifth author

*Content:* In this paper, design and verification of a linear non-resonant kinetic energy harvester for implantable devices are discussed. The energy harvester employs coils and permanent magnets to convert motion to the electrical signal.

*Contributions:* Formal analysis, investigation, validation.

#### **A sub-cm<sup>3</sup> energy harvester for in-vivo biosensors [HD7]:**

*Journal:* Microelectronic Engineering 2019-Elsevier

*Authorship:* Third author

*Content:* This article reports the characterisation of the kinetic energy harvester. The performance of the device installed on a linear shaker was studied in the first step. In the next step, the device was employed for an *in vivo* characterisation by embedding it on a wrist band and for different activities.

*Contributions:* Formal analysis, investigation, validation.

#### **Characterization of a wireless vacuum sensor prototype based on the SAW-Pirani principle [HD8]:**

*Journal:* Processes 2020-MDPI

*Authorship:* Sixth author

*Content:* This paper discusses a wireless vacuum microsensors employing both Pirani principle and surface acoustic waves (SAW) to enhance the range and sensitivity. System performance was studied at different configurations. The system was utilised to sense pressures within the range of 0.9–100000 Pa.

*Contributions:* Fabrication.

## 2 Fundamentals

### 2.1 Overview

Nuclear magnetic resonance (NMR) is a versatile technique, reporting the interaction of nuclear spins when exposed to a static magnetic field. The non-destructive nature of this technique makes it a method of choice, especially when an ongoing process is to be monitored. Chemical specificity and quantitative features of NMR are the other aspects which boost the popularity of this method amongst different spectroscopy techniques.

This chapter provides a brief theoretical overview of NMR. This discussion sets the stage for the successive chapters. Therefore, details are provided as much as required for the rest of the discussion. The discussion in Section 2.2 is founded based on the several reference books in the NMR field, e.g., *Biomedical magnetic resonance technology* by D. I. Hoult *et al.* [1], *Spin dynamics* by M. H. Levitt [2], *NMR probeheads for biophysical and biomedical experiments* by J. Mispelter *et al.*, [3], as well as several articles by D. I. Hoult *et al.* [4–8]. The section continues with introducing NMR hardware, signal flow chain, and the magnetic resonance imaging (MRI) principles.

As a basis for evaluation and optimisation of the NMR detectors, four figures of merit are presented and discussed in Section 2.3. As another focus point of this thesis, miniaturisation of the sample and coil are addressed in Section 2.4 by briefly reviewing the topic and listing the pros and cons of the technique. A major portion of this section is formulated based on the review papers by Webb [9, 10], Kentgens *et al.* [11], Fratila *et al.* [12], and Badilita *et al.* [13].

In Section 2.5, multinuclear detection techniques are critically analysed as the third focus point of the thesis. This subsection is based on a review pa-

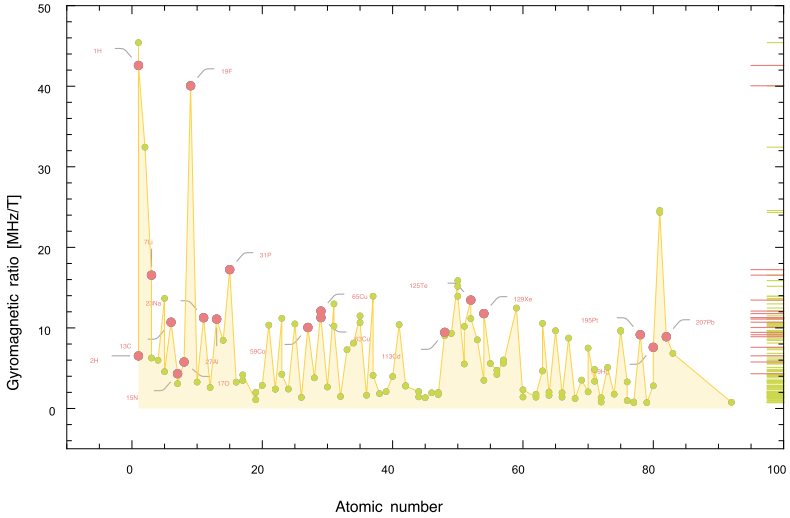
per, we have published in **Progress in Nuclear Magnetic Resonance Spectroscopy (Elsevier)** journal [HD1]. This study has been also presented in **Euroismar 2019** as a poster contribution.

## 2.2 Nuclear magnetic resonance principles

Atoms are the main building blocks of the matter. They either combine as molecules or develop an ensemble of atoms which form a macroscopic structure. An atom consists of electrons, protons, and neutrons. While protons and neutrons are densely packed in the nucleus, electrons are orbiting on certain trajectories around the nucleus. Distribution of electrons are influenced by the bonds to the other atoms, but the nucleus stays very much the same in normal conditions (ignoring high power irradiation or radio-active processes). Different isotopes have different combinations of protons and neutrons and, therefore, exhibit different properties, i.e., mass, charge, spin angular momentum ( $\vec{S}$ ), and magnetic moment ( $\vec{\mu}$ ). Mass and charge of the nuclei affect the physical and chemical properties of the atoms and molecules. Hence, these two can be measured and observed easily. The latter two are more difficult to identify since they are not involved in the macroscopic physical and chemical properties of the atoms and molecules. This fact also means that manipulating the spin or magnetic moment of an atom do not affect the chemical and physical properties of the atoms and atom/molecule maintains its usual behaviour when those properties are being measured. The spin and the magnetic moment are inter-dependent and observing one of those can lead to understanding the other one. The relation between the magnetic moment and spin angular momentum can be expressed as

$$\vec{\mu} = \gamma \vec{S} \quad (2.1)$$

where  $\gamma$ , known as the gyromagnetic ratio, is an intrinsic property of the isotope. Figure 2.1 illustrates the gyromagnetic ratio of the NMR active nuclei.

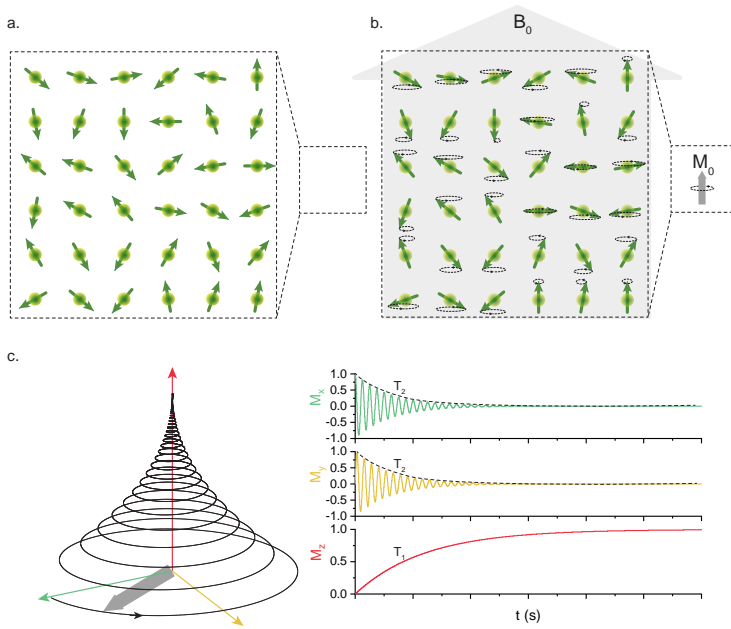


**Figure 2.1:** The gyromagnetic-ratio distribution of the NMR active nuclei. The red dots show the nuclei which have been investigated employing the multinuclear detectors and the green dots correspond to the other NMR-active nuclei. The data were curated from <http://chem.ch.huji.ac.il/nmr/> and <http://web.mit.edu/speclab/www/Facility/nmrfreq.html> (accessed 01.2019) and the figure is reproduced from [HD1].

Each sub-atomic particle (electron, proton, or neutron) exhibits spin  $1/2$ . Based on the combination of its protons and neutrons, each isotope has a certain spin number. This number shows the ground state of the nuclear spin ( $I$ ). Each nuclear spin state consists of  $2 \times I + 1$  substates, which are degenerated at the absence of an external magnetic field. The absolute value of the spin angular momentum can be defined as

$$\vec{S} = \hbar \sqrt{I(I+1)} \quad (2.2)$$

The spin angular momentum of the nucleus is shown with a vector. When the spins degenerate, the spin vectors are randomly distributed and cancel each other in microscopic scales, as illustrated in Figure 2.2.a. In other words, although



**Figure 2.2:** a. Random distribution of the spin vectors when  $B_0 = 0$  results in zero net magnetisation; b. When applying  $B_0$ , the spins of the sample precess around the field direction and also slightly align themselves to the field. It corresponds to a net magnetisation in macroscopic scales. c. After a  $90^\circ$  excitation pulse, the flipped magnetisation returns to its equilibrium by precessing around  $B_0$  and with  $T_1$  and  $T_2$  time constants.

the individual nuclei have certain magnetic moments, the overall magnetisation of the sample is zero.

Applying an external static magnetic field  $B_0$  (by convention, the system of coordinates is defined so that static magnetic field is along  $z$ -axis), splits the substates. This effect is called nuclear Zeeman splitting. The energy difference between two consecutive substates is

$$\Delta E = -\vec{\mu} \cdot \vec{B}_0 = -\gamma \vec{S} \cdot \vec{B}_0 = -\gamma m \hbar B_0 \quad (2.3)$$

where  $m$  is the magnetic quantum number having a value within the range of  $-I$  to  $I$ . The analogy for Zeeman splitting is the precessing of the spin vectors around the static magnetic field axis. This precessing has a certain frequency, known as the Larmor frequency which is defined as

$$\omega_0 = \gamma B_0 \quad (2.4)$$

Although the splitting is about four orders of magnitude smaller than the thermal energy at room temperature, the thermal energy slightly declines the precessing angles of the nuclei. This effect corresponds to the generation of a net magnetisation (see Figure 2.2.b) which is a very slow process comparing to the precessing speed. Assuming  $B_0$  being applied at  $t = 0$ , this phenomenon can be expressed by an exponential equation as

$$M_z(t) = M_0(1 - e^{-\frac{t}{T_1}}) \quad (2.5)$$

where  $M_0$  is the macroscopic magnetisation at the equilibrium and  $T_1$  is the longitudinal (spin-lattice) relaxation time constant. According to Boltzmann distribution for occupation probability of the  $m$ -th substate considering  $N$  nuclei of interest in the sample, the macroscopic magnetisation of the sample can be derived as

$$M_0 = \frac{N\gamma^2\hbar^2 I(I+1)B_0}{3kT} \quad (2.6)$$

where  $k$  is the Boltzmann's constant and  $T$  is the sample temperature. Taking  $^1\text{H}$  as a classic example for a two-state system, the difference between the state populations is  $\sim 40$  ppm in 11.74 T external magnetic field and at 300 K. This minute magnetisation is the main reason behind the low sensitivity of NMR in comparison to the other spectroscopic methods. Assuming a few ml sample volume, the total magnetisation along the static field is about eight orders of magnitude smaller than the external field. Therefore, the magnetisation cannot be measured as long as it is parallel to the external field. In order to measure

the net magnetisation, one can flip it to an orthogonal direction, where the static field has no components and measure the flipped magnetisation. The spins can absorb the oscillating magnetic fields, with the same frequency as the Larmor frequency. The absorbed energy is stored in the tilt angle of the spin vector. Therefore, irradiation of the spins with an RF magnetic field can flip the magnetisation in an orthogonal plane in order to enable measurement of the net magnetisation. For an excitation RF pulse  $\vec{B}_1 = B_x\hat{x} + B_y\hat{y} + B_z\hat{z}$ , the magnetisation can be calculated using the Bloch-equations:

$$\frac{d}{dt} \begin{pmatrix} M_x \\ M_y \\ M_z \end{pmatrix} = \begin{pmatrix} -\frac{1}{T_2} & \gamma B_z & -\gamma B_y \\ -\gamma B_z & -\frac{1}{T_2} & \gamma B_x \\ \gamma B_y & -\gamma B_x & -\frac{1}{T_1} \end{pmatrix} \begin{pmatrix} M_x \\ M_y \\ M_z \end{pmatrix} + \begin{pmatrix} 0 \\ 0 \\ \frac{M_0}{T_1} \end{pmatrix} \quad (2.7)$$

where  $T_2$  is the spin-spin relaxation. Assuming the RF field along the nominal  $y$ -axis, the equations can be simplified. In this case, for an RF field amplitude  $B_1$ , the pulse which flips the spins to  $xy$ -plane is called  $90^\circ$  pulse and its duration is calculated as  $\tau_{90^\circ} = \frac{\pi/2}{\gamma B_1}$ , assuming this time is much shorter than  $T_1$  and  $T_2$ . As soon as the excitation pulse is stopped, the spins release the stored energy by relaxing back to their equilibrium state, i.e., by a similar precessing behaviour, as depicted in Figure 2.2c. Assuming a detector sensitive to the magnetic field fluctuations in  $y$ -axis, the relaxation of the spins can be captured.

Both excitation of the spins and detection of the relaxation can be performed with either one coil or two different coil and based on the Faraday's law of induction. There are different types of coils with different geometries. Without loss of generality, a loop of wire surrounding the spins and with its axis along  $y$ -axis can represent the NMR coils. Based on the geometry and intrinsic properties of the coil, it generates an oscillating magnetic field ( $\vec{B}_{1u}$ ), at its surrounding space, for a unit current applied to its ports. According to the principle of reciprocity, the coil is similarly sensitive to the magnetic field fluctuations in  $y$ -axis and



translates those fluctuations to an electrical signal at its ports. The collected signal can be calculated as

$$\xi(t) = \int \frac{\partial(\vec{B}_{1u} \cdot \vec{M})}{\partial t} dV \quad (2.8)$$

The collected signal, known as the free induction decay (FID), is usually processed and presented in the frequency domain and is called the NMR spectrum. Assuming a perfectly uniform  $B_0$ , all the spins precess with the same frequency and the NMR spectrum is a Lorentzian peak as the result of relaxation. The peak width at half height for this case is  $2/T_2$ .

Nevertheless, several non-idealities contribute to the measurements and introduce deviations to the collected signal. These deviations can report on the environment of the nuclei in the microscopic scale and in a quantitative manner. The deviations can be divided into two groups: the deviations which stem from non-perfect experimental conditions and the deviations which are related to the sample. The main imperfections related to the experimental setup are:

**$B_0$  distortions:** Fluctuations in the external magnetic field are proportionally translated as distortions in the Larmor frequency of the spins. Therefore, the NMR spectrum is a collection of dense peaks. Assuming that the sensitivity of the coil is uniform all over the sample region, the final spectrum is the convolution of Lorentzian peak and  $B_0$  spatial distortions folded in linear dimension.  $B_0$  distortions can be made as a result of original field inhomogeneities, or susceptibility mismatch between different materials. Shim structures are employed in NMR systems to correct the distortions and adjust the line width. In addition, the material boundaries are pushed away from the detection region in order to minimise their effects.

**$B_1$  inhomogeneity:** RF field inhomogeneity induces non-uniform flip angles at different location of the sample. As Equation 2.8 implies, integral of the NMR spectrum depends on the average RF field at the sample region. In longer excitation pulses, this phenomenon corresponds to the dispersion

of the spins and cancellations of the total magnetisation. Besides, the efficiency of some NMR and MRI experiments, e.g., polarisation transfer, diffusion NMR, MRI, peak suppression technique, strongly depend on the RF field homogeneity.

**Noise:** As discussed, the total magnetisation of the sample is very low and the NMR signal is weak. Therefore, noise and signal-to-noise ratio (SNR) are the major concerns in NMR. The thermal noise of the coil and also the sample are the main sources of the noise. In the case of small sample volumes, i.e., micro-samples, the noise of the coil is dominant [14]. In high magnetic fields, the resonance frequency is also high and therefore, skin depth and proximity effects increase the resistance of the coil and accordingly the noise generated by that.

The second group of deviations, which originate from the physical and chemical properties of the sample, can be used to identify it. These deviations can be summarised as follows:

**Chemical shift:** Instead of distortion in the external static field, the structure of the molecules and the electron cloud surrounding the spin can introduce a slight  $B_0$  distortion in microscopic scales. As a matter of fact, NMR is especially useful because of the ability to collect these distortions and depict them as a signal. These distortions usually cause offset in the frequency axis (in part per million-ppm) based on the chemical compound and the electron cloud distribution around the spin under study.

**J-coupling:** The magnetic momentum of the nuclei in the neighbourhood can act as an external magnetic field and distort the electron cloud around the spin under study. In this manner, the neighbourhood nuclei affect the static field, which the spin sees, and indirectly introduce a shift in the peak position. Therefore, this effect is also known as indirect dipole-dipole coupling. J-coupling is independent of the external magnetic field and

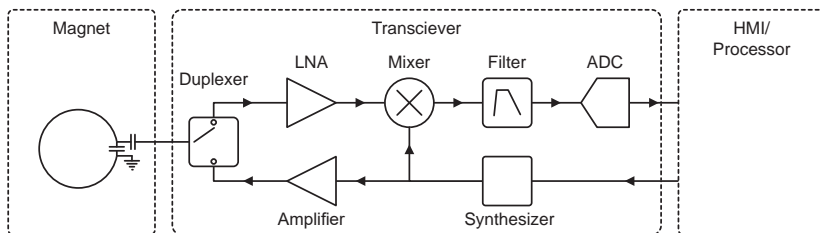
hence is expressed in Hz. This effect results in a collection of peaks known as multiplets.

**Dipole-dipole coupling:** The direct interaction between the magnetic moments of two neighbourhood nuclear spins results in the dipole-dipole coupling. In the isotropic liquids, the secular part of the dipole-dipole coupling is averaged to zero but in anisotropic liquids or the solid-state NMR this effect plays a big role as the structure of the sample is fixed and the interactions do not cancel each other. Magic angle spinning techniques have been developed to exclude these effects from the NMR spectra.

### 2.2.1 NMR hardware

In its very primitive structure, an NMR system requires a static magnetic field, an excitation/detection coil, the transceiver circuits, and the processor to calculate the Fourier transform of the collected signal. These main building blocks of the system are depicted in Figure 2.3. The magnetic field is generated by either a superconducting magnet (for high field NMR) or a set of permanent magnets (for low field NMR). The sample is placed inside the detection zone of the coil, which is connected to the transceiver circuits through an intermediate network. This network, maximising the power transfer rate between the coil and the transceiver, is usually called the tuning/matching network and consists of, at least, two capacitors.

The transceiver consists of several sub-systems. The excitation pulse is generated in the synthesizer according to the data provided through the user interface. This pulse is then directed to the amplifier to adjust its power level. The duplexer connects the output of the amplifier to the coil in the excitation phase so that power is transferred to the coil and excitation is performed. In the receive mode, the collected signal is directed to the low noise amplifier (LNA). LNA boosts the signal amplitude to be robust to the processing steps afterwards. In the next steps, down-conversion and frequency adjustment are performed. The down-conversion is performed by a mixer and with respect to the reference signal



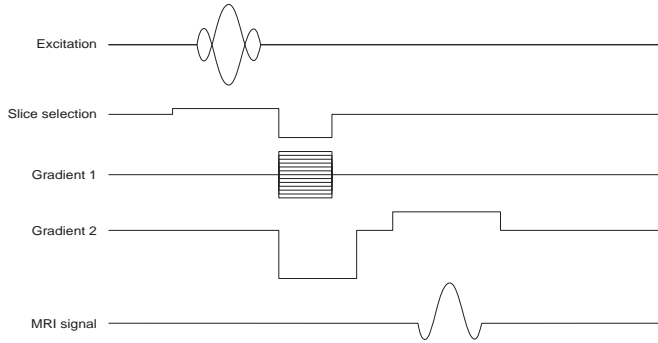
**Figure 2.3:** A simplified NMR experiment setup consisting of the magnet, the transceiver system, and the processing unit. While the coil is inside the magnet, it is usually connected to the transceiver through a tuning/matching network. The transceiver provides the excitation signal for the coil. In the receive mode, the transceiver collects the signal induced into the coil and after some adjustments delivers it to the processor.

being produced by the synthesizer. The result is filtered before digitisation in order to eliminate noise which are out of the detection bandwidth. The digital signal at the output of the ADC is further processed using the processor to calculate its Fourier transform and generate the NMR spectrum.

In a functional NMR system, several other systems, e.g., shimming, lock, are required to ensure accuracy of the measurements.

## 2.2.2 MRI

In an imaging experiment, in addition to the previously mentioned systems and sub-systems, a gradient system is required to generate field gradient in different directions. These field gradients, which add up to the static magnetic field, are used to encode the spatial information in the frequency or collect signal from a certain location in the space. The phase of the signal can also be used as another carrier for the spatial information. By proper adjustment of the gradients, one can select a certain slice in the space, and encode spatial distribution of the sample or  $B_1$  field to a matrix of signals, known as k-space. 2D Fourier transform of the k-space matrix results in the 2D spatial distribution of the sample/ $B_1$  field. Figure 2.4 illustrates a pulse sequence for a simple MRI experiment, known as the Fast low-angle shot (Flash). A certain slice is



**Figure 2.4:** The pulse sequence of a Flash MRI experiment. In this sequence, a slice is selected and by means of two other gradients, frequency and phase encodings are achieved.

selected using the slice selection. By sweeping Gradient 1 and recording the MRI signals, the k-space matrix can be generated. Gradient 2 is employed for dephasing and rephasing the spins.

## 2.3 NMR figures of merit

In an NMR experiment, several different parameters are involved. These parameters can be divided into a few groups: i) parameters depending on the sample, e.g., the gyromagnetic ratio, the total number of spins and their quantum number, the chemical structure of the sample, the relaxation times ( $T_1$  and  $T_2$ ); ii) parameters depending on the experimental conditions, e.g., the external static field  $B_0$  and temperature  $T$ ; iii) parameters depending on the signal processing steps and settings, e.g., the excitation pulse length and shape, the acquisition time, the sampling rate.; iv) parameters depending on the excitation/detection hardware, e.g., the power transfer efficiency between successive blocks, LNA noise figure, quantisation noise.

As a front-end hardware designer, the task of a detector developer is to design the best sensor for the required application and based on the rest of the system. In this thesis, the most important parameters to be considered in a good coil

practice are defined as the NMR figures of merit. The following chapters use these figures of merit considering the specific requirements of each application and NMR setup to study and propose the most suitable designs. These figures of merit are as follows.

### 2.3.1 Excitation efficiency

Considering Bloch-equations (Equation 2.7) and assuming a uniform distribution of the sample all over the sample volume,  $\vec{B}_0$  and  $\vec{B}_1$  along the nominal  $\hat{z}$  and  $\hat{y}$ , respectively, the magnetisation ( $\vec{M}$ ) for any arbitrary sample voxel can be approximated as:

$$\begin{aligned} \vec{M} = M \sin(\omega_0 \tau) \sin(\gamma B_{1u} I_{coil} \tau) \hat{x} + M \cos(\omega_0 \tau) \sin(\gamma B_{1u} I_{coil} \tau) \hat{y} \\ + M \cos(\gamma B_{1u} I_{coil} \tau) \hat{z} \end{aligned} \quad (2.9)$$

where  $B_{1u}$  is the magnetic field generated by the coil per unit applied current for a rectangular excitation pulse power  $P = r_{coil} \times I_{coil}^2$  and the pulse length  $\tau$  being much shorter than  $T_1$  and  $T_2$ .

In the receive mode,  $B_1 = 0$  and the magnetisation vectors return to their steady-state orientation following Equation 2.7. The amplitude of the collected signal can be calculated using Equation 2.8 as:

$$\xi(t) = \overline{B_{1u} \times \sin(\gamma B_{1u} I_{coil} \tau)} \times M \omega_0 \times V_{sample} \times \cos(\omega_0 t) \quad (2.10)$$

assuming  $B_0$  is perfectly homogeneous at the sample volume. For a uniform  $B_1$  distribution, the maximum signal amplitude is achieved when the duration of the excitation pulse is  $\tau = \pi / (2 \times \gamma B_{1u} I_{coil})$ . This value is known as  $90^\circ$  pulse width ( $\tau_{\pi/2}$ ).  $\overline{B_{1u} \times \sin(\gamma B_{1u} I_{coil} \tau_{\pi/2})}$  indicates the average effective RF field at the sample region following a  $\pi/2$  excitation pulse. In presence of  $B_0$  inhomogeneities, the signal is the sum of multiple sinusoidal signals with slightly

different frequencies. By convention, the definition of  $\tau_{\pi/2}$  still holds as the pulse width for which the signal amplitude is maximum.

Accordingly, unless otherwise specified, the excitation efficiency is defined as  $\pi/(2 \times \tau_{\pi/2})$  for 1 W applied power. This value is independent of  $B_0$  and noise performance of the system and shows the ability of the system to convert applied electric power to the RF magnetic field at the sample region.

### 2.3.2 RF field uniformity

By sweeping  $\tau$  and observing the collected signal ( $\xi$ ), the evolution of the NMR signal as a function of the pulse duration is achieved. This signal is known as the nutation signal. Another useful piece of information which can be extracted from the nutation signal is the  $B_1$  uniformity at the sample region. As mentioned for the excitation efficiency, assuming a uniform  $\vec{B}_1$  field and ignoring the spin relaxation time, the relative amplitudes of the collected signals depend on  $\tau$  and signal evolves as a sinusoidal wave with respect to  $\tau$ . However, the inhomogeneity of  $B_1$  field introduces an envelope to the sinusoidal signal. As the result, the signal envelop decays with  $\tau$ . Therefore, the amplitude of the signal corresponding to the  $450^\circ$  flip angle to that of the  $90^\circ$  is considered as the measure for field homogeneity.

### 2.3.3 Relative SNR

The amplitude of the signal following each certain excitation pulse can be achieved from Equation 2.10. The FID excludes the static field distortions, as well as  $T_2$  relaxation. This value corresponds to the area under each certain peak assuming enough distance between successive peaks. Excluding the noise contribution from the sample (which is a valid approximation for micro-samples), the signal-to-noise ratio at the coil's terminal depends on the Johnson noise generated by the coil [15]. Therefore,

$$SNR = \frac{\text{magnitude}(\xi)}{RMS(n_{coil})} = \frac{B_{1u} \times \sin(\gamma B_{1u} I_{coil} \tau_{\pi/2}) \times M \omega_0 \times V_{sample}}{\sqrt{4kTr_{coil}}} \quad (2.11)$$

where  $T$  is the coil temperature,  $k$  is the Boltzmann's constant, and  $r_{coil}$  is the coil resistance at the Larmor frequency. In the current study, SNR for a unit of sample volume is studied and the effect of the Larmor frequency, magnetisation, and coil temperature are excluded from the equation in order to facilitate the evaluation. Accordingly, unless otherwise mentioned, the third figure of merit is defined as the relative SNR. Relative SNR is calculated as:

$$SNR_{rel} = \frac{B_{1u} \times \sin(\gamma B_{1u} I_{coil} \tau_{\pi/2})}{\sqrt{r_{coil}}} \quad (2.12)$$

### 2.3.4 Spectral resolution

The last figure of merit considered here is the spectral resolution. Usually, the spectral resolution is defined based on the full-width half-maximum (FWHM) of the NMR peak. As discussed before, the linewidth depends on both  $B_0$  uniformity and  $T_2$  relaxation. As  $T_2$  relaxation depends on the sample under study, its effect is excluded in our evaluation. Besides, the external magnetic field in the absence of the NMR coil and the sample is presumed to be perfectly homogeneous. Accordingly, the line broadening introduced by  $B_0$  distortions, after considering the coil, the sample holder, and the sample, is considered as the figure of merit.

According to Equation 2.7, the impact of  $B_0$  distortions in different sample voxels depends on the  $B_1$  field at that voxel. It shall be noted that Equation 2.10 does not include  $B_0$  distortions. Therefore, the spectrum of the signal considering the static field perturbations shall be calculated directly from Equation 2.7.

## 2.4 Miniaturisation

Since in an NMR experiment a small fraction of the spins is magnetised, sensitivity is the Achilles' heel of NMR spectroscopy. Considering Equation 2.6, sensitivity can be enhanced by employing a higher  $B_0$  field or performing the experiments using a sample kept at low temperatures. Despite the progress in



superconducting magnets, they still experience several technical limits, e.g., size of the magnet, supplying power to the magnet, stabilisation, cooling down the magnet, superconductor material properties. Therefore, further developments of the high field magnets require even more investments (in terms of both money and time) before being introduced to the market. Moreover, for applications such as human MRI, the maximum frequency is limited due to the safety concerns and higher magnetic fields are not exploitable. Many NMR samples have a melting point much higher than the cryo-temperature. Therefore, reducing the sample temperature requires solid-state NMR experiments which are more complex than the liquid-state NMR. Besides, for the experiments which deal with living samples and organisms or the samples which require a preset temperature, cryo-NMR is not an option.

Another option is to artificially boost the spin polarisation. Nuclear Overhauser effect (NOE) enables the polarisation transfer from a high-gamma nucleus (for example  $^1\text{H}$ ) to a low-gamma nucleus (e.g.  $^{13}\text{C}$ ). In this case, polarisation of the low-gamma nuclei is manipulated to enhance the sensitivity of the NMR experiments [16]. Hyperpolarisation techniques transfer the polarisation from a second system, which is easier to polarise, to nuclei and increase the nuclear polarisation up to 100 %. Dynamic nuclear polarisation (DNP) relies on the polarisation transfer from the electrons to the nucleus. Due to its extremely higher Larmor frequency, electron magnetisation is six orders of magnitude higher than the nuclei [16, 17]. By transferring the electron magnetisation, one can expect more than two orders of magnitudes enhancement in the sensitivity. Optical pumping is another method to manipulate the polarisation. In this method, Alkali metals are exploited to transfer the polarisation of a light source to noble gas atoms, e.g.,  $^{129}\text{Xe}$ ,  $^3\text{He}$ , or semiconductors [16, 17]. Photochemically induced DNP employs photo-excitabile dyes and a light source to trigger a chain reaction and induce a nuclear polarisation [16]. Parahydrogen-induced polarisation transfers parahydrogen spins to the sample [16, 17]. In this case, parahydrogen is achieved by passing the hydrogen isomers through a paramagnetic catalyst.

As an alternative, the noise can be reduced to improve SNR. The most common solution for that is to reduce the temperature of the coil. Cryo-probes aim to reduce the coil temperature but maintain the sample temperature at a certain level. The thermal isolation between the coil and sample degrades both sensitivity of the system and spectral resolution by allowing smaller sample volumes and introducing additional material interfaces. Alternatively, high-temperature superconductive wires can be employed to reduce the coil resistance and noise [10]. It should be noted that especially for the large sample volumes or conductive samples, the sample noise is dominant. Therefore, coil modification cannot be beneficial.

According to the principle of reciprocity, summarised in Equation 2.8, the signal collected from any elementary sample volume depends on the amplitude of the RF magnetic field per unit applied current at the location of the sample. Therefore, by increasing the RF magnetic field per unit current, signal amplitude can be enhanced. For this purpose, a more compact winding is required. The penalties for that are: i) an increase in the resistance of the coil because of the proximity effects and total length of the conductor; ii) a decrease in the self-resonance frequency of the coil because of the longer conductor length and higher inter-turn capacitance. These two side effects increase the power dissipation in the coil and noise, it generates. Besides,  $B_1$  field generated by the coil drops when the detection frequency is higher than the self-resonance frequency.

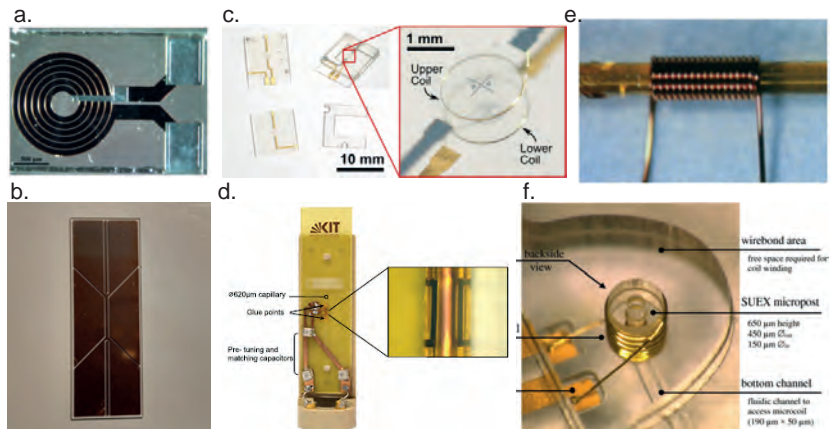
These issues can be accommodated for small sample volumes by miniaturising the coil to fit the sample size. As a result, the total resistance is reduced and the self-resonance frequency is increased. Therefore, miniaturisation helps to increase the magnetic field generated by the coil for a unit applied current. Consequently, SNR benefits from both reduced noise and increased signal amplitude. Nevertheless, the penalty is the SNR per unit sample volume which decreases with the scaling factor. Moreover, compactness of the miniaturised sample and detector results in higher  $B_0$  distortions and degrades the spectral resolution [10, 18, 19]. Immersing the detector and the sample in a susceptibility matched

medium or using zero-susceptibility wires [20] are the potential solutions for spectral resolution enhancement for micro-coils. Nevertheless, both methods result in higher noise levels of the coil. Special shims custom-designed for the samples volume is another potential solution [21].

Although the very first micro-coil was a hand-wound solenoid [22], planar geometries are more favourable because of their compatibility with standard micro-fabrication techniques and integration of microfluidic channels. Korvink *et al.* have developed a semi-automatic technique using ball-wedge wirebonder to generate arbitrary 3D helices being fully compatible with micro-fabrication process [15, 23–28]. Flexible substrates are also another solution which helped to realise micro-coils, e.g., saddle coil [29, 30]. Planar spiral coils are another type of the NMR coils which have been widely studied as micro-coils [31–37]. Stripline coils, which are a subset of the planar geometries, are very wide-spread since they offer high sensitivity, as well as minimised  $B_0$  distortions [18, 38–47]. Some of the most successful designs are collected in Figure 2.5.

In addition to their compact nature, being problematic in terms of  $B_0$  field homogeneity, another major challenge of the micro-coils is associated with their connection to the corresponding circuit, i.e. capacitors. The connection paths have impedances comparable to that of the coil. Therefore, power dissipation and noise contribution of those elements are considerable.

One method to eliminate the conductive tracks is to provide an inductive coupling path for power transfer. In this case, the miniaturised coil is coupled to a secondary coil. The miniaturised coil can be either in the resonant mode to absorb the maximum power from the secondary coil or in the non-resonant mode. Several designs have been proposed according to these concepts, e.g., magic angle spinning coils [25, 28, 48, 49], Lenz-lens structures [50–56]. Additionally, inductive coupling reduces complexity of the circuit around the sample region and enhances spectral resolution. Nonetheless, the coupling between two coils is always smaller than unity which, in turn, results in lower power transfer efficiency, as well as signal amplitude.



**Figure 2.5:** Different geometries of micro-coils reported for NMR applications: a. spiral coil (Reproduced from Ref. [37] with permission from The Royal Society of Chemistry), b. stripline (Reproduced from Ref. [42] with permission from American Chemical Society), c. Helmholtz (Reproduced from Ref. [26] with permission from IOP Publishing), d. saddle (Reproduced from Ref. [29] with permission from Publishing), e. solenoid (Reproduced from Ref. [14] with permission from American Association for the Advancement of Science), f. solenoid with integrated microfluidics (Reproduced from Ref. [27] with permission from Publishing)

Developments of the micro-coils motivated new NMR applications, especially for limited sample volumes or precious samples which were not exploitable by conventional NMR. In addition, from the economical point of view, micro-NMR along with developments in the superconducting magnets and NMR/MRI software is envisioned to unlock new opportunities such as wearable sensors and also the integration of the NMR sensors to the production lines as a quality control methods [57].

## 2.5 Multinuclear NMR

One of the most interesting features of NMR is its ability to address a wide range of isotopes. It allows the user to perform experiments on all NMR-active nuclei in a sample and collect information from different perspectives, corresponding to different isotopes. In addition, some more sophisticated techniques are able

to study the correlation between different nuclei by transferring the polarisation from one kind to another. The decoupling experiments are also helpful to exclude the coupling between two isotopes from the NMR spectrum. All these features are available due to the progress in the NMR hardware. In the front end of this hardware, the coil should be capable of multinuclear detection. As NMR suffers from low SNR, maximum efficiency in power transfer between the coil and the LNA is of great interest.

According to circuit theory, maximum power transfer between two circuits is achieved if their impedances are complex conjugate. As a standard procedure, commercial LNAs have  $50\ \Omega$  resistive impedance at their input. Besides, the coaxial cable, which connects the coil and the LNA, has a characteristic impedance of  $50\ \Omega$  meaning that it has its best performance once it is terminated to this impedance at both ends. Therefore, the impedance of the coil should also be transferred to  $50\ \Omega$ . In its simplest form, it is realised with two capacitors known as tuning and matching capacitors, respectively. Usually, power dissipation in these capacitors is negligible since capacitors have high quality factors. Nonetheless, the two capacitor set-up can provide the tuning/matching at only one certain frequency.

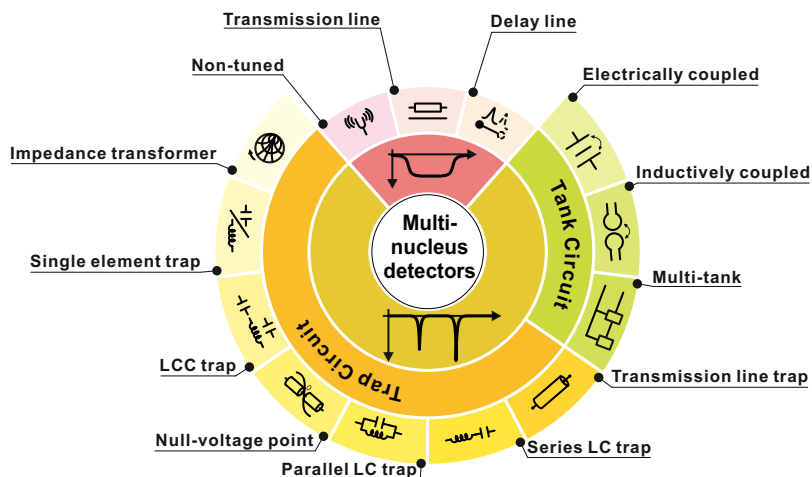
Consequently, using the tuning/matching circuit enhances the power transfer efficiency at one frequency with the cost of degrading power transfer at the other frequencies. One possibility for multinuclear detection is to employ multiple coils, each of which being tuned/matched at a certain frequency and all of them sharing the same sample volume. There are four issues associated with these designs: i) restricted access in the bore of the superconducting magnets does not allow several pieces of hardware to be implemented; ii) the additional hardware in the bore of the magnet distorts  $B_0$  homogeneity and spectral resolution; iii) cross-talk between the coils results in additional noise in the receive mode, as well as power leakage in the excitation mode, which is harmful to the circuits in the secondary channel and/or distorts the concurrent measurements; iv) different coils have different regions of interest meaning that the actual sample under study is different at different frequencies.

The other possibility is to use a single coil but to employ a different type of tuning/matching network to achieve multiresonant performance. The network can either provide multiple output ports and act as a demultiplexer, so that each port corresponds to a certain frequency, or have a single output port and provide the tuning/matching for all frequencies at that port. In the former case, the cross-talk between the ports, as well as the power dissipation within the network, should be considered. The latter option requires additional filters at the input of the LNA to block the unexpected frequencies in concurrent measurements. In both circumstances, the network should be as close as possible to the coil, in order to enhance power transfer efficiency. Therefore, the elements of the network distort  $B_0$  field. Moreover, the multi-coil and multiresonant configurations can be combined to provide multinuclear detection. The resonance-based circuits are especially useful when two or three nuclei are to be detected. For higher numbers of nuclei, the circuit becomes too complex and the efficiency of the circuit drops considerably.

In addition to these configurations, some designs rely on variable capacitors or switches to either sweep within a range of frequencies or to switch between multiple frequencies. These designs are not capable of simultaneous excitation and detection at different frequencies.

In another category, the coil has a wide working bandwidth so that more than one nucleus can be detected. These wideband detectors require no means of tuning and matching. As expected, they exhibit lower SNR in comparison to their single resonance counterparts. Considering their wide bandwidth and ability to detect several nuclei, broadband coils are a good choice for the cases when more than five nuclei are to be detected. Figure 2.6 presents all different configurations and methods which can potentially provide multinuclear detection with a single coil.

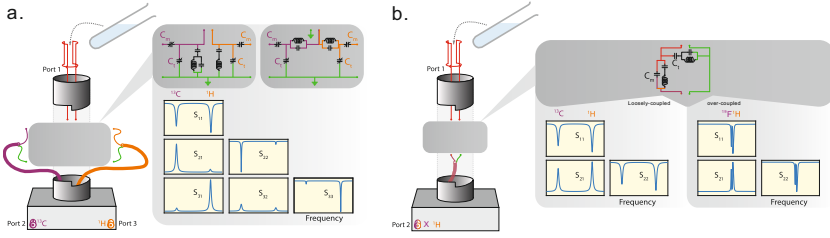
This section provides a thorough study of the multiresonant circuits and also broadband coils for NMR applications by analysing their building blocks and possible topologies. For this purpose, Subsection 2.5.1 considers the multiresonant circuits and Subsection 2.5.2 focuses on the broadband schemes.



**Figure 2.6:** Different topologies enabling multinuclear NMR detection employing just one NMR coil. While the multiresonant circuits enable NMR at multiple discrete frequencies, broadband topologies offer a wide bandwidth in which the detection can occur. Multiresonant circuits are divided into two subcategories: tank circuits and trap circuits. The broadband designs can be categorised as delay line, transmission line, and non-tuned topologies. Tank circuits rely on either electrically coupled, inductively coupled, or multi-tank topologies. Trap circuits can be realised by either transmission line traps, series LC traps, parallel LC traps, null-voltage points, LCC traps, single element traps, or impedance transformer circuits. The figure is reproduced from [HD1].

### 2.5.1 Multiresonant NMR detectors

Two different topologies, which enable multiresonant detection with a single coil, are presented in Figure 2.7. The main difference between these two is the total number of access ports, being available for each configuration. While the topologies relying on the trap circuits provide multiple access ports, the topologies employing tank circuits deliver all the frequencies at one single port. Nevertheless, the trap and tank building blocks are not limited to the ones depicted in Figure 2.7 but there is a wide range of selections as shown in Figure 2.6. In order to gain a better understanding of these building blocks, the blocks are introduced and analysed in Subsection 2.5.1. The circuit topologies which employ these building blocks are discussed in Subsection 2.5.1.



**Figure 2.7:** Two different topologies to achieve a multiresonant network. a. A trap network has multiple ports. Where the first port is connected to the coil, the other ports are the output ports to be connected to their corresponding channels. Accordingly,  $S_{11}(f_i) = -\infty$  and  $S_{ii}(f_i) = -\infty$  and  $S_{ij}(f_i) = 0 \forall i$  to satisfy the maximum power being delivered to the coil whereas  $S_{ij}(f_i) = -\infty \forall i, j \neq 1$  and  $i \neq j$  to satisfy a good inter-channel isolation. In terms of the first port, it can be as a differential port or a common port with one line sharing a common potential with the other ports. b. A tank topology provides a two-port network in which the first port is connected to the coil and the second port is connected to the channels. In this case,  $S_{11}(f_i) = -\infty$ ,  $S_{22}(f_i) = -\infty$  and  $S_{12}(f_i) = 0 \forall i$ . The tank topologies can be either loosely coupled or over coupled. The figure is reproduced from [HD1].

## Methods

- **Trap circuits:** In their ideal form, trap circuits act as frequency-dependent switches which allow a frequency (or a range of frequencies) to pass and block the rest. These switches are made of components such as inductors and capacitors. Because of the limited quality factor of these elements, the block and pass behaviour of the trap circuits are not ideal and there is some power leakage or attenuation, respectively. Different methods to realise a trap circuit are listed as follows.

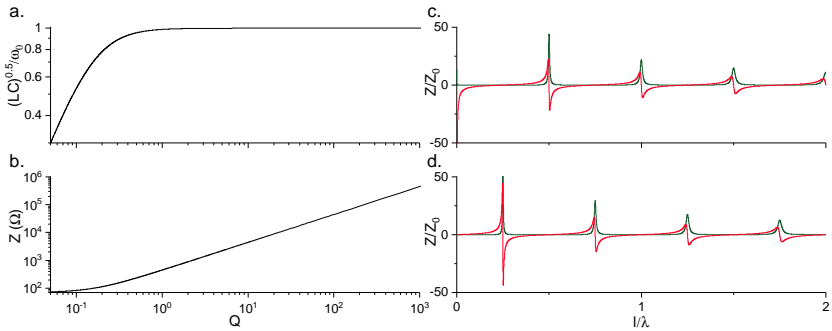
- (a) *Parallel LC trap:* ignoring the effect of the self-resonance frequencies of the inductor and capacitor, the impedance of a parallel *LC* trap is

$$Z = \frac{r}{(1 - LC\omega^2)^2 + r^2C^2\omega^2} + j\omega \frac{L(1 - LC\omega^2) - r^2C}{(1 - LC\omega^2)^2 + r^2C^2\omega^2} \quad (2.13)$$

where  $r$  is the series resistance of the inductor,  $L$  is the inductance of the inductor,  $C$  is the capacitance of the capacitor and  $\omega$  is the working frequency in  $\text{rads}^{-1}$ . At its resonance frequency (where the



imaginary part is zero), the trap acts as an open switch with high resistance. The resonance frequency and the impedance of the switch depend on the quality factor of the coil ( $Q = L\omega_{res}/r$ ). At frequencies lower than the resonance frequency, the inductive part is dominant and the circuit acts as an inductor with a certain resistance, whereas at the frequencies higher than the resonance frequency, the circuit acts as a lossy capacitor. Therefore, this circuit is usually used as a low-pass trap in the series mode and a high-pass trap in the shunt mode. Figure 2.8.a. and b. show the trap frequency and the trap impedance as the functions of the inductor quality factor.



**Figure 2.8:** a. The trap frequency as a function of quality factor for a parallel  $LC$  trap. b. The trap impedance as a function of quality factor for a parallel  $LC$  trap. c. The impedance of an open-ended transmission line as a function of its length with respect to the frequency. d. The impedance of a shorted transmission line as a function of its length with respect to the frequency.

(b) *Series LC trap*: the impedance of a series  $LC$  circuit is

$$Z = r + j \frac{LC\omega^2 - 1}{C\omega} \quad (2.14)$$

and at its resonance frequency, the trap acts as a signal path with relatively small resistance. The trap acts as a capacitor at frequencies lower than its trap frequency and as an inductor at frequencies higher

than the trap frequency. Accordingly, the series  $LC$  is a high-pass trap in the series mode and a low-pass trap in the shunt mode.

- (c) *LCC trap*: the impedance of a circuit consisting of either a parallel  $LC$  in series with a capacitor or a series  $LC$  in parallel with a capacitor is purely resistive at two different frequencies. At the lower trap frequency, it has a low resistance and can be exploited as a short circuit whereas at the higher trap frequency it has a high resistance and can be exploited as an open switch. Therefore, these circuits can be used as both low-pass or high-pass traps in either series or shunt modes, respectively.
- (d) *Open-ended transmission line*: the impedance of a transmission line being measured at one of its ports when the other port is open, is

$$Z = \frac{Z_0}{\tanh(\Gamma l)} \quad (2.15)$$

where  $Z_0$  is the characteristic impedance of the transmission line and  $l$  is the length of the transmission line.  $\Gamma$  is a complex value known as the propagation constant. Its real part ( $\alpha$ ) is known as the attenuation constant and determines the power loss during wave propagation and is negligible when  $l$  is shorter than the wavelength. The imaginary part ( $\beta = 2\pi/\lambda$ ) determine the phase of the wave while propagating through the transmission line. An open-ended transmission line is always a shunt element which traps wavelengths  $\lambda = 4l/n$  with  $n \in \{1, 3, 5, \dots\}$ . Figure 2.8.c illustrates the impedance of an open-ended transmission line as a function of the signal frequency. To keep power dissipation in the cable small, as well as eliminate unwanted trap performances at other frequencies, the open-ended transmission line is usually used as a high-frequency trap and the length of the transmission line is selected to be  $\lambda/4$  where  $\lambda$  is the wavelength of the high-frequency signal.

- (e) *Shorted transmission line*: the impedance of the transmission line at its first port, when the second port is shorted, is

$$Z = Z_0 \times \tanh(\Gamma l) \quad (2.16)$$

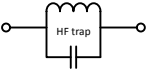


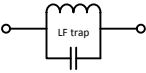

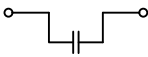

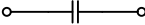
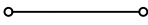
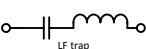
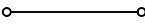

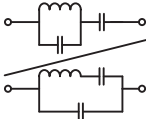


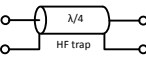
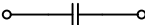
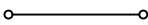
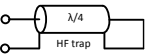


and in the shunt mode it traps signals with wavelength  $\lambda = 2l/n$  if  $n \in \{1, 2, 3, \dots\}$ . Figure 2.8.d shows the impedance of a shorted trap as a function of its length. Usually, the shorted transmission line is employed as a low-frequency trap and the length of the transmission line is calculated as  $l = \lambda/4$  where  $\lambda$  is the wavelength of the high-frequency signal.

Table 2.1 summarises the trap circuits at different frequencies. The skin effect shall be considered when selecting a trap. In the parallel *LC* high frequency (HF) and the *LCC* traps, the skin depth decreases the resistance of the traps at high frequencies whereas, in the parallel *LC* low-frequency (LF) traps, the skin depth does not have a significant effect. Similarly, in the series *LC* HF trap, the skin effect degrades the trap performance but, it enhances the performance at high frequencies in the series *LC* LF trap.

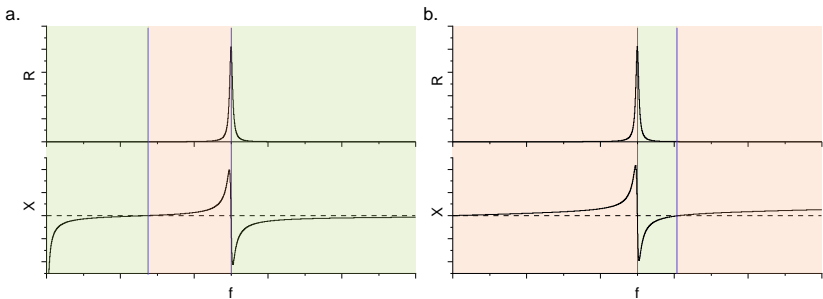
- **Tank circuits**: The tank circuits are similar to the trap circuits in terms of the circuit elements but the difference is at the working frequencies. As discussed, an *LC* circuit acts as either an inductive or a capacitive element at the frequencies except for its trap frequency. This inductive or capacitive element can be exploited as a variable element to tune and match the coil at different frequencies. The connection between the tank circuit and the coil is established using two different methods:

- (a) *Electrically coupled tank circuits*: in this case, the *LC* circuit is added to the tuning/matching capacitor to manipulate its impedance and allow for the multiple resonance performance. The circuit consisting of the tuning/matching capacitor and the tank circuit looks like an *LCC* but as mentioned, it is exploited at frequencies other than the

**Table 2.1:** Different types of trap circuits with their simplified equivalent electrical models at different frequencies with respect to their trap frequency. The table is reproduced from [HD1].

Circuit block	Low-frequency equivalent circuit	High-frequency equivalent circuit
		
		
		
		
		
		
		

trap frequencies. Two different possible configurations are: a series *LC* in parallel to a capacitor or a parallel *LC* in series to a capacitor. Regardless of the circuit configuration, the impedance of the circuit can be divided into respectively three different zones: a low-frequency capacitor, a mid-frequency inductor, and a high-frequency capacitor, as presented in Figure 2.9. The interesting regions, in this case, are the first and the last zones as the circuit exhibits capacitive performances.



**Figure 2.9:** a. An  $LC$  tank circuit, being electrically coupled to a tuning/matching capacitor, divides frequency axis to three zones. The circuit is exploited as a tank circuit at the first and the last zones. b. An  $LC$  tank circuit, being inductively coupled to the coil, divides the frequency axis to three zones. The circuit is exploited as a tank circuit at the first and the last zones.

- (b) *Inductively coupled tank circuits:* a parallel  $LC$  circuit can be coupled to the NMR coil through inductive coupling. Therefore, the total impedance seen from the coil port is accordingly divided into three distinct regions: a low-frequency inductor, a mid-frequency capacitor, a high-frequency inductor. The interesting regions are the first and the last regions as the circuit has an inductive behaviour.

### Challenges associated with tank/trap circuits

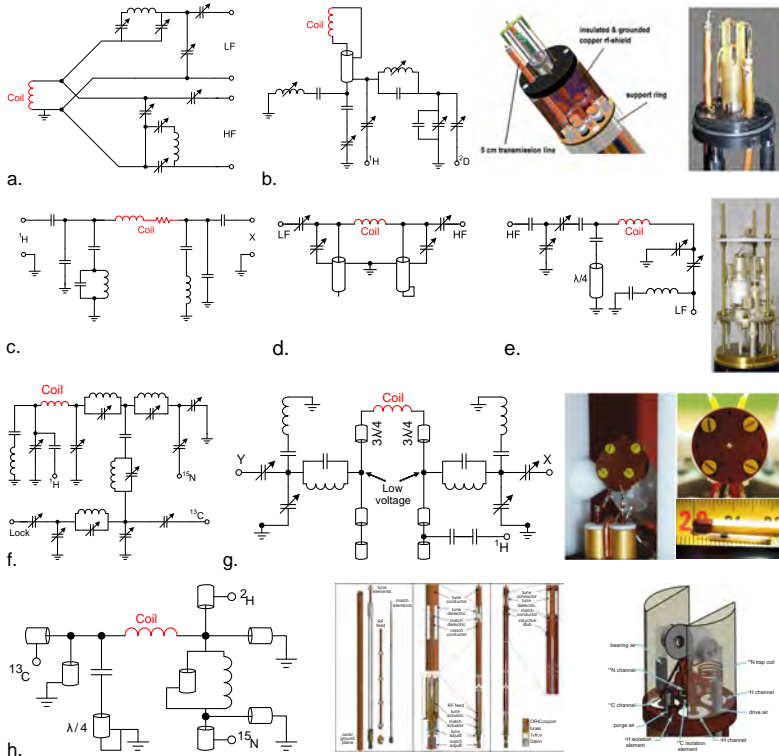
Tank and trap circuits should be placed in the close vicinity of the coil in order to eliminate long tracks and enhance the overall performance of the system. However, the coupling between the inductors and the coil is an experimental challenge to be considered when designing these circuits. The limited space inside the magnet bore, as well as  $B_0$  distortions, exacerbate the issue. Capacitors are the other elements in the trap/tank circuits which pose their own issues. On one hand, the capacitors should fulfil the magnetic compatibility requirements, on the other hand, the breakdown voltage of the capacitors should comply with the applied power. Usually, a higher applied power mandates more bulky capacitors, which make the whole tank/trap circuit larger and restrict the

total number of elements. The other consideration is the presence of several metallic elements inside the bore of the magnet which affects the RF magnetic field and the impedance of the coil and inductors. Therefore, in the design process of the trap/tank elements, the practical tolerances should be taken into the account.

## Topologies

- **Trap circuits:** In the circuits which require simultaneous excitation and detection at different frequencies, different channels should be isolated in order to maintain power transfer efficiency at the excitation channel and protect the circuit elements in the other channels from high amplitude excitation pulses. In the receive mode, the isolation assures the collected signal being delivered to the corresponding channel and eliminates the noise of the other channels to degrade SNR. Therefore, the trap circuits can be employed to provide isolation. Depending on the configuration of the traps with respect to the coil, the trap topologies can be divided into two main subcategories: the common mode and the differential mode. Assuming the coil as the core for the circuit, the differential mode is the case where two different channels are connected to two ends of the coil, whereas in the common mode both channels are connected to a common end of the coil. A few examples of these circuits are given in Figure 2.10.
  - (a) *Common mode traps:* In the case where the trap circuits are not next to the coil, the distance between the trap and the coil is bridged with a coaxial transmission line [58–60]. As result, the current of the coil is provided through the cable and the power dissipation in the cable plays an important role. Moreover, since the cable is not terminated to its characteristic impedance at the coil side, the impedance, seen at the other side, depends on the frequency and the cable length. This feature, known as impedance transfer, can be mindfully designed to improve the inter-channel isolation. It should be noticed that the trap

circuits shall be designed for the transferred impedances and not the coil impedance.



**Figure 2.10:** Different circuits employing trap topologies: a. Leach [61] designed a double resonant coil based on the *LCC* common mode traps; b. Kc [60] implemented a common mode trap circuit after transferring the impedance of the coil. c. A double-resonant differential mode trap circuit, developed by Spengler [62]. d. Doty [63] used the transmission line traps to provide the return path for the signals in a differential mode trap topology. e. Grant [64] implemented a differential mode trap with two traps at the low-frequency side. f. Li [65] used a differential mode circuit to differentiate between the high-frequency signal and the low-frequency channels. Three low-frequency signals are applied using the common mode traps. g. Brauckmann [66] inserted two low-frequency channels at the null-voltage points of the high-frequency channel in differential mode. h. Collier [67] employed a solenoid coil connected to a common/differential mode circuit in order to acquire three resonance frequencies. The figure is reproduced from [HD1].

The non-linear impedance transfer concept is meant to increase the contrast between the impedance of the coil at two different frequencies so that the isolation at these frequencies is easier. In its extreme case, the branch for each frequency is connected to the nodes at a certain length of the cable where the other signal has minimum amplitude [11, 68, 69]. These points, being called the null voltage point or the virtual ground, are helpful to enhance the isolation with no counter effects on the other channels. The impedance transfer concept has been also explored by adding a parallel capacitor to the coil to pre-tune the coil [45, 70–78] or by employing a combination of both capacitors and transmission lines [79–82, 82]. The impedance transfer is especially advantageous for micro-coils where their impedances are low and comparable to the impedance of the traps in their short circuit mode. Additionally, the signal is immune to the power loss in the connecting tracks when the coil impedance is transferred to a relatively higher value.

Nelson [83] reported the first common mode trap circuit based on parallel  $LC$  HF and series  $LC$  HF traps respectively in low-frequency and high-frequency signal paths. A similar circuit was reported by Stoll [84] where the series  $LC$  HF trap was replaced by a single capacitor to enhance the low-frequency isolation and simultaneously reduce the resistance at high frequencies with the cost of a small residual capacitance. Other authors [41, 45, 58, 60, 70, 85] have also used the single capacitor approach instead of the series  $LC$  HF traps, especially because this capacitor can be exploited as the tuning/matching capacitor of the high frequency channel. Besides, the  $LCC$  trap circuits have been employed by Kan [86] and later by Leach [61].

- (b) *Differential mode traps*: For the cases where balancing of the coil is essential, the differential mode is a better choice. It can be achieved by using a shunt trap circuit for the opposite port.



The differential mode circuits were introduced by Cross [87] where he used shunt segments of transmission lines to provide return paths, as well as to tune the coil, at different frequencies. Doty enhanced the design by replacing the tuning transmission lines with capacitors and the shunt open-ended transmission line with a series  $LC$  HF trap or a single capacitor [63, 88]. The single capacitor approach was picked up by other authors [64, 65, 67, 89–95] thanks to its superior noise performance and better power transfer efficiency at high frequencies. Since the capacitor, in this case, is a balancing capacitor and carries half of the voltage across the coil, it does not function as isolation for the low-frequency channel. In some cases, a secondary trap was employed to reduce power leakage and reinforce isolation [64–68, 77, 80, 86, 88, 91, 93–103].

Tang [93] and Zhang [89] proposed single inductors instead of the parallel  $LC$  HF trap which has poor isolation because of the amplified impedance at frequencies lower than the resonance frequencies. Zens [90], Stringer [103], and later Grant [64, 97] replaced the inductors with segments of transmission lines in series with capacitors in order to obtain low-frequency traps. The  $LCC$  traps were employed by Spengler [62] to improve circuit performance for micro-coils whereas Park [96] employed the  $LCC$  traps together with the tuned coil. Some reports also employed the impedance transformation techniques, namely the pre-tuning capacitors [71, 80, 90, 96].

The differential mode and the common mode circuits are often combined in a circuit where higher numbers of resonances are required. Similar to the double resonant differential mode circuits, the high-frequency resonances and the low-frequency resonances are fed from the different sides of the coil [65, 67, 77, 86, 99, 103]. Moreover, the common mode trap circuits are employed to maintain isolation between the frequencies within each range. With the help of this hybrid design, the total number

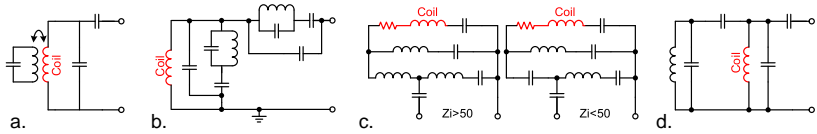
of isolation circuits can be reduced and accordingly the power transfer efficiency is enhanced.

The null-voltage point was exploited together with the differential mode circuits to achieve a higher number of resonance frequencies [68]. Lim [80] reported a triple-resonance coil in which the coil was first tuned to a frequency between the two highest frequencies. A differential mode configuration was employed with the aid of transmission lines to connect these high-frequency ports. A low-frequency channel, as the third frequency, was connected through the parallel  $LC$  traps to a null-voltage point in a common mode configuration. Three circuits in which the combination of the differential- and the common mode trap circuits are employed are depicted in Figure 2.10.

- **Tank circuits:** Since the tank circuits provide the tuning and matching at different frequencies for a coil through a single port, the inter-channel isolation is impossible. Therefore, either external elements, e.g., filters, are required for experiments with simultaneous activation of the channels or this topology should be employed in the sequential experiments. Having just one access port makes these circuits especially advantageous when there is a restricted access to the coil, e.g. in narrow bore magnets. In the early use of the tank circuits, the universal  $50\ \Omega$  impedance matching was not the case and efforts were focused on realising the resonant circuits for multiple frequencies [104–108]. Figure 2.11 illustrates a few examples of tank circuits.

Depending on the proximity of the resonance frequencies, tank circuits can be divided into two subcategories as:

- (a) *Loosely-coupled tank circuits:* If the desired resonance frequencies are relatively far (more than 10 %) from each other, the frequency gap between the resonances provides a good margin and the tank circuit behaves either as a capacitor or as an inductor at the desired



**Figure 2.11:** a. Kan [109] suggested an inductively coupled tank for a double resonance circuit. b. Tadanki [110] used two loosely-coupled tank circuits electrically coupled to the tuning/matching capacitors. c. Otake [111] electrically coupled two loosely tank circuits to the coil to achieve two close resonance frequencies. d. Haase [112] achieved two close resonance frequencies employing an over-coupled tank. The figure is reproduced from [HD1].

frequencies. Chang [113] reported balanced matching of a tank topology employing two capacitors at each side of the tuned coil. Blum [114] employed a circuit consisting of two parallel  $LC$  tank circuits, a capacitor, and the coil in series. The transceiver coil is coupled to the inductors of these tank circuits. By adjusting the distances between the inductors and the transceiver coils, Blum could maintain a good matching at different frequencies.

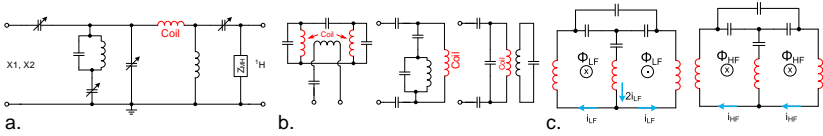
Leach [61] and Tadanki [110] proposed the most comprehensive double resonant circuits using the tank method, as these configurations provide both tuning and matching at two different frequencies. These circuits provided enough degrees of freedom by employing multiple capacitors and tank circuits. Subramanian [115, 116] employed multiple parallel tanks in series (plain) to achieve a higher number of resonance frequencies whereas Eleff [117] suggested a nested configuration. The power transfer efficiency in a plain circuit at each resonance frequency is independent of the relative position of its corresponding tank elements. In contrast, the power transfer efficiency decreases with the order of its corresponding tank circuit in the nested configuration .

In a different approach, in order to provide tuning and matching for two close frequencies (6% apart), Otake [111] suggested a tank circuit consisting of two parallel series  $LC$  circuits with different

resonance frequencies (20 % separation) in series with a capacitor. This tank was connected in parallel with a resonating coil. Schnall [105, 107] reported an inductively coupled tank circuit and a coil. This circuit was later upgraded employing an extra capacitive link between the main coil and the tank circuit [109, 118]. The extra capacitor enhances the stability of the network without introducing additional signal loss. Rajan [119] exploited a segment of the coil as the inductor of the  $LC$  tank in a similar configuration. The single-inductor double resonant circuit reduces the noise contribution and offers a more compact design. Gonnella [120] reported a similar circuit but for the surface coils. The main drawback of this design is poor field homogeneity and low efficiency at the higher resonance frequency as the currents in two segments are anti-parallel. Inukai [121] employed an inductively coupled tank circuit in which two coils are both electrically and inductively coupled and additionally are coupled to a transmission coil. With the aid of capacitors, multi resonant performance is brought to the coils.

- (b) *Over-coupled tanks*: In order to provide a double resonant circuit where the resonance frequencies are less than 10 % apart, two resonating circuits with the same resonant frequencies can be coupled together. In this case, the single resonant frequency splits into two distinct frequencies.

Collins [122] implemented an electrically over-coupled circuit for a coil, being inductively coupled to a transceiver coil. A similar design was employed later with an electrical coupling between the tank and the transmission line, utilising the matching capacitors [112, 123, 124]. Hu [125] discussed an electrically over-coupled circuit for a saddle coil where the coupling capacitor was split into four capacitors distributed along the coil conductors. With this design, the current distribution throughout the coil was enhanced.



**Figure 2.12:** a. Zhang [89] developed a triple resonant circuit by inserting a tank circuit into the low-frequency side of a differential mode trap topology. b. Fitzsimmons [127] compared three different double-resonance approaches (electrically coupled, inductively coupled, and LGR). c. Cao [128] proposed a CMDM circuit to allow the LF signal through a series  $LC$  trap circuit in the middle branch and block the high-frequency current. The figure is reproduced from [HD1].

- Combination of both tank and trap:** Kendrick [74] combined an over-coupled tank circuit with a common mode trap to achieve a triple-resonant circuit with two high frequency channels. As depicted in Figure 2.12.a, Zhang [89] also combined a differential mode trap with an electrically loosely-coupled tank, in order to have a triple resonant circuit with two low-frequency channels. Paulson [126] employed an  $LC$  tank as a balancing capacitor at the high-frequency side and a balancing inductor at the low-frequency side of a differential mode double resonant circuit. The traps for the circuit were realised using two quarter-wave transmission lines.
- Other topologies:** A set of double-resonant receiver coils were proposed by Grist [129] where two coaxial, inductively-coupled loop-gap resonators (LGR) were tuned to the lower frequency. Tuning to the higher frequency was achieved by connecting the coils in series together with an additional capacitor. The coil assembly acts like a surface coil and the sample sits on top of the coil. The currents in the two coils are in parallel at the lower frequency while at the higher frequency the currents are anti-parallel. As the result, the system has a better power transfer efficiency at low frequencies compared to the higher frequencies.

Fitzsimmons [127] improved the system introduced by Grist [129] by exploiting the LGR coil as both excitation and receive coil. Fitzsimmons showed that the LGR coil has a better performance with respect to the

conventional trap/tank circuits (see Figure 2.12.b). In another report, Van Hecke [130] studied an LGR coil, tuned at two distinct frequencies, utilising a tank circuit and at different matching configurations. Volotovskyy [131] employed two flat ring coils with different diameters rather than the LGR coils. The loops were tuned to both frequencies using the tank circuits. A third coil, which was also in series with a parallel  $LC$  frequency tank, was coupled to the two coils.

Pang [132] suggested a common-mode differential-mode (CMDM) coil using a single micro-strip coil on a PCB. The smart design of the coil, resulted in two orthogonal RF fields hence 30 dB isolation. Cao [128] enhanced the coil performance by adding a series  $LC$  LF trap at the centre branch, carrying the low-frequency current. Additionally, the RF field homogeneity was enhanced by bending the coil around a cylinder. The working principle of this coil is presented in Figure 2.12.c.

### 2.5.2 Broadband NMR detectors

Based on their configurations, the broadband detectors are divided into three categories. These categories are introduced and discussed in more detail in the following subsections.

#### Delay line coils

This type of coils forms a two-port network of discrete lumped capacitors and inductors connected as either  $\pi$ - or  $T$  networks. The concept of delay line coils was introduced by Lowe [133]. A low-pass  $\pi$ -network was reported with the inductors ( $L$ ) being the segments of a solenoidal coil and extra capacitors ( $C$ ) to ground these segments. A model was also proposed for the case where both ports of the coil were terminated to its characteristic impedance of  $Z_0 = \sqrt{0.5L/C}$  without considering the mutual inductance between the segments. Accordingly, the network cut-off frequency was predicted as  $\omega_c = \sqrt{2/LC}$  beyond which the performance of the network degrades. It was concluded that for frequencies

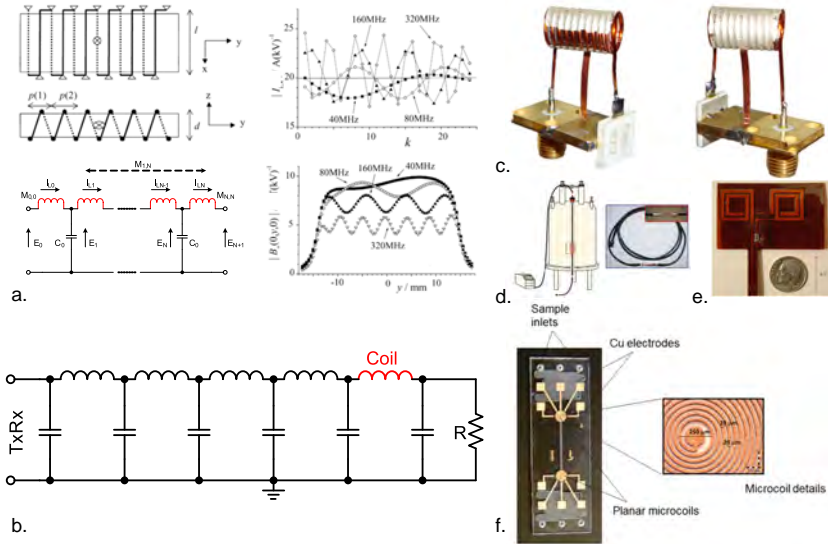
smaller than the cut-off frequency, the time delay per segment ( $T = \sqrt{2LC}$ ) is frequency-independent, and the signal collected by the inductive elements is divided between two ports equally. In a different report, Lowe [134] suggested a flat solenoid delay line probe with a rectangular cross-section (its length and height being much larger than its width) to improve the field homogeneity. Another improvement was achieved by considering the mutual inductances of the neighbourhood elements in the model. It was also proved that the cut-off frequency does not exist if the coupling between the segments is strong ( $0.5 \leq k \leq 1$  where  $k$  is the coupling). For a weak coupling ( $0 \leq k < 0.5$ ), the cut-off frequency can be calculated as  $\omega_c = \sqrt{2/LC} \times 1/\sqrt{1-2k}$ . The time delay per segment and the characteristic impedance of the coil are  $T = \sqrt{2LC} \times \sqrt{1+2k}$  and  $Z_0 = \sqrt{L/2C} \times \sqrt{1+2k}$ , respectively.

As depicted in Figure 2.3.a, Kubo [135] analysed an arbitrary delay line coil of  $N$  cascaded  $T$ -networks. The inductance of each segment was assumed equal to the total inductance of the coil ( $L$ ) divided by the total number of segments. The effective impedance of the coil was defined as  $Z_{\text{eff}} = \sqrt{L/NC}$  and the cut-off frequency was defined as  $\omega_c = \sqrt{4N/LC}$ . The time delay was calculated as  $T_d = d\beta/d\omega$  where  $\beta = 2N\omega/\omega_c$  is the propagation constant.

Scharfetter [136] investigated a ladder network, consisting of  $N$   $\pi$ -segments, as an alternative for the delay line coils. As shown in Figure 2.13.b, one of the inductors in the network is exploited as the NMR coil. The values of the inductors and capacitors in the  $\pi$ -sections were selected so that the network approximates an exponential transmission line with different characteristic impedances of individual segments and identical centre frequencies. As the result, the network interfaces two different impedances with a good matching over a wide range of frequencies.

### Transmission line coils

The transmission line coil relies on the same concept as the delay line coils but using distributed impedance. The transmission line coil is realised using



**Figure 2.13:** a. Kubo [135] studied the delay line coils using their equivalent  $T$ -model and predicted the current distribution through the coil segments and the magnetic field generated on the axis of a flat coil. b. Scharfetter [136] proposed a ladder exponential delay line. c. Scott [137] developed a transmission line solenoid coil terminated to the  $50\ \Omega$  load. d. Tang [138] exploited a coaxial cable as a transmission line coil by replacing the dielectric of a segment of the cable with the sample. e. Murphree [139, 140] used a flexible PCB to make a transmission line saddle coil. f. Fratila [141, 142] achieved a wideband performance using the spiral micro-coil. The figure is reproduced from [HD1].

a conductive strip separated from a grounded plane by a dielectric layer. The distributed capacitance between the strip and the grounded plane provides the capacitors whereas the strip itself is the inductance. This topology offers a flat frequency response over a wide range of frequencies as long as the transmission line is terminated to its characteristic impedance at both terminals. Few different designs are presented in Figure 2.13.

Stokes [143] reported the first transmission line coil consisting of a 13-turn solenoidal coil encapsulated by a dielectric layer and wrapped with a grounded brass foil. Webber [144] and later Scott [137] employed similar coils with the



grounded conductor partially covering the outer surface to have  $50\ \Omega$  characteristic impedance.

Tang [138] selected a different approach where a coaxial cable was employed as the transmission line coil. In this case, they simply replaced a section of the cable dielectric with the sample. Tang [138] showed that the performance of the cable terminated to its characteristic impedance is independent of the cable length. Murphree [139, 140] also used a flexible circuit board to fabricate the first transmission line saddle coil.

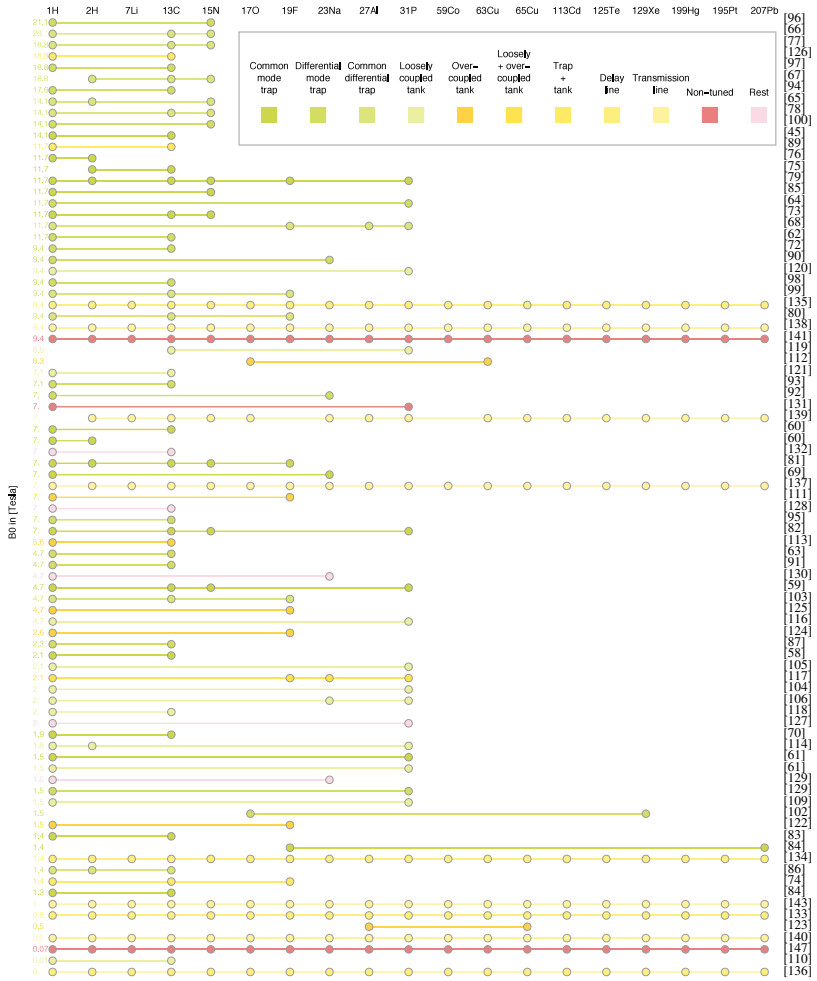
Regardless of their design, both delay line and transmission line coils have three main drawbacks: i) the relatively low SNR of the coil because of the considerable noise generated by the loads at the terminals of the transmission line; ii) the collected power being divided between two ports; iii) low  $B_1$  homogeneity because of the phase variation of the signal as it flows through the coil.

### **Non-tuned coils**

A non-tuned coil is mainly an inductor connected to the transceiver circuit with its matching traded for a larger bandwidth. To this end, Abraham [145] intentionally reduced the quality factor of the tuning capacitor by adding a resistor in parallel to that. This technique allowed him to achieve a bandwidth wide enough to detect two distinct Larmor frequencies 3.6 % apart.

Mandal [146–148] suggested a system working at very low frequencies (0.1–3.0 MHz). In this case, the tuning and matching of the coil were ignored, the impedance of the coil was multiplied with the aid of a transformer, and the transmitter and receiver were adjusted accordingly to avoid power reflection.

Fratila [141, 142] reported a spiral coil being optimised for the transceiver system which can be employed to detect all NMR active nuclei from 61 MHz to 400 MHz with a superb SNR. The spiral coil, discussed by Fratila, is a micro-coil with an active sample volume of 25 nl. Chapter 4 focuses on the non-tuned micro-coils and discusses this finding in more details.



**Figure 2.14:** A comparison of the multinuclear NMR probes. Each line in the plot corresponds to a specific probe, with the field strength  $B_0$  in T to the left, and the literature citation to the right. The dots correspond to the nuclei, hence, the frequency. The colour coding indicates the specific circuit topology, as shown in the legend. The figure is reproduced from [HD1].

Different designs enabling multi-nuclear detection are listed in Figure 2.14. This figure categorises these designs based on their working magnetic field and the nuclei, which the designs are capable to detect. The colour code corresponds to the topologies/methods being employed.



## 3 Microfluidic platforms for *in situ* electrochemistry

### 3.1 Overview

This chapter is aiming for a lab-on-a-chip system, consisting of an NMR coil and an electrochemistry insert, in order to enable monitoring electrochemical process in micro-domain. For this purpose, a modular NMR detector, which has been previously presented by Spengler *et al.* [62, 149], is further developed to meet the requirements. The detector consists of a Helmholtz (HH) coil and an interchangeable insert. This insert loads the sample into the detection zone of the coil with the help of a simple microfluidic channel. The electrochemistry electrodes (at least two in this case) are integrated into the insert so that an electric potential can be applied to the sample inside the detection zone.

The chapter starts with a brief review of the chemical reaction monitoring using NMR, more specifically, the electrochemical reaction monitoring using NMR and the chemical reaction monitoring using micro-NMR techniques followed by a study of the challenges arising at the intersection of electrochemical reactions and micro-NMR. In order to evaluate different electrode configurations for the micro-electrochemistry-NMR applications, the figures of merit (FOM) are discussed in Section 3.3 followed by introducing different electrode configurations. These configurations are simulated and the simulation results are processed to achieve the aforementioned figures of merit. Some of those configurations were selected for fabrication and experimental characterisation as discussed in Section 3.4 and Section 3.5, respectively. The experimental characterisation is followed by verification of the best configurations in a simple EC-NMR experi-

ment. The application is introduced and discussed in details in Section 3.6. The current chapter will be closed by a brief discussion and conclusion.

The achievements of this work have been presented in two journal papers: the simulation, fabrication, and experimental evaluation of the different inserts have been published in **Lab-on-a-chip (RSC)** journal [HD2]; employing the inserts for monitoring the activity of localised enzymes is the subject of an article, submitted in **Angewandte Chemie (Wiley)** journal [HD5].

## 3.2 Introduction

NMR is one of the most powerful tools amongst different spectroscopic methods in monitoring chemical reactions as well as determining reaction kinetics. The quantitative analysis of the reaction, achieved by NMR, enables a precise evaluation of the on-going process. Besides, as NMR observation does not interrupt the reaction or destroy any substances, this technique is gaining lots of interests despite its inherent low sensitivity. Furthermore, NMR does not need any calibration prior to the experiment and has a high chemical resolution. These features make NMR a preferable technique comparing to the other spectroscopy counterparts [150–152]. However, the main requirement, to be fulfilled, is either to keep the reaction inside the field-of-view (FOV) of the NMR detector or to introduce the reagents and products to the FOV. The FOV is usually located in the vicinity of a coil, as the  $B_1$  source, inside a strong (1–22 T), extremely homogeneous (sub-ppb uniformity), static magnetic field with restricted access. While low field online NMR reaction monitoring methods are popular because of the compactness and lower costs of the devices [152–155], numerous high field NMR spectroscopy techniques have been also developed for the chemical reaction monitoring due to their intrinsic higher resolution and sensitivity [156–159]. For the online reaction monitoring, the conventional NMR sample tube is replaced with a reactor and NMR captures the on-going reaction. The sample introduction to the reactor can be either in the stopped-flow mode [151, 152, 159] or in the flow mode [153–157].

Miniaturisation of the reaction chambers introduces new opportunities for chemical and process industries as it: i) allows advanced processing, as a result of the heat and mass transfer characteristics in micro-regime, ii) enables distributed production, iii) reduces the costs in chemical and pharmaceutical industries, iv) increases the safety of the experiment [160]. Together with micro-reactor developments, micro total analysis systems ( $\mu$ TAS) and Lab-on-a-Chip (LOC) concepts were developed to control and monitor the on-going processes.

Interestingly, miniaturisation is one of the possible solutions to tackle the low sensitivity of the NMR methods for mass-limited samples [10]. The enhanced sensitivity in micro-domain makes NMR techniques a perfect fit for  $\mu$ TAS applications. Different reports have discussed monitoring reactions in a LOC system comprising micro-reactors and micro-coils [18, 31, 44, 45, 160–165].

Apart from the specific challenges associated with the reaction monitoring using NMR, the microfluidics, and/or the micro-NMR techniques, once these fields are merged into an LOC system some new challenges arise which hinder the monitoring performance. The micro-reactors, being more complex than a conventional sample container, introduce magnetic susceptibility discontinuities at close vicinity of the FOV, perturb the nominal  $B_0$ , and reduce the spectral resolution and the signal-to-noise ratio (SNR). Literature contains many different reports about the susceptibility issues in the microfluidic domain and possible methods to compensate them either by material choice or engineering the environment of the sample chamber [18, 31, 39, 41, 44, 163, 164, 166, 167]. Section 3.2.2 discusses this issue in more details and reviews the possible solutions in the literature.

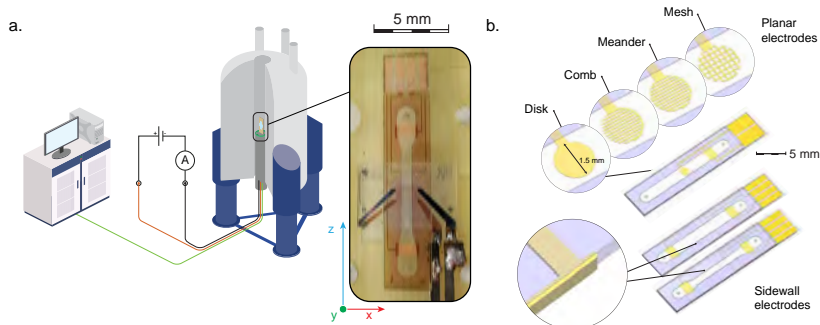
Electrochemical (EC) reactions are a subset of chemical reactions, which require electrical field or electrical conductors to enable the reaction. NMR is one of the best methods for structural elucidation and, therefore, a popular technique to observe the EC reactions, e.g, electrodeposition, electrooxidation, electrochemical process in the fuel cells, electrolysis, electrophoresis, dielectrophoresis [168–179].

Nonetheless, adapting the conductors inside the FOV is the challenge to be addressed in this case [175, 180, 181]. Unlike the conventional dielectric materials used for microfluidic channels, the metallic/conductive structures influence both  $B_0$  and  $B_1$  distribution.  $B_1$  field induces an eddy current in the metallic structures. The resistance of the eddy current path results in power loss in the system. It affects both excitation and detection performance by reducing the available power for the sample and introducing noise, respectively. The metallic structures can also shield the RF field and prevent the sample from being exposed by  $B_1$  field. These phenomena have been subject of different studies since the very beginning of the EC-NMR applications [170, 173, 175, 177, 182–187]. The solution to this incompatibility is either to keep the electrodes away from the FOV or to make them thin enough to be transparent to the RF field. Although these solutions might be applicable in some restricted applications, there are certain applications which cannot rely on these solutions, e.g., the energy storage devices requiring a certain amount of current flow.

Similar incompatibility concerns between the metallic electrodes and NMR have been intensively studied for the clinical MRI experiments [188, 189] where the power dissipation in the electrodes can cause damage to the adjacent tissues or the susceptibility mismatches can end up in signal loss in the voxels close to the interfaces.

Miniaturisation exacerbates the issue with the shielding since it is more severe at the close vicinity of the electrodes and the compactness of the system introduces more susceptibility issues. Digital microfluidics is another novel technique which relies on the metallic electrodes to manipulate the reactants and products [164, 168]. Integrating those techniques to NMR requires a similar approach. Section 3.2.3 studies the issues associate with the conductive electrodes being exposed to  $B_1$  field in the NMR.





**Figure 3.1:** a. Experimental setup for *in situ* electrochemistry experiment consisting of NMR setup and electrochemistry system. The zoom inset is the standard HH coil adapted from Spengler *et al.* [149] and the narrow sidewall insert. b. Different electrode topologies.

### 3.2.1 Experimental set-up

In this work, an EC cell containing metallic electrodes and compatible with the detector proposed by Spengler *et al.* [62, 149] was developed. Integration of these electrodes to the microfluidic channel was considered as the main challenge to overcome. The HH coil consists of two parallel loops each 1.2 mm in diameter with 600  $\mu\text{m}$  distance between them. The coil was tuned at 500 MHz and matched to 50  $\Omega$ . The detector chip was mounted on a Poly(methyl methacrylate) (PMMA) adaptor. The adaptor was plugged on top of the Micro5 probe (Bruker) and a pair of pins provided the electrical access to the probe. The coil and its accompanying parts are demonstrated in Figure 3.1. The standard sample insert was a rectangular channel 2 mm wide, 18 mm long, and 90  $\mu\text{m}$  high, patterned out of a photoresist and sandwiched between two glass slides as demonstrated in Figure 3.1. The access to the channel was provided through the inlet and outlet holes, being patterned on the top glass layer. Further details of the coil and the standard sample insert can be found elsewhere [62, 149].

### 3.2.2 Susceptibility challenges in micro-NMR

According to the Gauss' law for magnetism, the relative susceptibility mismatch, taking place at the material interfaces, disturbs  $B_0$  field locally. Since the Larmor frequency of the spins in NMR depends on the actual static magnetic field, which they experience, a minute perturbation in  $B_0$  translates in a corresponding offset in the Larmor frequency. Considering the sample as an ensemble of spins, the susceptibility perturbations broaden the spectrum. Consequently, in a sample representing multiple NMR peaks, short peaks might be dominated by the high peaks in their neighbourhood or some dense peaks might merge into one peak. Therefore, some part of the information might be lost. The total area under a certain peak depends on the RF field magnitude at the sample region and the total amount of sample. Therefore, line-broadening affects peak amplitude and SNR.

In micro-regime, the sample volume is shrunk and the detector is accordingly miniaturised. By making the sample and the detector more compact, sensitivity increases for the cost of more susceptibility issues and wider linewidth [11, 13, 18, 44, 190]. In order to reduce the susceptibility issues, two general guidelines are discussed in the literature: i) avoid susceptibility mismatches around the FOV, ii) compensate for the inevitable material interfaces.

To avoid any irregular material interface, the stripline detectors, lying along the microfluidic channel and  $B_0$ , were developed [18, 38, 39, 41, 43, 44, 46, 47, 191, 192]. Some authors also employed materials having a susceptibility similar to that of the sample [193]. In parallel, some research focused on introducing a third material, with a different susceptibility, to the system and adjusting the field distribution at the FOV by optimising the distribution of the "three-body system". Utz *et al.* structured some air pockets at the PMMA sample holder and around the sample volume to compensate for the distortions [165, 166]. Korvink *et al.* presented a more general approach by employing finite element methods and optimising the geometries for any arbitrary material [167].

In the current work, the insert geometry is adopted from the standard insert developed by Spengler *et al.* [62, 149] and it is modified to contain the additional metallic electrodes. On one hand, the metallic electrodes exhibit a considerable susceptibility mismatch to the aqueous sample. On other hand, the electrodes should be in direct contact with the sample and hence no intermediate compensation layer is allowed. The potential options, to be considered to mitigate the susceptibility issues, are the geometry of the electrodes and the electrode material.

Nevertheless, the material is dictated by the end application. In this work, gold was selected as the electrode material despite its relatively high susceptibility mismatch to water. The main advantages of gold are: i) compatibility with microfabrication techniques, ii) relatively high standard electrode potential (SEP=1.69 V) [194, 195], iii) low oxidation rate and long lifetime especially as a thin film and in contact with an aqueous sample, iv) compatibility with chitosan sample as the main application for this work.

Therefore, the focus of this work is to tailor the electrode geometry for the NMR applications. In order to gain a better understanding of the susceptibility perturbations, different potential electrode configurations have been introduced, simulated, and analysed.

### **3.2.3 RF field challenges in micro-NMR**

According to the Faraday's law, a time-varying magnetic flux induces an electromagnetic force (EMF) in a closed path, enclosing the surface through which the flux is penetrating. In case of a metallic surface or a closed path with a finite resistance, this EMF generates a current. As per Lenz's law, the induced current opposes the changes in the magnetic flux. Therefore, it generates a secondary magnetic field in the opposite direction of the original one. In other words, the actual magnetic field circumvents the metallic path. Furthermore, as a result of current flowing in the path and its finite resistance, power is partially dissipated in the metallic structures.

Assuming a uniform distribution of the sample all over the sample volume and a perfectly homogeneous  $B_0$ , the NMR sensitivity at each elementary sample voxel depends on the average RF field at the location of that voxel. As the magnetic field is disturbed and some part of that is dissipated, the overall sensitivity is reduced especially for the voxels near the shielded zone.

In order to minimise the induced current and the perturbed field as well as the dissipated power, either the area of the surface enclosed by the current path (the electrode footprint) should be reduced or the resistance of the current path should be increased. The resistance of the current path depends on the resistivity of the material, the path length, and path width. The material and hence its resistivity is imposed by the application as discussed in the previous section. Therefore, the geometry of the electrodes is again the only option for optimisation.

Chen *et al.* presented an analytical model to calculate the penetrated RF field inside an infinite long cylinder as a function of the metallic wall thickness [185]. According to their calculations, the wall thickness shall be less than 0.1 % of the skin depth ( $\delta$ ) in order to achieve a field strength higher than 80 % of the external field.

As mentioned in the previous sections, depending on the applications, having a thin electrode might not be possible. Additionally, manufacturing and control over such thin layers are cumbersome. Therefore, in the following sections, different geometries are proposed and analysed in order to fulfil all requirements imposed by susceptibility and RF challenges as well as application requirements.

## 3.3 Theory

### 3.3.1 Selection of the insert geometry

Different insert geometries have been considered, simulated, and compared based on the figures of merit discussed in Section 2.3. These geometries bring the sample to the detection zone and carry some electrodes which can be used as the electrochemistry sites. As a reference for the evaluations, an electrode-free

insert was considered as well. Potential configurations for the electrodes, which have been considered with respect to the  $B_0$  and  $B_1$  orientations, are:

- **Perpendicular to  $B_0$  and parallel to  $B_1$ :** This topology develops a good sensitivity as the RF field experiences the minimum perturbation. Total power dissipation in the electrodes is minimised by making the surface of the metallic layer, facing wave-front, as small as possible. However, the static magnetic field is perturbed substantially as the static field encounters a material interface at the edge of FOV.
- **Parallel to  $B_0$  and perpendicular to  $B_1$ :** This topology benefits from minor static field distortion, but the RF field distortion and power dissipation are the major concerns. In order to minimise those issues, the solution is to reduce the electrode size. On one hand, the electromotive force, being induced in the electrode, depends on the perimeter of the electrode facing the wavefront. On the other hand, the thickness and the surface area of the electrodes affect the resistance against the induced current.

The shielding effectiveness of an infinite planar metallic shield parallel to the coil surface can be found elsewhere [196]. Nonetheless, there is no closed-form for the field distribution. Additionally, in the case where the field is generated using two loops in the form of a Helmholtz coil and the electrode diameter is comparable to the coil diameter. These constraints add to the complexity of the problem. Instead of an analytical expression, we rely on the numerical simulations of the field in different situations. Different geometries to be considered for this case are depicted in Figure 3.1 and discussed in Table 3.1.

The disk electrode has the worst performance as it depletes the field at the centre part and concentrates it at the edges. In order to evaluate the effect of the electrode thickness precisely, three disk electrodes with different thicknesses ( $0.1 \times \delta$ ,  $0.01 \times \delta$ , and  $0.001 \times \delta$ ) are considered. The mesh

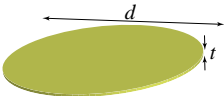

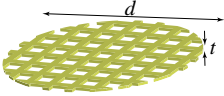
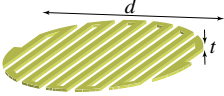
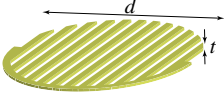
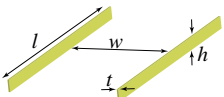
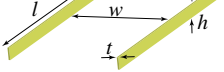
electrode enhances the field distribution in comparison to the disk as the metallic material is partially removed. Therefore, the current path is manipulated based on the mesh grids, and the resistance of the current path is increased. The comb electrode increases the current path resistance by increasing the length of the path for the same electrode surface area. Hence, the distortions are further reduced. The meander electrode is designed so that for the same electrode surface area, the length of the current path is maximised. Therefore, the distortions are minimum.

The surface area of the mesh, comb, and meander electrodes are selected to be 50 % of that of the disk electrode. It means that the available electrode size for electrochemistry is less. For each one of those geometries, the thickness of the electrode affects  $B_1$  distribution, the power dissipation in the electrode, and  $B_0$  distribution.

- **Parallel to both  $B_0$  and  $B_1$ :** For an infinitesimal electrode thickness, this topology is expected to act identical to the electrode-free case. However, because of the fabrication and mechanical stability requirements, the electrodes have a minimum thickness which leads to both  $B_0$  and  $B_1$  distortions. As a simple solution to avoid these distortions, the electrodes can be placed outside the FOV to eliminated their effect on both  $B_0$  and  $B_1$  distortions. This has been achieved by the wide-channel sidewall configurations. In contrast, in the narrow channel configurations, the distance between the electrodes is adjusted to take advantage of the eddy current induced in the electrodes and improve both  $B_1$  homogeneity and the mass-sensitivity.

In total eight different electrode geometries along with the electrode-free structure were considered to be studied using the simulation toolkit.

**Table 3.1:** Different electrode geometries have been employed as the active electrodes for *in situ* experiments.

Configurations	CAD design	Remarks
Electrode-free		na
Disk		$t = 340 \text{ nm}, d = 1.5 \text{ mm}$
Thin disk		$t = 34 \text{ nm}, d = 1.5 \text{ mm}$
Ultra-thin disk		$t = 3 \text{ nm}, d = 1.5 \text{ mm}$
Mesh		$t = 34 \text{ nm}, d = 1.5 \text{ mm},$ filling = 50 %, trackwidth = 50 $\mu\text{m}$
Meander		$t = 34 \text{ nm}, d = 1.5 \text{ mm},$ filling = 50 %, trackwidth = 50 $\mu\text{m}$
Comb		$t = 34 \text{ nm}, d = 1.5 \text{ mm},$ filling = 50 %, trackwidth = 50 $\mu\text{m}$
Wide-channel side-wall		$h = 90 \mu\text{m}, t = 30 \mu\text{m},$ $l = 8 \text{ mm}, w = 2 \text{ mm}$
Narrow-channel side-wall		$h = 90 \mu\text{m}, t = 30 \mu\text{m},$ $l = 8 \text{ mm}, w = 1.1 \text{ mm}$

### 3.3.2 Simulation settings

Electrical properties of different materials are summarised in Section A1. Mesh sizes were adjusted so that the sample volume and the electrodes have the finest mesh and the surrounding environment has the coarsest mesh.

## Physics

**RF simulations:** FEM simulations for RF studies were carried out using *Electromagnetic Waves, Frequency Domain* interface of *RF module* of the COMSOL MultiPhysics® 5.5 (COMSOL AB, Sweden).

Simulation of small structures is a common issue in all FEM techniques. The mesh size is determined by the size of the small features and the computation time increases accordingly. *Transition Boundary Condition* can be used in this interface to mimic the thin layers. This boundary condition assigns different tangential electric field and surface current densities on the different sides (1 or 2) of the thin layer [197]. For this purpose, the permittivity ( $\epsilon$ ), the permeability ( $\mu$ ), the electrical conductivity ( $\sigma$ ), and the thickness of the thin structure ( $d_s$ ) are used to calculate the currents density at each side ( $\{1, 2\}$ ) as:

$$\begin{aligned} J_{s,1} &= \frac{\cos(\Gamma d_s) E_{t,1} - E_{t,2}}{\cos(\Gamma d_s) - 1} \\ J_{s,2} &= \frac{\cos(\Gamma d_s) E_{t,2} - E_{t,1}}{\cos(\Gamma d_s) - 1} \end{aligned} \quad (3.1)$$

where  $\Gamma = \omega \sqrt{\mu(\epsilon - j\sigma/\omega)}$  is the propagation constant of the layer.

The maximum tolerable relative error for the RF simulations was set to 0.1 %. The study was performed at 500 MHz corresponding to the  $^1\text{H}$  Larmor frequency at 11.7434 T. Simulations were performed applying 1 A current to the coil terminals.

**Susceptibility simulations:** FEM simulations for susceptibility analysis were performed using *Magnetic Fields, No Currents* (MFNC) interface of *AC/DC module* of the COMSOL MultiPhysics® 5.5 (COMSOL AB, Sweden). Maximum tolerable relative error was set to 0.1 ppb. The permeability values of different materials were adopted from Schenck [189] and Wapler *et al.* [198].



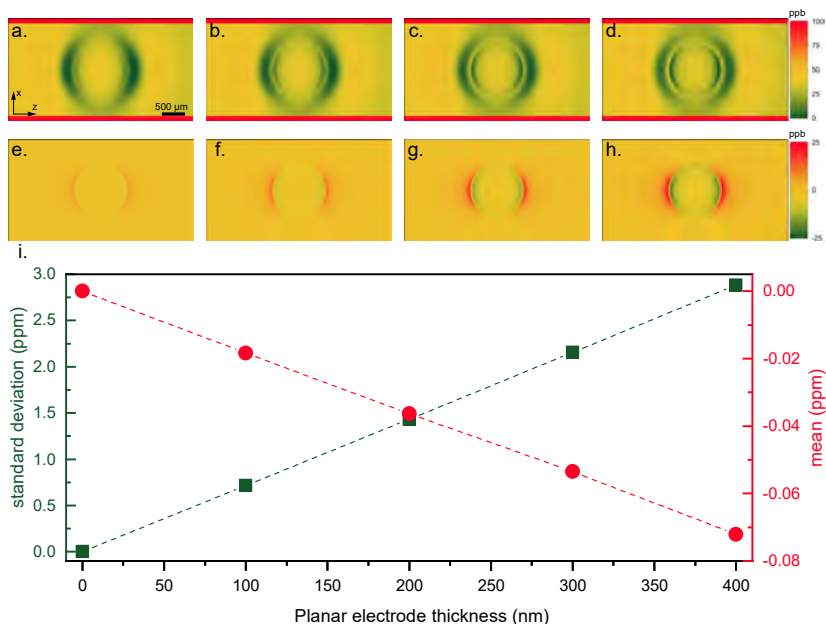
*Thin Low Permeability Gap (TLPG)* boundaries is a feature in MFNC which enables simulation of a thin object within a domain with higher permeability by approximating the flux relation on two sides of the layer as:

$$\vec{n} \cdot (\vec{B}_1 - \vec{B}_2) = \mu \left( \frac{V_m^1 - V_m^2}{d_s} \right) \quad (3.2)$$

where  $V_m^1$  and  $V_m^2$  are the magnetic potential on different sides of the TLPG,  $d_s$  is the thickness of TLPG, and  $\mu$  is the magnetic permeability of the TLPG layer [199]. This feature is mainly for the cases where a diamagnetic or a paramagnetic layer comes in contact with a ferromagnetic material, e.g. air gaps in the transformer core. However, for a relatively small susceptibility mismatch between the materials (the case of these simulations), this method is not reliable.

Considering the electrode thickness of 34 nm or 3 nm, the simulations would be extremely intensive and are not feasible because of the memory requirements. In order to evaluate the performance of the thin structures, the disk thickness was swept for the bulk electrode simulations and the results are presented in Figure 3.2. Other details of the geometry such as the coil and glass substrates have been also included in the simulations to have a better understanding of the overall field distortion and also the effect of the electrode thickness in comparison to the other artefacts. Additionally, the effect of the electrode was extracted by subtracting the  $B_0$  distribution of the electrode-free from the results collected from the disk thickness sweep.

All plots show a similar field perturbation pattern as the result of the electrodes. The difference between the field distributions is the intensity of the perturbations. Figure 3.2.i reports the standard deviation and the average of the field perturbations corresponding to the electrode thickness. The linear distribution of these parameters suggests that the field



**Figure 3.2:**  $B_0$  distribution in presence of the disk electrode with different thickness (100 nm, 200 nm, 300 nm, and 400 nm) and considering distortions from other components of the coil and inserts (a-d). Subtracting the distortions of the electrode-free case from the previous values shows the effect of the electrodes (e-h). These simulations reveal that distortions are a linear function of the electrode thickness and the corresponding values for the other thicknesses can be achieved by interpolating the data (i).

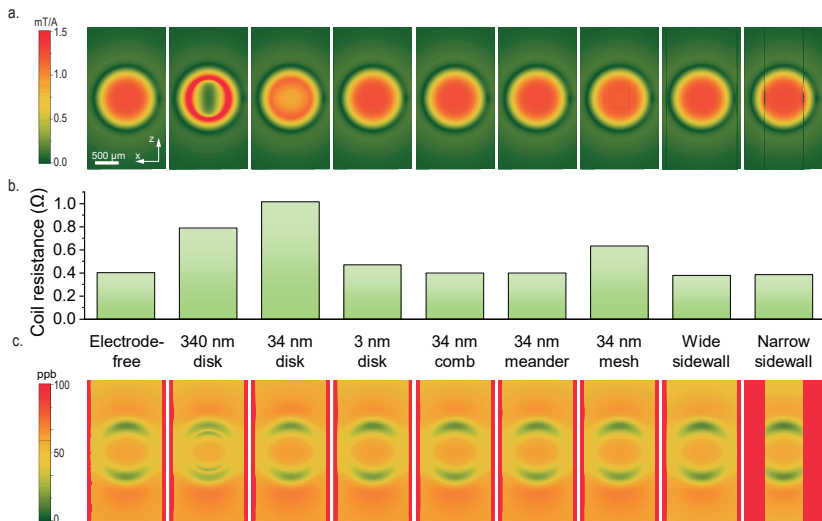
perturbation for electrode thickness of 34 nm or 3 nm can be interpolated and hence the overall  $B_0$  distribution can be back-calculated. A similar approach was utilised to calculate the field distribution in mesh, meander, and comb planar structures.

In the simulations, the material for the metallic structures was assumed to be gold whereas, in the actual experiments, a chromium layer serves as the adhesion layer between the gold and the glass substrate, as discussed in Section 3.4.

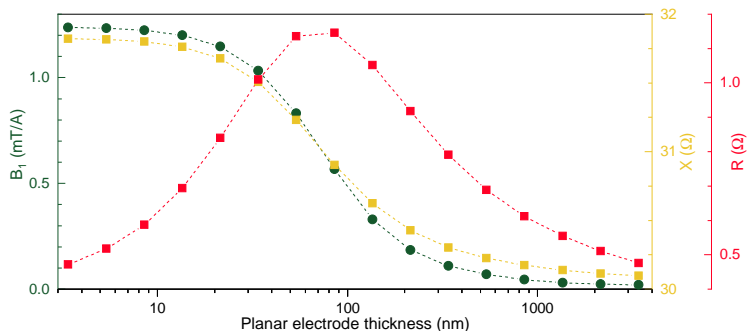
### 3.3.3 Simulation results

#### RF simulations

Figure 3.3 presents the component of  $B_1$  field, which is perpendicular to  $B_0$ , at the  $xz$ -plane (at the middle of the channel). For an electrode-free insert,  $B_1$  has a 2D parabolic distribution. By adding a metallic planar structure, the field is depleted from the centre of the disk and focused at the edges to encompass the electrode. The net penetrated field inside the metallic structures depends on the resistance of the electrode. A thicker electrode provides less resistance against the induced current and exhibits more distortions. Additionally, some components of the RF field are flipped along the  $B_0$  and hence do not contribute to the signal. The ellipsoidal shape of the depletion region corresponds to the same fact.



**Figure 3.3:** Simulation results for different electrode geometries. a. RF field distribution. b. The resistance of the HH coil considering the effect of the electrodes. c. Relative  $B_0$  distribution.



**Figure 3.4:** RF simulation for the film thickness sweep reveals that there is a critical thickness ( $\sim 90$  nm in this case) at which the total power dissipation in the disk electrode is maximum. For thickness lower than the critical thickness, a large portion of the field penetrates through the electrode and for thickness more than the critical thickness, the field is mainly blocked.

The effect of the electrode thickness on the RF field distribution and impedance of the coil is studied in more detail by sweeping the disk thickness within 3.4–3400 nm range in a logarithmic scale. The RF field at  $40\ \mu\text{m}$  above the centre of the electrode was probed and plotted in Figure 3.4 together with the impedance of the coil. According to these results, the coil resistance is maximised for the electrode thickness about 90 nm. The thickness of the maximum resistance coincides with the thickness at which the observed magnetic field is half of the field in the electrode-free case. This behaviour is attributed to the critical thickness of the metallic layer. For this thickness, the power dissipation is maximum due to both penetration depth of the field and decoupling between two coils.

The ultra-thin disk and patterned planar structures are almost transparent to the RF field as the induced current in those structures is small. The wide-channel sidewall insert acts similar to the electrode-free version. A shallow strip, located at the channel edges, corresponds to the sidewall electrodes. The narrow channel sidewall crops the pattern and slightly improves the field distribution inside the channel. The fields circumventing the sidewalls are partially directed inside the channel and contributed to the total field amplitude as well as its uniformity.

The impedance of the coil in the presence of different electrode configurations is another useful piece of information to be studied. The impedance, reads at the coil's port, depends on the mutual inductive coupling between two coil lobes, inductive coupling between the coil and the metallic structures, as well as, the total power dissipation in the electrode. As the result, 34 nm disk and 34 nm mesh electrodes cause higher resistances at the coil ports. The resistance also represents the total noise collected by the coil.

### Susceptibility simulations

Figure 3.3.c summarises  $B_0$  distribution for different configurations at  $xz$ -plane (at the middle of the channel). A pair of round-bracket patterns, which stems from the coil loops, is observable in all structures. The brackets are bolder at the locations, where the loop edge is perpendicular to  $B_0$ . The electrode-free insert has been optimised to introduce the minimum susceptibility mismatch by extending it along  $B_0$  [149]. As explained in Section 3.3.2, a planar electrode perturbs the field so that: i) it forms a disk with lower susceptibility corresponding to the electrode location; ii) it produces a secondary pair of brackets, having higher susceptibility values, beyond the electrode edges. Superposition of the perturbations forms the field pattern of the planar electrodes. The perturbations introduced by the 34 nm- and 3 nm-thick structures are dominated by the background distortions, made by the coil loops, and no obvious perturbation is distinguishable.

Similar to the 34 nm-thick disk electrode, the effect of the 34 nm-thick mesh, meander and comb electrodes are negligible in  $B_0$  field plot. It should be emphasised that even a minor perturbation, if coinciding with high amplitude  $B_1$  field, can play a significant role in the NMR performance.

The sidewall electrodes perturb the static field locally. This perturbation is minimised because of the electrodes extending along  $B_0$ . For the wide-channel structure, the perturbation is pushed further outside the detection region. Never-

theless, the narrow channel eliminates some parts of the distortions, generated by the coil, and improves the overall  $B_0$  uniformity.

### 3.3.4 Post-processing the simulation data

Although the field plots and the raw simulation data are very informative to understand the underlying phenomena at the physical level, the actual device performance cannot be interpreted from an ordinary representation of the information. Accordingly, the figures of merit discussed in Section 2.3 are employed to study and compare different designs. For this purpose, the simulation results have been post-processed by MATLAB® R2018a (MathWorks Inc., USA) to produce the *Digital Twins* of the NMR figures of merit.

According to Equation 2.10, normalised  $\xi$  can be defined as  $\xi_M(\tau) = \xi(\tau)/\omega_0 M$  so that the amplitude of the calculated signal is independent of the sample and the Larmor frequency. This parameter is considered as a measure for the signal amplitude in the simulations. By sweeping the length of the excitation pulse ( $\tau$ ), the nutation signal can be achieved.

For each insert geometry,  $B_{1u}$  values at the sample volume were extracted with a sampling rate of 10  $\mu\text{m}$  and imported in MATLAB® R2018a (Mathworks Inc., USA) as a vector called  $\underline{B}_{1u}(n \times 1)$ . The time span for the nutation spectra is considered as  $\underline{\tau}(1 \times m)$ . For an arbitrary applied power ( $P$ ) by the amplifiers, the nutation signal can be represented in a vector format as:

$$\underline{\xi}_M = \underline{B}_{1u}^T \sin\left(\gamma \sqrt{\frac{P}{r_{coil}}} \underline{B}_{1u} \underline{\tau}\right) \quad (3.3)$$

The  $90^\circ$  pulse is defined as  $\tau_{\pi/2} = \tau(\arg \max(\underline{\xi}_M))$ . The excitation efficiency is calculated then accordingly as  $ef = \pi/2 \times \tau_{\pi/2}$ . The relative SNR can also be calculated as  $SNR_{rel} = \max(\underline{\xi}_M) / \sqrt{r_{coil}}$ . The impedance of the coil ( $r_{coil}$ ) is simulated in the loaded condition, i.e. in presence of the sample and electrodes. Therefore, the total power dissipation in the insert is also included in the calculations.  $B_1$  homogeneity is also calculated as the ratio between the signal amplitude at  $450^\circ$

pulse (second maxima of  $\underline{\xi}_M$ ) and the signal amplitude at  $90^\circ$  pulse (maximum of  $\underline{\xi}_M$ ).

In order to calculate the spectral resolution, both susceptibility and RF simulations are required. The final FID signal, induced in the coil, is the superposition of all the elementary signals from each sample voxel. The elementary signals, following the  $90^\circ$  pulse, are calculated according to Equation 2.10. In the frequency domain, it corresponds to a Lorentzian signal centred at  $2\pi\gamma B_0(x, y, z)$  and linewidth equal to  $T_2$  and the amplitude of the signal is proportional to  $\underline{B}_{1u}(x, y, z) \sin(\gamma\sqrt{P/r_{coil}}\underline{B}_{1u}(x, y, z)\tau_{\pi/2})$ . Ignoring the  $T_2$  relaxation time, the signal can be illustrated with a bar chart where the location of the sticks correspond to the chemical shift and their height correspond to the total effective RF field of the voxels sharing the same static field. In this case, the simulated results do not consider the shim compensation and assume a perfectly uniform  $B_0$  in absence of the coil and the insert. The simulations also exclude the effect of the detector chip, PCB, capacitors, and the probehead.

### 3.3.5 Evaluation of different configurations

This section presents and studies the calculated figures of merit, achieved from the simulation results, and discusses different insert geometries. Based on these comparisons, the best geometries are selected for the fabrication and experimental evaluation.

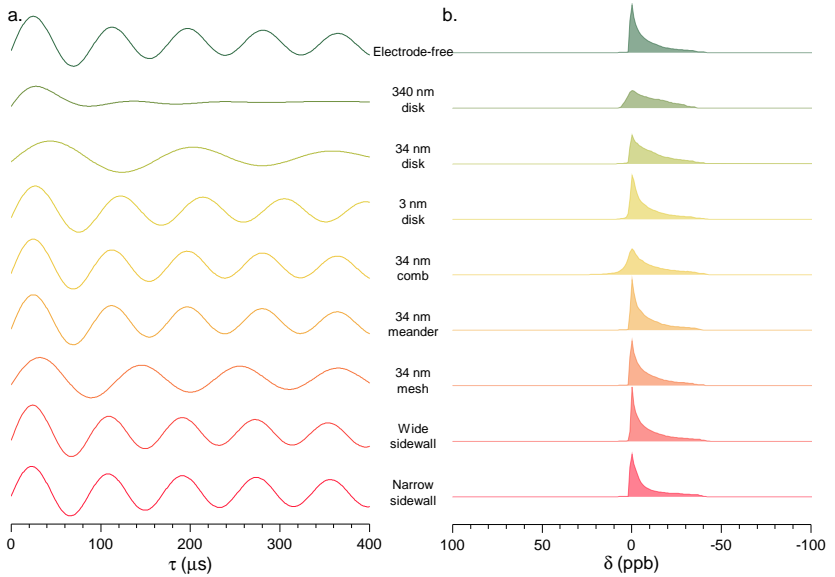
The nutation signals achieved using the simulations are depicted in Figure 3.5.a. Accordingly, the excitation efficiency, the field homogeneity, and the relative SNR values are extracted and listed in Table 3.2. The 340 nm-thick electrode distorts  $B_1$  field significantly and the nutation signal decays very fast. The narrow channel sidewall geometry outperforms the other geometries in terms of the field homogeneity and the excitation efficiency. It is attributed to the flux compression between the electrodes and also restricting the channel to a smaller width. The rest of the structures show an almost similar decay in the nutation signal. The 34 nm-thick disk and mesh structures require the longest  $90^\circ$  pulse.

It is in agreement with the results of the impedance and field distribution as a function of the electrode thickness presented in Figure 3.3 and 3.4.

The relative SNR is scaled with respect to the electrode-free case to simplify the comparison. The 340 nm-thick electrode has the poorest performance because of both  $B_1$  field being depleted from the centre of the electrode and additional noise introduced by the electrodes. In the 34 nm-thick electrode, noise contribution plays a major role in SNR degradation. The narrow-channel sidewall has the best performance thanks to constraining the sample inside the narrow channel and the slight enhancement of the field amplitude at the vicinity of the electrodes. This configuration is especially interesting for the applications, which monitor the reactions happening close to the electrode surface. The slightly lower sensitivities in the 34 nm-thick disk, meander, mesh, comb, and wide-channel sidewall structures in comparison to the electrode-free case are attributed to the power dissipation in the electrodes. It implies that, although some field perturbations were introduced, they did not impair the sensitivity of the system. The NMR spectra for different structures are presented in Figure 3.5.b. The spectral resolution for each geometry is calculated and presented in Table 3.2. The results were scaled for the same noise level in order to facilitate the SNR comparison. The spectrum of the electrode-free insert has a long tail in the lower chemical shift side. It is attributed to the field distortions caused by the coil lobes. At the locations corresponding to the round bracket  $B_0$  artefacts,  $B_1$  field is weak and the collected signal from those voxels generate the one-sided line broadening pattern.

Although  $B_0$  distribution in the planar structures is very similar to that of the electrode-free, the spectral resolution suffers from the electrode thickness. It is mainly because of the relative distribution of  $B_1$  with respect to  $B_0$ . By increasing the thickness of the planar electrodes, the RF field is more concentrated on the periphery, where  $B_0$  experiences perturbations. Therefore, the signal, corresponding to the peripheral voxels, is amplified and the spectral resolution is degraded. As expected, patterning the planar electrode enhances its performance in comparison to the disk electrode with the same thickness. It is achieved by





**Figure 3.5:** a. The nutation signals reconstructed from the simulations for different electrode geometries; b. The NMR spectra reconstructed from the simulations for different electrode geometries.


increasing the resistance against the induced current and allowing more field penetrating through the channel floor. The comb structure shows a relatively wider spectrum, compared to the other geometries. It corresponds to the relative position of the sampling points which coincide with the edges of the electrodes. Sidewall electrode geometries have similar performance with respect to the electrode-free case in terms of linewidth.

### 3.4 Fabrication




Based on the simulation results, four different electrode configurations were selected for further analysis. These four inserts are: 34 nm-thick disk electrode, 3 nm-thick disk electrode, wide-channel sidewall electrode, and narrow channel sidewall electrode. Further geometrical details of these inserts are given in

**Table 3.2:** The simulated figures of merit for different electrode configurations.

Configurations	$ef$ (krad/sec)	$A_{450}/A_{90}$ (%)	$S_{rel}$ (%)	FWHM (Hz)
Electrode-free	62.8	68	100	2.14
340 nm-thick disk	56.1	25	86.4	8.30
34 nm-thick disk	49.1	70	94.9	4.51
3 nm-thick disk	58.2	68	99.4	2.31
34 nm-thick comb	62.8	68	100	2.68
34 nm-thick meander	62.8	68	98.9	2.27
34 nm-thick mesh	49.1	71	97.7	2.21
Wide-channel sidewall	65.4	68	99.0	2.09
Narrow-channel sidewall	68.3	75	154.8	2.29

Section A3. Together with these configurations, an electrode-free structure was also fabricated as the reference for the comparison. These five inserts can be divided into three groups in terms of the fabrication process. The fabrication process for each group is explained in the following sections. Further details of the fabrication steps, marked with , are given in Section A2.

### 3.4.1 Electrode-free insert

The fabrication process of the electrode-free insert is depicted in Figure 3.6.a. The process started with cleaning and dehydration bake of a 4 inch, 210  $\mu\text{m}$ -thick MEMpax® wafer (SCHOTT glass, Malaysia) as the bottom substrate. For this purpose, the wafer was rinsed with isopropanol (IPA) and Acetone and exposed to the plasma cleaning process  (RIE plasma etcher Etchlab 200, SENTECH Instruments GmbH) for 10 min followed by 5 min dehydration bake on the hotplate at 200 °C. The wafer was coated  with a 90  $\mu\text{m}$ -thick layer of SU-8 3025 using the spincoater (PRIMUS STT 15, ATMvision AG) followed by softbake .

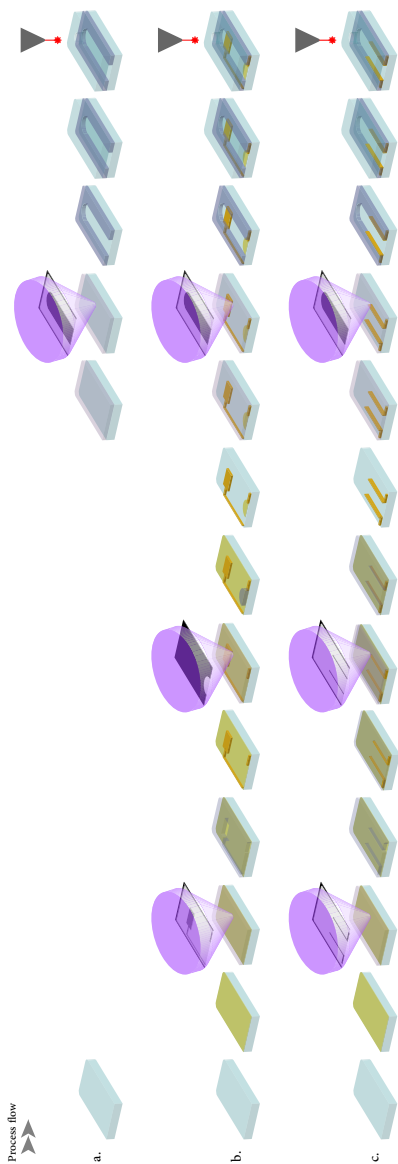
The channel design, to be transferred to the photoresist, was drawn using LayoutEditor® and printed on the transparent foils with 12 µm resolution. The photoresist was exposed to UV (wavelength 365 nm) through the mask for 370 mJ cm<sup>-2</sup> dose using the mask aligner (EVG 620®, EV Group). The post exposure bake<sup>☐</sup> was performed at 65 °C to reduce any stress in the structures. The wafer was stirred in PGMEA solvent for 40 min in order to develop the unexposed photoresist. 10 min stirring in IPA was applied afterwards to dissolve PGMEA residues. The wafer was rinsed with DI-water and dried in the convection oven at 30 °C for 600 min.

The bonding was achieved using a 5 µm-thick SU-8 as the adhesive medium. For this purpose, SU-8 3005 was coated on a second 4 inch, 210 µm-thick MEMpax® wafer, cleaned with the same protocol discussed earlier. The photoresist was spincoated<sup>☐</sup> and partially baked<sup>☐</sup> on the hotplate. The partial bake leaves the surface of the photoresist ready to bond to the other wafer whereas the photoresist maintains its uniform distribution under high pressure and temperature conditions, experienced during the bonding procedure. The coated sides of the two wafers were brought into contact and the assembly was left for compression bonding<sup>☐</sup> using (EVG 510®, EV Groups).

The assembly was exposed with 300 mJ cm<sup>-2</sup> afterwards to enhance its mechanical and chemical stability followed by a baking process at 90 °C for 240 min. The in-/outlets of chips were drilled using nanosecond Laser (PIRANHA® ACSYS) and the assembly was diced into individual chips with the same Laser.

### 3.4.2 Planar-electrode inserts

The fabrication process of the planar electrode inserts is similar to the electrode-free insert except for a few intermediate steps to introduce and pattern the metallic structures, as shown in Figure 3.6. After the initial cleaning step, a chromium/gold seed layer was deposited on the wafer. The thickness of the layer was set based on the electrode thickness, either 1/2 nm or 10/25 nm, respectively. The wafer surface was cleaned again with the same protocol. The



**Figure 3.6:** a. The fabrication process of the electrode-free insert employing one lithography step to pattern the channels followed by bonding to the top wafer and dicing.; b. The fabrication process of the planar-electrode inserts employing two metallisation steps, and three lithography steps, followed by bonding and dicing. c. The fabrication process of the sidewall electrode inserts employing three metallisation steps, and three lithography steps, followed by bonding and dicing.

counter electrodes, access pads, and connecting tracks were fabricated using gold electroplating. For this purpose, the corresponding mask was designed as discussed before. A 5  $\mu\text{m}$ -thick SU-8 3005 was spincoated<sup>Ⓜ</sup> on the seed layer. It was baked at 95 °C for 10 min followed by exposure with 300  $\text{mJ cm}^{-2}$  and post-exposure bake at 95 °C for 2 min. The unexposed photoresist was developed by leaving the wafer in PGMEA for 10 min and rinsing that with IPA and DI-water. After dehydration, pulsed electroplating<sup>Ⓜ</sup> was performed for the target height of 5  $\mu\text{m}$  during 96 min.

After that, the mould was stripped using O<sub>2</sub>-Plasma technique<sup>Ⓜ</sup> for 30 min. The wafer was cleaned with the protocol mentioned earlier and a 20  $\mu\text{m}$ -thick SU-8 3025 was spincoated<sup>Ⓜ</sup> on the wafer. Softbake was performed for 15 min at 95 °C. A second mask was prepared to pattern the photoresist and to develop the active electrodes through the seed layer. The wafer was exposed through that mask with 330  $\text{mJ cm}^{-2}$  and was baked at 95 °C for 4 min. The development step was performed by stirring the wafer in PGMEA for 20 min and rinsing it with IPA and DI-water. Then, gold and chromium seed layers of the unprotected parts were etched using a chemical etching method. For this purpose, the wafer was stirred in gold etchant (KI: I<sub>2</sub>: H<sub>2</sub>O 100 g: 25 g: 1 l) and Cr-200® (MicroChemicals, Germany), respectively. The photoresist was stripped using O<sub>2</sub>-Plasma<sup>Ⓜ</sup> for 90 min. The wafer was further processed as of a bare wafer in the electrode-free insert fabrication process.

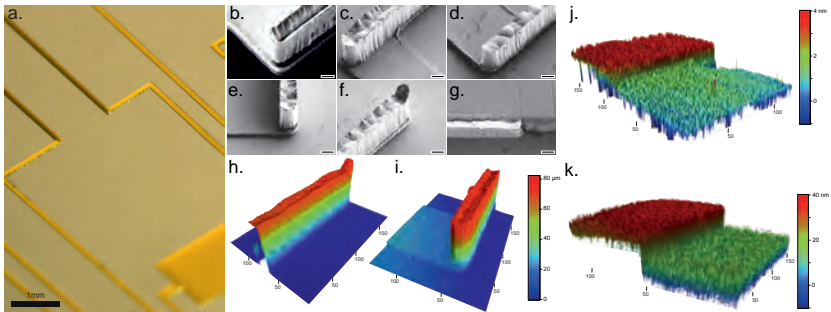
### 3.4.3 Sidewall-electrode inserts

The sidewall electrodes were manufactured by gold electroplating as depicted in Figure 3.6. The fabrication of these inserts started with spincoating<sup>Ⓜ</sup> SU-8 3025 on a wafer covered with 20/60  $\mu\text{m}$  chromium/gold seed layer. The wafer was then baked at 95 °C for 15 min. The photoresist was exposed through the mask for the first metallisation layer with an exposure dose of 330  $\text{mJ cm}^{-2}$  followed by baking at 95 °C for 4 min. The unexposed photoresist, corresponding to the pads, tracks, and the sidewall electrodes, was developed by stirring the wafer

in PGMEA for 20 min and rinsing with IPA and DI-water. After dehydration step, the structures were electroplated for the target height of 5  $\mu\text{m}$ . The mould for the second electroplating step was deposited on top of the first mould. In order to enhance the resolution of the structures and avoid reflections from the first electroplated gold layer, an anti-reflection coating was employed. For this purpose, AZ® Barli® -II 200 (MicroChemicals, Germany) was spincoated at 3000 rpm and baked at 200 °C for 1 min. Afterwards, 70  $\mu\text{m}$  SU-8 3025 was spincoated<sup>[1]</sup>. After softbake<sup>[2]</sup>, the wafer was exposed to 350  $\text{mJcm}^{-2}$  UV through a second mask and maintaining alignment to the first layer followed by post-exposure bake<sup>[3]</sup>. The unexposed regions, corresponding to the sidewall locations, were developed in PGMEA solution by applying 20 min ultrasound (SONOREX SUPER 10P, BANDELIN electronic GmbH & Co. KG) with 70 % power to accelerate the procedure and enhance the resolution. The wafer was stirred in IPA for 15 min, rinsed with DI-water, and left in the convection oven at 30 °C for 600 min. A plasma cleaning process<sup>[4]</sup> (RIE plasma etcher Etchlab 200, SENTECH Instruments GmbH) was applied for 10 min to remove the Barli layer in the openings. The sidewall structures were gold electroplated<sup>[5]</sup> for the target height of 80  $\mu\text{m}$ . The mould was stripped using O<sub>2</sub>-Plasma<sup>[6]</sup> for 360 min and the seed layers were etched, accordingly. The fabrication process was continued similar to the other inserts to form the channel, bond the top wafer, drill holes, and dice the assembly into individual chips.

## Fabrication challenges

**High aspect-ratio SU-8 mould:** Although more sophisticated techniques are available to resolve thin structures, e.g. Laser-, X-ray lithography, this work aimed to achieve these structures with low-cost MEMS techniques. The best resolution, which can be reliably achieved using the foil masks and UV exposure, is about 20  $\mu\text{m}$  for an aspect-ratio one or smaller. Increasing the photoresist thickness, for the case of the sidewall electrodes, exacerbates the light diffraction and degrades the resolution. Besides,



**Figure 3.7:** The sidewall electrodes were realised using two electroplating steps(a-i). A photograph of the sidewall electrodes in a narrow channel configuration (a). The SEM images of the electrodes (b-g). Characterisation of the electrodes with a white-light interferometre (h, i). Overexposure of the mould for the second electroplating layer leaves some photoresist residue at the bottom of the structures. The mould imperfection, being transferred to the electroplated layer, generates a V-neck at the junction of the two layers (b). The other imperfection is caused by a faster growth rate at the edges. It generates a cup shape electrode rather than a solid bar (b) or leaves some overplating at the corners (f, h). The microfluidic channel walls overlap with the electrode (g). The channel is slightly thicker to ensure proper bonding to the top cap. White-light interferometry images of the planar electrodes, being fabricated by patterning the PVD layer (j, k).

the electroplated gold layer underneath the mould reflects the light and increases the total exposure dose. Therefore, the edges of the mould are not sharp. A V-neck shape at the junction of the two electroplated layers was observed as the result (see Figure 3.7.b). This issue was minimised by optimising the exposure dose, and also employing an anti-reflection coating (AZ® Barli®-II, MicroChemicals, Germany), before the second mould being generated.

**Electroplating:** According to the measurements, the growth rate of the electroplated gold is higher at the edges and corners. This effect is more noticeable in the sidewall electrodes as depicted in Figure 3.7b, c, f, h, i. It is attributed to two facts: i) higher electric charge concentration at the corners; ii) O<sub>2</sub> plasma treatment attacking the seedlayer and deposition of gold particles on the walls of the mould. In order to compensate for

that, pulsed electroplating was employed and the plasma-treatment was modified.

**Thick SU-8:** The roughness of the thick SU-8 layer, used to pattern the channel, can degrade the bond quality. In the sidewall electrode configuration, the presence of the metallic structures projects more non-uniformity to the SU-8 encapsulation layer. Furthermore, some voids can form just behind the sidewalls because of the spincoating. In order to enhance the structure quality, a lower viscosity SU-8 (SU-8 3025) was used and the spincoating, as well as the soft-bake steps, were optimised accordingly. Figure 3.7.g shows an SU-8 layer formed employing these adjustments.

**Bonding:** Bonding wafers employing cured SU-8 has been demonstrated elsewhere [200]. However, the chemical and mechanical stability of the bond is not reliable. In addition, the roughness of the SU-8 layer impairs the bonding. In order to enhance the bond quality, a partially-cured SU-8 was employed. This layer was baked on the hotplate to leave the top surface of the SU-8 active. Therefore, the adhesion to the host substrate is preserved and it is still elastic enough to compensate for the roughness of the other surface. The bond pressure and temperature were adjusted to avoid any reflow or shred of the SU-8 layer. The assembly was exposed and baked afterwards to enhance the stability of the bond. The final parameters are listed in Section A2.

**Ultra-thin metallisation layer:** Forming an ultra-thin planar metallic layer using low-cost PVD techniques and considering the consistency of the layer was another challenge to overcome. In order to evaluate the deposited layer, its thickness, sheet resistance, and the atomic content of the substrate coated with these layers were measured. Figure 3.7.j, k show the profile measurements using white-light interferometry. Table 3.3 summarises the sheet resistance and atomic content measurements. The atomic contents were measured with Scanning Electron Microscopy /



**Table 3.3:** Characterisation of the nano-layers with white-light interferometry, sheet resistance measurement, and atomic content measurement.

	Nom. Cr thickness (nm)	Nom. Au thickness (nm)	Meas. thickness (nm)	Meas. sheet res. ( $\Omega \square^{-1}$ )	Cr atomic content (%)	Au atomic content (%)
34 nm	10	24	33	$1.0 \pm 0.1$	$2.38 \pm 0.10$	$4.75 \pm 0.10$
3 nm	1	2	3.5	$72 \pm 20$	$0.12 \pm 0.03$	$0.20 \pm 0.04$

Energy Dispersive X-Ray Spectroscopy (SEM/EDX). The electron interaction depth is  $2 \mu\text{m}$ . Therefore, the absolute contents of the chromium and gold are low. Nevertheless, the comparison between these values correlates with the sheet resistance and layer thickness measured using white-light interferometry.

### 3.5 Characterisation

The fabricated inserts (electrode-free insert, 34 nm- and 3 nm-thick disk electrodes, and wide- and narrow-channel sidewall electrodes) were tested using NMR spectroscopy and MR imaging to, on one hand, verify the simulation results and, on the other hand, explore their performance in the experimental conditions. The characterisation was performed using a stationary sample and without applying a signal to the electrodes. NMR spectroscopy presents the figures of merit without any insight to the local distribution of  $B_0$  and  $B_1$  fields whereas MRI complements it by providing a closer look at the system, reporting  $B_0$  and  $B_1$  map.

Both NMR and MRI measurements were performed using an 11.7434 T superconducting magnet (Bruker, Germany). The corresponding  $^1\text{H}$  resonant frequency is 500 MHz. As depicted in Figure 3.1, a Helmholtz detector, devel-

oped and fabricated by Spengler *et al.* [149] was employed as the NMR sensor. The coil was tuned to 500 MHz and matched to  $50\ \Omega$  using ceramic capacitors. The sample was loaded to the insert and the insert was slid inside the detector chip. The assembly was installed on the micro5 probehead (Bruker, Germany) with the aid of a PMMA adaptor and was connected to the probe circuit using two pins. The gradient sleeve was installed and fine tuning and matching were performed. Two adjustable capacitors, implemented in the probe, served for fine-adjustment of tuning and matching.

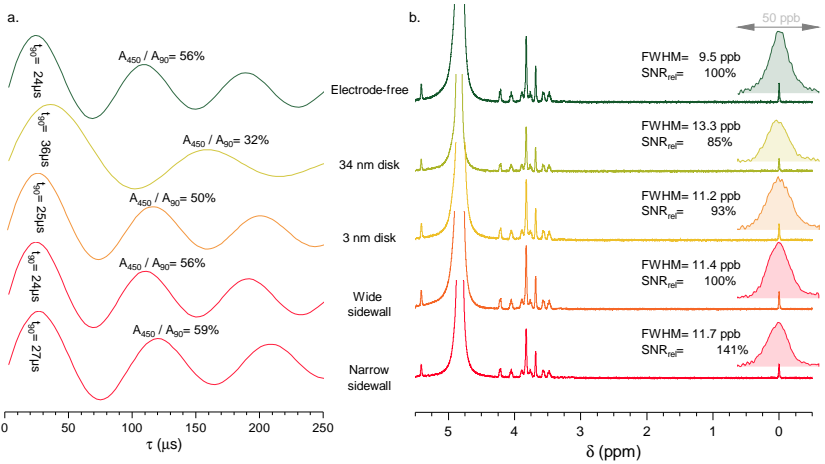
### 3.5.1 Sample preparation

A liquid sample consisting of 500 mM sucrose and 50 mM 3-(trimethylsilyl)propionic-2,2,3,3-d<sub>4</sub> acid sodium salt (TSP) dissolved in deionized water was prepared for the NMR measurements and  $B_1$  map experiments. TSP serves as the chemical shift reference. The sample used for  $B_0$  experiments consists of 4 mM copper sulphate ( $\text{CuSO}_4 \cdot 5\text{H}_2\text{O}$ ) and 75 mM sodium chloride (NaCl) in deionised water. All the chemicals were purchased from Sigma Aldrich® (Germany).

### 3.5.2 NMR

The NMR measurements were carried out using TopSpin 5.4 software (Bruker, Germany). The measurements were performed at 30 °C. The shimming was performed manually up to the second order shims. After sufficient shimming, the nutation signals were collected. 1D NMR experiments were performed by adjusting the pulse width to the 90° pulse calculated from the nutation experiments. Figure 3.8 presents the NMR measurement results.

**Nutation signal:** The water peak was considered as the reference for the nutation plot and the integral of each peak was calculated to eliminate the imperfections, stemming from poor shimming or radiation damping. The experiment was performed collecting one single scan for each cer-



**Figure 3.8:** a. Nutation signal of different electrode geometries collected from experiments. b. NMR spectra of different electrode geometries collected from experiments.

tain pulse length value. The pulse length increment was set to 1  $\mu\text{s}$ , the relaxation delay was set to 10 s, and maximum pulse length was 250  $\mu\text{s}$ .

The absolute values of the  $A_{450}/A_{90}$  parameter, collected from the measurements, are smaller than those from the simulation results. This difference is attributed to the detector imperfections, e.g. coil geometry, alignment of the Helmholtz pair, the distance between the pairs, and the effect of the metallic tracks, which feed the coil. The 34-nm-thick electrode geometry exhibits even lower  $B_1$  homogeneity as a result of  $B_0$  distortions, introduced by the electrode. For higher flip angles, the static field distortions induce phase distortion in the signals and accelerate the signal decay.  $B_1$  field homogeneity in the narrow-channel sidewall insert is slightly better than the electrode-free case which is in good agreement with the simulations.

In the experimental studies, tuning and/or matching can influence the delivered power to the coil and degrade the pulse width required for a  $90^\circ$  flip angle. Nonetheless, the measured values are in good agreement with

the simulation results except for the narrow-channel sidewall. Since the tuning and matching capacitors have limited adjustment ranges, a proper adjustment was not possible in this case and the power transfer efficiency was degraded, accordingly.

**NMR spectrum:** Each final spectrum is the average of 64 scans, each one consisting of 18000 datapoints over 20 ppm spectral width. The relaxation delay was set to 5 s and acquisition time was 0.9 s. The receiver gain was adjusted to 32. The SNR and the spectral resolution of the TSP peak were calculated as the reference for comparison.

The area under the TSP peak of each understudy geometry for a unit of sample volume divided by the noise level was calculated and its ratio to that of the electrode-free insert was reported as the relative SNR. These data confirm the sensitivity loss wherever the planar electrodes are introduced. As expected, the mass sensitivity was improved by restricting the sample to a narrower channel, corresponding to the higher RF field values, and compressing the magnetic flux between the electrodes.

The spectral resolution of the NMR signals denotes that the simplifying assumptions presumed during the simulations, e.g. ignoring  $B_0$  distortions introduced by the probehead components, capacitors, and soldering bumps, play a big role in the final results and shimming cannot compensate for all those imperfections. However, these effects have a uniform impact on all the geometries and the relative values are in agreement with the simulations.

### 3.5.3 MRI

MRI experiments were performed in order to achieve  $B_1$  and  $B_0$  field distributions at the sample volume and cross-check the NMR figures of merit. These experiments were conducted using ParaVision 6.0.1 (Bruker, Germany) at 30 °C. The experiments consist of two steps: i) automatic adjustments, controlled by

the software, such as frequency adjustment (adjusting the excitation frequency to the resonance frequency) and receiver gain adjustment; ii) MRI scan which were performed at the end using the scan parameters.

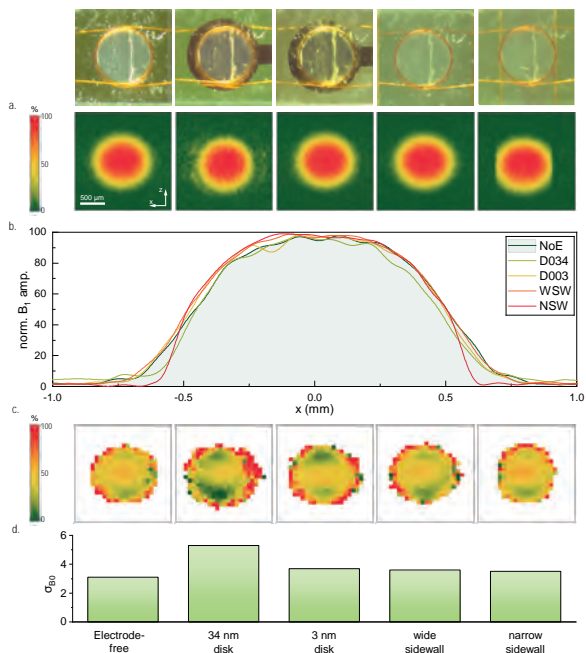
**FLASH** is a Gradient Echo (GE) sequence with a single excitation pulse. For a uniform sample distribution, the brightness of each pixel in the acquired image is a function of the average  $B_1$  in the corresponding voxel [201]. However, the field intensity is coded by a sinusoidal function meaning that the relation between the field amplitude and the voxel brightness for a uniformly distributed sample is

$$S \propto \frac{\sin(\theta)(1 - e^{-T_R/T_1})}{1 - e^{-T_R/T_1} \cos(\theta)} e^{-T_E/T_2^*} \sqrt{N_{ave}} \quad (3.4)$$

where  $\theta = \gamma B_{1u} I_{coil} \tau$  is the flip angle of each voxel,  $T_R$  is the repetition time,  $T_E$  is the echo time,  $T_1$  is the spin-lattice relaxation time, and  $T_2^*$  is the spin-spin relaxation time. For small flip angles, the field intensity at each voxel can be approximated by the slope of the signal of the voxel as a function of the flip angle.

For FLASH experiments, the scan parameters are set as: relaxation time (TR)= 200 ms, echo time (TE)= 4 ms, slice thickness= 100  $\mu\text{m}$ , in-plane resolution= 40  $\times$  40  $\mu\text{m}^2$ , scanning time= 53 min, averages= 512, bandwidth= 10 kHz, FOV= 2  $\times$  2  $\text{mm}^2$ , excitation pulse length= 1.1 ms. In order to calculate the flip angle of each voxel, five different experiments were performed at different power levels (0.3  $\mu\text{W}$ , 3.3  $\mu\text{W}$ , 9.4  $\mu\text{W}$ , 19.2  $\mu\text{W}$ , 33.6  $\mu\text{W}$ ). The images collected from these experiments are presented in Section A5. The collected data were post-processed in MATLAB® R2018a (Mathworks Inc., USA) to calculate the normalised  $B_1$  field distribution depicted in Figure 3.9.

As expected the noise level in 34 nm disk geometry is higher suggesting that the maximum signal amplitude is less. As the slice thickness is



**Figure 3.9:** MRI measurements depicting  $B_1$  (a,b) and  $B_0$  (c) field distributions at the sample region for different inserts. The standard deviation of  $B_0$  field (d) can be an indicator for the spectral resolution.

slightly larger than the sample thickness,  $B_1$  field plot represents the field averaged over the sample thickness. Nevertheless, the field distribution in 34 nm disk shows some halo patterns similar to its *digital twin*. The other four geometries have similar field patterns except in the narrow channel where the field pattern is cropped by the channel walls.

**Fieldmap** is a 3D GE sequence which uses a single pulse but reads the signal at two different echo times. The ratio of signal amplitude between these two read-outs depends on the susceptibility distortions in the voxel [24, 201, 202].

The scan parameters for Fieldmap experiments are as follows: relaxation time (TR)= 35 ms, first/second echo times (TE1/TE2)= 1.31/7.03 ms, isotropic voxel size= 90  $\mu\text{m}$ , scanning time= 76 min, averages= 128, bandwidth= 30 kHz, FOV=  $2.9 \times 2.9 \times 2.9 \text{ mm}^3$ , flip angle=  $50^\circ$ . SNR threshold was set to 5 to cut out the voxels with low SNR. The slices corresponding to the sample region were selected and presented in Figure 3.9.

According to the images, similar round-bracket shapes are observable in all field patterns. These results are consistent with the simulation results, i.e.  $B_0$  distortion as the result of the coil lobes. In addition, further distortions are observable in the 34 nm- and 3 nm-thick electrode structures which are attributed to the Cr adhesion layer under the gold electrodes.

In order to quantitatively analyse the static field distributions, the standard deviation of  $B_0$  field is presented in Figure 3.9. In the calculation of  $B_0$  field standard deviation, the pixels corresponding to the outermost rim of the images are eliminated as they suffer from poor signal-to-noise ratio. The standard deviation values are in good agreement with the spectral resolution presented in Figure 3.5.

## 3.6 Application

Chitosan (CS) is a stimuli-responsive biopolymer and it was the first biopolymer being electrodeposited. The CS gel is biocompatible, nontoxic, and antibacterial. Besides, the deposition is reversible, meaning that at low pH the CS primary amines are protonated which makes it soluble, whereas at high pH the amines are deprotonated and it is insoluble [203–205]. The functionality of the CS gel can be increased by either chemical modification or stacking the gel in multi-layer. All these features make chitosan a good candidate as the interface between soft-matter and solid, inorganic structures for bio-medical

applications. Moreover, the modified CS containing some chemical substrates can be employed to localise a chemical reaction. This approach has been widely used for enzyme studies [206].

The required pH gradient for the CS deposition can be produced using a pair of electrodes and an applied voltage between them. Then, the electrodeposition happens at the cathode electrode. Some reports studied deposition by measuring CS profile as a function of the applied current or deposition time, either by fluorescence microscopy methods, mechanical profile measurements, or some other indirect measurements [207–209]. The main constraint of those measurements is the interruption during the deposition for the measurements. Cheng *et al.* characterised CS-electrodeposition optically by observing the pH of the fluidic sample and the profile of the deposited gel [210]. It allowed them to have an online monitoring system and observe the on-going deposition process.

NMR spectroscopy can be employed as an alternative in order to monitor CS deposition without interrupting that, on one hand, the pH of the sample can be correlated to the chemical shift of the water peak. On the other hand, the gel generates a broader peak compared to its sol counterpart which can be observed with NMR. Therefore, NMR can report on both pH of the sample and gel volume. Additionally, it can report on the chemical reactions and physical phenomena happening during the deposition. Given NMR capabilities for monitoring chemical reactions, the localised reaction sites, provided by modified CS, unlock new opportunities for *in situ* NMR measurements.

In this study, the sidewall electrode and the 3 nm-thick disk electrode inserts were employed for three different experiments: i) monitoring CS deposition using NMR; ii) studying the gelation effect on the PEG signal of deposited CS, being modified with PEG; iii) observing a multiplex reaction, employing a stack of three layers of CS, each one being modified with a certain enzyme. These experiments were performed in collaboration with Nurdiana Nordin [211]. Further details of the experiments are discussed in the following subsections.



### 3.6.1 Monitoring *in situ* CS electrodeposition

#### Sample preparation

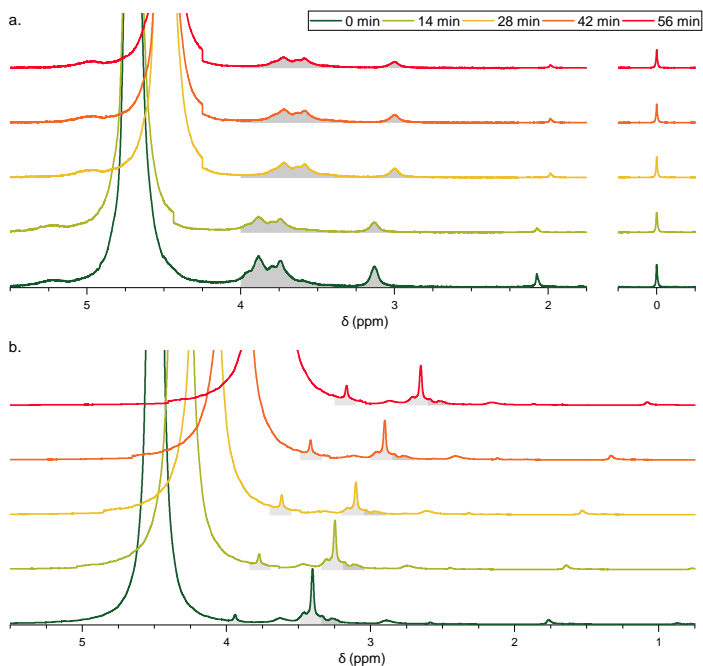
Electrodeposition was performed with two different CS samples: pure CS and chemically modified CS. In order to produce CS solution, 10 mM D<sub>2</sub>O based phosphate buffer solution (PBS) was prepared. pH of the solution was 7.4. The chitosan was then added to reach 1 % w/v concentration, maintaining the solution pH 3 by adding appropriate amount of deuterium chloride (DCl). After the CS was fully dissolved with the help of stirring, sodium deuterioxide (NaOD) was added to adjust the solution pH to 6. In the end, 50 mM trimethylsilylpropanoic acid (TSP) was added to the solution. Modification of CS was formed by coupling to polyethyleneglycol (PEG) with 1:1 CS:PEG molar ratio. PEG was activated using PEG:EDC:NHS (1:0.5:0.5) in deionised water. The solution was then added to the CS solution described before and allowed to proceed for 3 h. The solution was formed into hydrogel by adding NaOD followed by purification using extensive dialysis. The hydrogel was dissolved by adjusting pH 6 with the aid of DCl.

#### Experiment configuration

The sidewall electrodes were employed for these experiments. The electrodeposition was performed using a continuous current density of  $3 \mu\text{A mm}^{-2}$ . For this purpose, a voltage source was connected to the electrodes through a resistor. The current was measured and the voltage was adjusted so that the current reaches  $12.6 \mu\text{A}$  (electrode area  $\times$  current density).

#### NMR experiment and results

The NMR experiment was set up before applying current and the same adjustments were preserved for the whole experiment. Afterwards, the current was applied and the measurements were performed with 14 min intervals (5 min delay and 9 min NMR experiment).



**Figure 3.10:** Monitoring CS electrodeposition using sidewall electrodes for an unmodified CS sample (a) and CS coupled to PEG (b). The highlighted segment in a represent CS signal. PEG signal in b is highlighted.

CS generates NMR signal within 3–4 ppm as depicted in Figure 3.10.a. The linewidth of the CS signal increases with the deposited layer volume. It attributes to the lower molecular motion in the hydrogel state in comparison to the liquid state. PEG has an NMR signal around 3.3 ppm and 3.9 ppm (see Figure 3.10.b). The signal amplitude and linewidth of PEG are independent of the deposition. It is attributed to the free movement of the PEG molecules inside the CS gel. Free movement of PEG, makes it a good candidate for attaching molecules to CS. In this case, the attached molecules are decoupled from the unwanted line-broadening effects of the deposited hydrogel.

### 3.6.2 Multiplexed sensing

#### Sample preparation

200 mM sodium acetate (NaAc) was produced with NaAc tablets in deuterated ( $D_2O$ ) water and the pH was adjusted using deuterium chloride (DCI), and deuterium sodium hydroxide (NaOD). 50 mM TSP was added to this buffer as the reference for the quantitative analysis. All enzymes, modified-CS solutions, and dilutions used this buffer to maintain pH 5.5 for solution and pH 7 for hydrogel.

#### Experiment configuration

The experiment was performed with both ultrathin and narrow-channel sidewall insert geometries. The insert, employing the planar electrode, is adjusted so that the electrode does not coincide with the NMR region of interest but is slightly upstream. The insert with the sidewall electrode is used in its normal configuration (region of interest coincides with the middle of the channel and between two electrodes). Except for the sample volumes and the current amplitudes, the rest of the experiments were identical for both insert geometries.

The gel stack consists of three layers. The first layer contains urease coupled with CSPEG, whereas catalase coupled with CSPEG forms the second layer and glucose oxidase coupled with CSPEG forms the third layer. Each layer was deposited using a continuous current density of  $3 \mu A mm^{-2}$  for 15 min. After each deposition step and in order to stabilise the gels a solution of 200 mM NaAc was injected to the channel and later the channel was rinsed with  $D_2O$ . The reactions were activated by injecting the substrate solution containing 1000 mM urea, 100 mM D-glucose, 200 mM NaAc, and 200 mM TSP at pH 7.

The  $^1H$  NMR spectra were collected at  $\sim 17$  min intervals. The concentration of urea, D-gluconic acid, and D-glucose were calculated from the integral of their corresponding NMR peaks to monitor the reaction. Accordingly, the kinetic data were extracted.

## NMR experiment and results

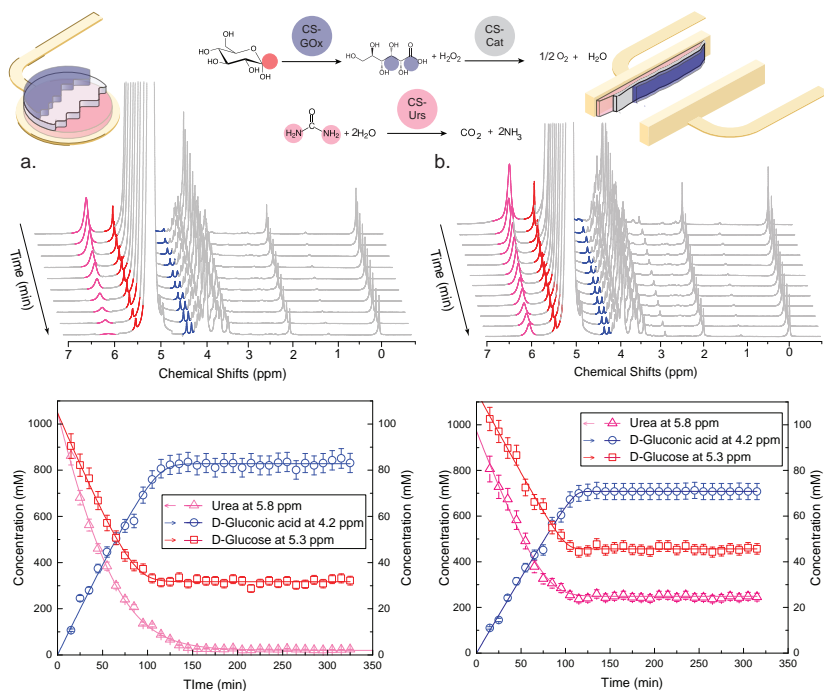
As illustrated in Figure 3.11, the oxygen production in catalase layer (second layer) depends on the hydrogen peroxide production in glucose oxidase layer (third layer) whereas these reactions are independent of the ureas reaction.

The reaction kinetics (derived from Michaelis-Menten equation) of this multiplexed experiment are in agreement with the single layer individual experiments [211], [HD5]. These results reveal that the hydrogel layers are independent and simultaneous reactions do not interfere each other. Besides, both electrode geometries show similar enzymatic activities in multi-layered hydrogels. Nevertheless, there is a small difference between the results collected from two experiments. The experiment with the sidewall electrodes reaches to the saturation state faster than the experiment with the planar electrode. It indicate an incomplete conversion because of the larger ratio ( $5\times$ ) of substrate (urea) to the active units in the sidewall case with respect to the planar electrode.

## 3.7 Discussion and conclusion

In this work, we have introduced different electrochemistry cells consisting of a pair of electrodes and a microfluidic channel, being compatible with Helmholtz NMR detector introduced by Spengler [62, 149]. The effect of different electrode structures on the NMR figures of merit have been studied and the best architectures have been fabricated. Microfabrication techniques enabled us to precisely control the geometry of the electrodes (e.g, thickness, width, and location). The performance of the fabricated cells was investigated with NMR experiments. The insert employing a pair of metallic sidewalls outperforms the other designs as predicted by the simulations.

The narrow-channel sidewall electrodes and the ultrathin planar electrodes were employed in three different applications as the proof of concept to evaluate the performance of the insert in an *in situ* electrochemistry experiments. This work



**Figure 3.11:** Monitoring multiplexed enzyme reactions employing two different electrode geometries (a: ultra-thin planar electrode, b: narrow-channel sidewall electrode) and with ureas, glucose oxidase, and catalase coupled to CSPEG. The figure is reproduced from [HD5].

is the very first demonstration of the micro-NMR being employed to monitor electrochemistry experiments inside a micro-cell.

The other achievement of this work is to develop a method to study and evaluate different electrode configurations in the NMR experiments relying on the FEM simulations. While most of the previous studies rely on the raw simulations data, in this work we have successfully demonstrated that those data can be further processed to achieve NMR figures of merit. A remarkable agreement between the simulated and measured NMR figures of merit confirms that the "Digital Twin" of the NMR experiments can play an important role in future NMR hardware development.

### 3.7.1 Challenges

Presence of the metallic electrodes inside the NMR field of view introduces both  $B_0$  and  $B_1$  field distortions. One solution to minimise these distortions is to reduce the thickness of those electrodes. However, it is not compatible with many applications, requiring high current densities. Another challenge is the fabrication of those thin electrodes. Instead, we have introduced a novel structure employing two sidewalls parallel to both  $B_0$  and  $B_1$  fields to reduce the distortions. This configuration requires high aspect ratio metallic structures precisely aligned with the channel. Integration of those structures was the main challenge to overcome.

### 3.7.2 Suggestions

A true electrochemistry cell requires three electrodes with more sophisticated electrode materials. Compatibility of those electrodes to the microfabrication techniques is the main requirement to fulfil. In addition, it requires a more complex fabrication process to introduce different types of electrodes.

The insert has demonstrated an interesting performance in the enzyme-coupled experiments. To further enhance the performance of the insert, an array of addressable electrodes can be employed to generate an arbitrary 3D gel structure and facilitate more complex experiments or to mimic biological organ- or body-on-a-chip systems as interesting subjects for NMR studies.

Another interesting application which can benefit from this research lies in the conjunction of NMR and energy storage field. Electrolyte or dielectric samples can be easily introduced in the current insert and the performance of the batteries or capacitors employing those media can be studied, accordingly. These designs would be great tools for those studies since the filling factor and the field amplitude are maximised in this case.

This design can also readily be utilised to monitor and drive electrophoresis or dielectrophoresis phenomena with NMR experiments. The compactness of the electrodes results in a lower required voltage for a certain electric field.

Additionally, thanks to the electrode geometries of the sidewall inserts, the electric field can be perfectly homogeneous in the channel. The design can be modified to produce different electric field patterns with different amplitudes. In order to reduce the footprint of the sidewall electrodes, one can realise the high aspect ratio electrodes using sputtered thin films on a sacrificial layer. With that technique, the electrode thickness can be reduced to a few nanometers. In this case, the power dissipation in the electrode and additional noise corresponding to the electrodes can be eliminated.





## 4 Broadband spiral micro-coils

### 4.1 Overview

The opportunity to "look" at a sample from different perspectives has always been a wish to fulfil in different spectroscopic methods. While it is usually achievable by correlative measurements, i.e. employing multiple spectroscopic techniques, some spectroscopic methods are capable of giving a multi-dimensional perspective. NMR is amongst those spectroscopy methods which can- theoretically- provide a multi-dimensional observation, opportunity thanks to its multi-nuclear detection. In this case, the sample is examined at different Larmor frequencies corresponding to different isotopes. However, the main bottleneck is the detection hardware. In this study, we re-evaluate and offer a novel type of NMR detector, i.e. broadband detector, which can collect data from the sample at different frequencies. Although this technique is at its early stages, the results show that this method has a performance comparable to the well-established resonance-based methods.

This chapter begins with a brief review of the micro-NMR techniques and the opportunities and challenges associated with that by focusing on multi-nuclear NMR. The chapter continues with discussing the figures of merit. Based on these figures of merit, the broadband detector performance is evaluated, simulated, and optimised for the given sample and at the desired working frequency ranges. In the next step, the fabrication process of the detector is presented together with the characterisation of the coil. The chapter is then concluded by comparing the proposed coil with the state of the art.

The primary results of this work were presented in **Euromar 2018** as a poster contribution. The final results of this work together with the optimisation and fab-

rication details have been published in **Scientific Reports (Nature Springer)** journal [HD3].

## 4.2 Introduction

As discussed in Section 2.4, micro-NMR is a technique to study micro-volume samples using NMR spectroscopy. For this purpose, miniaturised coils are usually employed to enhance the filling factor, increase the sensitivity of the coil, and reduce the noise. The term micro-coil refers to these miniaturised coils with sub-mm dimensions.

In addition to their popularity for the applications dealing with minute/precious samples, micro-coils are especially interesting in high static fields. In this case, the available space in the magnet bores is usually smaller and, besides, the micro-coils exhibit self-resonant frequencies higher than the Larmor frequency of the nuclei.

According to the discussion in Section 2.4, the power transfer between the micro-coil and the other circuits is a challenge to be considered. This challenge worsens when these coils are employed for the detection of more than one nucleus. As discussed in Section 2.5, usually trap and tank circuits are required to produce a multi-resonant circuit. These circuits, consisting of inductors and capacitors, introduce power loss which reduces the delivered power to the coil or partially dissipates the signal collected from the nuclei. Besides, these circuits introduce noise to the detected signal, while conducting it through the corresponding path. The complexity of the circuit rapidly increases with the number of the detection frequencies and the efficiency of the circuit drops, accordingly. Since micro-coils have smaller impedance and the collected signal is also smaller because of a smaller sample volume, the power loss and the additional noise are more critical in micro-domain rather than the standard multinuclear NMR experiments.

Employing elements with high quality-factor is crucial when designing and developing the trap/tank circuit for micro-NMR applications. Another possible

solution to enhance the overall multi-nuclear micro-NMR performance is to make the circuit compact in order to avoid long signal paths. Nevertheless, it contradicts the spectral resolution and  $B_0$  uniformity requirements since all these nearby elements contribute to the susceptibility mismatches.

Altogether, the susceptibility and power transfer efficiency issues limit the application of multi-nuclear micro-NMR. Consequently, a few studies tried to explore more than two nuclei [66, 67, 75, 77] and most of the literature is restricted to single or double resonant micro-coils [41, 45, 60, 93, 94, 97].

As a solution to the susceptibility issues and the power transfer challenges Webb [10] proposed to couple the micro-coil to a macro-coil. With that, the impedance of the macro-coil governs the power transfer efficiency and the tuning/matching elements can be kept relatively far from the detection zone hence improve the spectral resolution. Nevertheless, for a multi-resonant circuit, the challenge is to maintain an efficient inductive coupling matrix with different over- and loosely-coupled tank circuits. A double resonant magic angle coil spinning (MACS) was developed by Inukai [121] using two interconnected tank circuits inductively coupled to a commercially available triple resonance magic angle spinning (MAS) coil (see Figure 4.1). Working based on a similar inductive coupling concept, Lenz lens structures are wideband, passive inserts which focus the flux at the sample region [50–52]. Chapter 5 discusses these solutions in more details.

Amongst the multi-resonant circuits for the micro-coils, the pre-tuned configuration is the most popular method. In this way, the impedance of the micro-coil is boosted to enhance the power transfer efficiency [41, 45, 75]. As depicted in Figure 4.1, pre-tuning is usually provided by a capacitor. As a result, trap or tank circuits can be pushed further away from the detection zone and  $B_0$  or  $B_1$  perturbations can be suppressed. In a different report, Kc [60] examined impedance transfer employing transmission lines. In addition, sample spinning was employed in case even higher  $B_0$  and  $B_1$  homogeneities are required [66, 67, 77, 94].



**Figure 4.1:** a. Inukai [121] suggested a double resonant MACS employing two tank circuits coupled to a MAS coil. b. Oosthoek-de Vries [45] developed trap circuits for a micro-stripline coil. The figure is reproduced from [HD1].

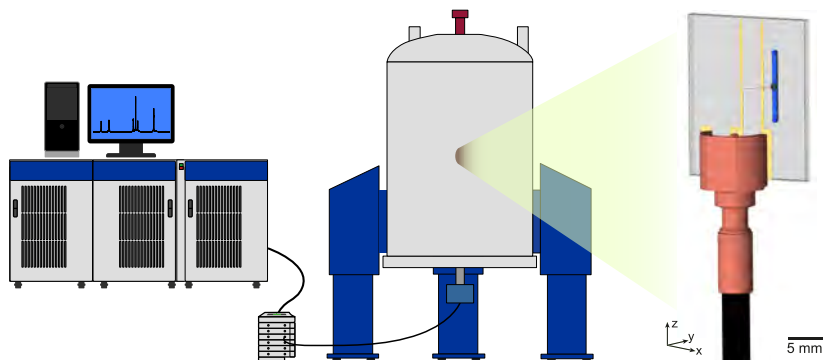
As reviewed in Chapter 2, miniaturisation facilitated realisation of distributed impedance needed for transmission line and non-tuned coils [137, 138, 141–143]. In the transmission line micro-coils the distributed impedance results in a better field homogeneity comparing to the delay lines, as well as a superior power transfer efficiency.

The non-tuned coil introduced by Fratila *et al.* [141, 142] traded tuning/matching for wider bandwidth. In addition, the challenges associated with the extra circuit elements were eliminated. Nevertheless, this class of micro-coils are still under development and their performance can be further improved by either optimising their geometry or modifying the other signal processing elements based on these coils characteristics. In order to do that and as the first step this chapter studies the working principle of these coils.

### 4.2.1 Experimental set-up

As illustrated in Figure 4.2, the experiment is performed using an 11.74 T superconducting magnet, corresponding to the following Larmor frequencies for different nuclei:  $^1\text{H}$ -500 MHz,  $^{19}\text{F}$ - 471 MHz,  $^{31}\text{P}$ - 202 MHz,  $^7\text{Li}$ -194 MHz,  $^{11}\text{B}$ - 160 MHz,  $^{23}\text{Na}$ - 132 MHz,  $^{13}\text{C}$ - 126 MHz. The detector is a hybrid micro-electro-mechanical system (MEMS), consisting of a broadband spiral coil and a microfluidic channel which carries the sample. The detector is installed on top of a probe and is connected to the pre-amplifier block (also known as the low noise amplifier-LNA) using a coaxial cable in order to bypass all the circuits

embedded in the probe. Further details of the measurement setup are discussed in Section 4.5.3.



**Figure 4.2:** The experimental set-up consisting of a superconducting magnet, probe, LNA block, and NMR console. The detector is located on top of the probe inside the magnet. The detector consists of a spiral coil, a microfluidic channel, and an MMBX plug.

### 4.3 Theory

The performance of the broadband coil was considered in both excitation and detection modes. Although all four figures of merit (discussed in Section 2.3) have been studied here, one should note that  $B_1$  homogeneity of the coil and the spectral resolution are independent of the coil tuning and matching. Therefore, the evaluation and optimisation were made based on the excitation efficiency and relative signal-to-noise ratio (SNR). These figures of merit were first redefined considering the effect of tuning and/or matching. As a reference for comparison, a tuned/matched coil was also studied theoretically. Based on these evaluations the optimum geometry was selected. As a complementary study, the performance of the optimum detector was studied in terms of spectral resolution in order to select the best geometry for the microfluidic channel.

### 4.3.1 Figures of merit

#### Excitation efficiency

In order to calculate the excitation efficiency, the sample was assumed to be uniformly distributed within the predefined region of interest. Considering Equation 2.10, the coil current ( $I_{\text{coil}}$ ) for a certain applied power ( $P_{\text{amplifier}}$ ) strongly depends on the tuning/matching conditions. The other parameters are independent of the intermediate circuits between the coil and the excitation power source.

For a broadband case where a coaxial cable connects the coil and the amplifier directly,  $I_{\text{coil}}$  can be calculated as a function of the coil impedance- $Z_{\text{coil}}$ , cable length- $l_{\text{cable}}$ , characteristic impedance of the cable- $Z_{\text{cable}}$ , output impedance of the amplifier- $Z_0$ , and the propagation constant- $\Gamma$ . Assuming  $Z_{\text{cable}} = Z_0$ , the formula for the coil current can be written as:

$$i_{\text{coil,BB}} = \frac{v_{\text{amplifier}} \times e^{-\Gamma l_{\text{cable}}}}{Z_0 + Z_{\text{coil}}} \quad (4.1)$$

whereas in the tuned/matched coil, assuming all the power being dissipated in the coil and not in the tuning/matching circuit, the current can be calculated as:

$$i_{\text{coil,TM}} = \sqrt{\frac{|v_{\text{amplifier}} \times e^{-\Gamma l_{\text{cable}}}|^2}{Z_0 \times r_{\text{coil}}}} \quad (4.2)$$

Therefore, the excitation efficiency ( $ef$ ) for two different cases can be defined considering the newly defined formula for the coil current. In the other words, in the excitation mode, the impedance of the coil and the generated field per unit applied current are the main parameters to be optimised at the desired frequencies. Increasing the number of turns in a spiral coil increases the magnitude of the magnetic field which it generates, but also increases the coil impedance. This trade-off should be analysed at different frequencies and for different matching configurations.

## B<sub>1</sub> uniformity

The distribution of B<sub>1</sub> field, generated by a coil for a unit applied current, depends on the coil geometry, as well as the sample volume geometry. For the frequencies much lower than the self-resonance frequency of the spiral coil, the magnetic field generated at the coil axis can be derived from the Biot-Savart formula as:

$$B_{1,u}(z_o) = \frac{\mu}{2(w+s)} \left[ \frac{r_{in}}{\sqrt{z_o^2 + r_{in}^2}} - \frac{r_{in} + (w+s)n}{\sqrt{z_o^2 + [r_{in} + (w+s)n]^2}} + \ln \left( \frac{r_{in} + (w+s)n + \sqrt{z_o^2 + [r_{in} + (w+s)n]^2}}{r_{in} + \sqrt{z_o^2 + r_{in}^2}} \right) \right] \quad (4.3)$$

where  $z_o$  is the distance of the observation point from the coil which has been assumed much bigger than the track thickness ( $t$ ).  $\mu$  is the magnetic permeability of the sample, and  $w$  and  $s$  are the width of the tracks and the spacing between the tracks, respectively. In this study, these values were considered constant all over the coil geometry.  $r_{in}$  and  $n$  are the inner radius of the coil and its number of turns.

At higher frequencies, the inter-turn parasitic capacitances create alternative current paths rather than the inductive loops, hence forming internal resonators. Therefore, the total magnetic field generated by a unit current flowing through the coil increases with the frequency. At frequencies between the first and second self-resonance frequencies of the coil, the capacitive paths bypass the inductive paths. Therefore, the magnetic field at the sample region decays. Increasing the number of turns improves the magnetic field per unit current, enhances homogeneity of the field, and reduces the self-resonance frequency.

## Relative SNR

Equation 2.10 determines the intrinsic signal amplitude, collected by the coil. However, a resonating circuit can scale-up the induced voltage by conserving the power of the signal but increasing the impedance of the circuit. This can be achieved by adding a capacitor in parallel to the coil. This passive amplification scales both the signal and the noise collected by the coil. Since the capacitors usually have much higher quality factor than the coil, the extra noise and the power dissipation introduced by that can be neglected. Therefore, the SNR remains intact although the signal is amplified.

In order to minimise the SNR degradation by the signal processing chain, the collected signal is further amplified by a low noise amplifier (LNA). A coaxial cable bridges the gap between the coil and its accompanying circuit and the LNA which usually has an input impedance of  $50\ \Omega$ . Nevertheless, the input impedance of the LNA should complex conjugate the output impedance of the coil circuit to achieve the best signal transfer efficiency. This can be achieved with the aid of a second capacitor on the coil side. By adding the second capacitor and adjusting the resonance frequency, the impedance matching can be achieved at a certain frequency. Therefore, the circuit bandwidth is limited to a narrow band around that specific frequency and modification of the detection frequency requires a different combination of capacitors.

Once the signal reaches the LNA, it amplifies the input signal. During this process amplifier also introduces an additional noise . Noise performance of the LNA is determined by the noise-factor ( $F$ ) of the amplifier as a two-port circuit being defined as:

$$F = \frac{SNR_{in}}{SNR_{out}} \quad (4.4)$$

Assuming that the gain of the LNA is adjusted so that the signal level at the output of the LNA is the same in both tuned/matched and broadband case and all the other signal processing steps are the same, the additional distortions are



similar in both cases. Therefore, the SNR of the system at the output of the LNA is a good indicator for the performance of the system in the receive mode. For a tuned and matched coil, the transferred voltage to the input of the amplifier can be calculated as

$$V_{L, TM} = \sqrt{\left| \frac{Z_0}{Z_{coil}} \right|} \times \xi e^{-\Gamma l_{cable}} \quad (4.5)$$

whereas for a broadband coil, where there is no intermediate circuit to adjust the impedance of the coil, and neglecting the power loss as the result of the cable and the connector, the transferred voltage is

$$V_{L, NM} = \frac{Z_0}{Z_0 + Z_{coil}} \times \xi e^{-\Gamma l_{cable}} \quad (4.6)$$

For the micro-coils, the thermal noise of the coil ( $n_{coil}$ ) is dominant and the noise, originating from the sample, is negligible. As discussed earlier, the noise also experiences the same transfer function once travelling through different stages as long as the noise introduced by the cable and other passive elements are negligible. Consequently, SNR at the input of the LNA is the same as the SNR at the coil port. Therefore, the SNR at the output of the LNA for a tuned/matched case is

$$SNR = \frac{\xi}{\sqrt{F} \times n_{coil}} \quad (4.7)$$

whereas for a non-tuned, non-matched coil and modelling the noise performance of the amplifier with a voltage source, the SNR is

$$SNR = \frac{\xi}{\sqrt{n_{coil}^2 + n_0^2 \times \frac{F-1}{2} \times \left| 1 + \frac{Z_{coil}}{Z_0} \right|^2}} \quad (4.8)$$

As the result, the impedance of the coil and the magnetic field, it generates for a unit applied current, are the main parameters in the coil design from the detection perspective.

## Spectral resolution

The spectral resolution of an NMR signal depends on the relative  $B_0$  and  $B_1$  distributions at the sample region and therefore is independent of tuning/matching conditions. The main source of  $B_0$  distortions is the susceptibility mismatch between the sample and its surrounding environment, e.g., the coil, the sample holder, and air. In order to enhance the SNR and the excitation efficiency,  $B_1$  shall be maximised at the sample region and according to Equation 4.3, it mandates the coil to be as close as possible to the sample. Nonetheless, the susceptibility mismatch between the coil and the sample can be minimised by keeping them apart. As a result, there is a trade-off between the spectral resolution and SNR and/or excitation efficiency. In other words, the integral of the signal in the frequency domain depends on the sample and the average  $B_1$  whereas broadening of the signal depends on the susceptibility mismatches. To meet both these requirements, the distance between the coils and sample volume shall be selected mindfully. Other approaches which have not been considered here are either to encapsulate the coil with a material having the same susceptibility as the coil material or to select zero susceptibility material for the coil.

### 4.3.2 Pre-adjustments

#### Detector geometry selection

A spiral coil, patterned on a glass substrate, was selected for this study. The sample was considered as a cylinder with 500  $\mu\text{m}$  diameter and 500  $\mu\text{m}$  height, placed at the backside of the substrate. The coil material is gold. Based on the  $B_{1,u}$  given in Equation 4.3, the optimum value for  $s + w$  is 40  $\mu\text{m}$ . As a rule of thumb, the thickness of the tracks and their width should be at least twice the skin depth to use the track cross-section efficiently. Assuming the minimum working frequency of 100 MHz, its corresponding skin depth is 7.5  $\mu\text{m}$ . As a result, the track thickness, the track width, and the spacing between tracks are set to 20  $\mu\text{m}$ . In addition, the inner diameter of the coil is set half of the sample

diameter to have a good compromise between the field homogeneity and the signal amplitude.

A pad is required at the inner end of the spiral to connect it to its corresponding signal pad. This connection is provided using a wirebond. For a wire diameter of 25  $\mu\text{m}$ , the minimum required pad diameter is 50  $\mu\text{m}$ . In order to maintain the symmetry for both  $B_0$  and  $B_1$  fields, the pad is placed at the centre of the coil. Accordingly, the presence of the pad sets a boundary condition for  $B_1$  field at the axis of the coil and forces it to zero at the location of the pad. The field at the axis increases to a maximum amplitude and then decays exponentially as presented in Figure 4.3. Based on these results, the spacing between the sample and the coil, i.e. the substrate thickness, is set to 100  $\mu\text{m}$  to coincide with the maximum field amplitude. The only unknown is the number of turns. For this purpose, the coil performance was simulated with sweeping the number of turns to evaluate the figures of merit.

### Simulation frequency selection

Considering the distribution of the Larmor frequencies of the NMR active isotopes presented in Figure 2.1, there are three frequency bands where the most interesting nuclei (red dots) are concentrated.  $^1\text{H}$  and  $^{19}\text{F}$  form the high-frequency range,  $^7\text{Li}$  and  $^{31}\text{P}$  form the middle-frequency range, and  $^{15}\text{N}$ ,  $^{17}\text{O}$ ,  $^2\text{H}$ ,  $^{13}\text{C}$ ,  $^{23}\text{Na}$ ,  $^{11}\text{B}$  form the low-frequency range. In order to reduce the computation cost, one frequency was selected as the representative frequency for each range. Taking the 11.74 T magnetic field, 500 MHz was selected as the representative for the high-frequency range whereas 200 MHz was selected as the representative for the middle-frequency range. Since the field and impedance do not experience a considerable change at lower frequencies, 150 MHz can be a good representative for this range although it is not located at its centre.

## Simulation preferences and settings

**RF simulations:** Simulations for the RF studies were performed using *Electromagnetic Waves, Frequency Domain* interface of *RF module* of COMSOL MultiPhysics® 5.5 (COMSOL AB, Sweden). The maximum tolerable relative error for the RF simulations was set to 0.01%. The simulation frequency was swept in a range of 100–1000 MHz. However, the performance was just considered at the three representative frequencies (150 MHz, 200 MHz, and 500 MHz). Simulations were achieved applying 1 A current to the coil terminals.

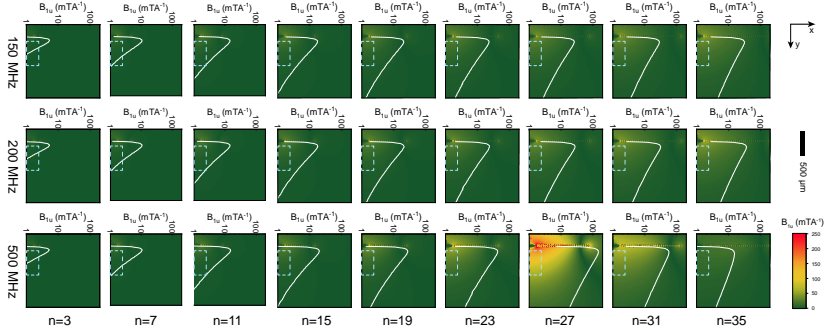
**Susceptibility simulations:** FEM simulations for the susceptibility studies were performed using *Magnetic Fields, No Currents* (MFNC) interface of *AC/DC module* of COMSOL MultiPhysics® 5.5 (COMSOL AB, Sweden). In these simulations, the maximum tolerable relative error was set to 0.1 ppb in order to obtain enough accuracy required for the spectral resolution. The permeability values of different materials were adopted from Schenck [189] and Wapler *et al.* [198] as listed in Section A1.

### 4.3.3 Coil geometry optimisation

#### RF simulations

For the given geometrical parameters, the number of turns was swept in the RF simulations to calculate the impedance of the coil, as well as the magnetic field per unit applied current. As mentioned in the previous sub-sections, the NMR figures of merit depend on these parameters in the coil design level. The field patterns at different frequencies and for different numbers of turns are plotted in Figure 4.3. Since the geometry is symmetric, the field patterns are shown just in half-space. For this purpose, the components of the field being perpendicular to  $B_0$  are considered (components in  $xy$ -plane). The dashed rectangle shows the cross-section of the sample volume. The upper  $x$ -axis together with the line plot illustrates the field at the axis of the coil. The field

amplitude reaches its maximum at  $100\ \mu\text{m}$  distance from the coil and then it drops, almost exponentially, with distance from the coil.



**Figure 4.3:**  $B_1$  field distribution of the coils with different numbers of turns and at three different frequencies. Dashed rectangles highlight the sample volume. The colour maps show the field distribution at the cross-section and the line plots depict the field at the axis of the coils.

As expected, the field homogeneity at the sample volume increases with the number of turns whereas the field amplitude shows a maximum at a certain combination of the frequency and the number of turns ( $f = 500\ \text{MHz}$  and  $n = 27$ ) because of the self-resonance of the coil. After the self-resonance frequency, the field amplitude reduces indicating that the capacitive paths bypass the current of the inductive paths.

Figure 4.4 presents the resistance, inductance, and the quality factor of the coil at different frequencies and for different numbers of turns. The self-resonance effect can be observed at 500 MHz and for the 27 turn coil. Both resistance and inductance increase monotonically with the number of turns for cases lower than the self-resonance frequency. As a result, the quality-factor increases with frequency, as depicted in Figure 4.4.c. At 500 MHz, the maximum quality-factor corresponds to the 17 turn coil.

The analytical prediction for the resistance and the inductance are achieved considering just the coil and excluding all the connection tracks and pads. The

resistance at the radio frequencies was calculated by considering the skin depth to include the effective cross-section of the tracks as:

$$R_{RF} = \rho \frac{l}{A} = \rho \frac{2\pi \times r_{in} \times n + (s+w) \times \pi \times n^2}{(w+t) \times \delta - \delta^2} \quad (4.9)$$

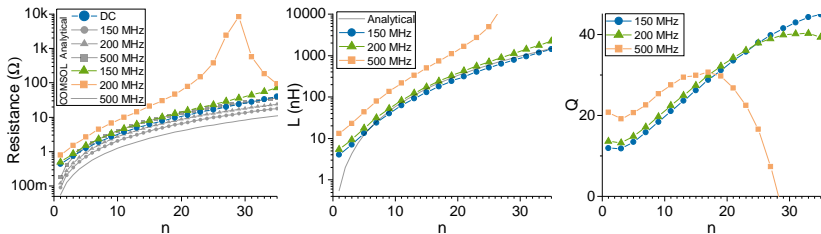
where  $\delta$  is the skin depth. The small difference between the simulation results and the analytical results is because of the extra length of the tracks which connect the coil to its corresponding pads and also the effect of the self-resonance. The inductance can be calculated based on the formula given by Wheeler [212] as:

$$L = 31.33 \times \mu \times n^2 \frac{(r_{in} + (2n-1) \times (w+s)/4)^2}{8 \times r_{in} + 7.5 \times (2n-1) \times (w+s)} \quad (4.10)$$

whereas  $\mu$  is the magnetic permeability of the sample. The values are in good agreement for the number of turns larger than 5. As expected, the error is more pronounced for small numbers of turns since the track impedance is comparable to the coil impedance.

### Post-processing simulation data

The simulation results were further processed in MATLAB® R2018a (Mathworks Inc., USA), to extract the figures of merit. The nutation signal was



**Figure 4.4:** The electrical characteristics of the broadband coil at different frequencies and for different numbers of turns. The values are achieved using COMSOL simulations, as well as the analytical formula.

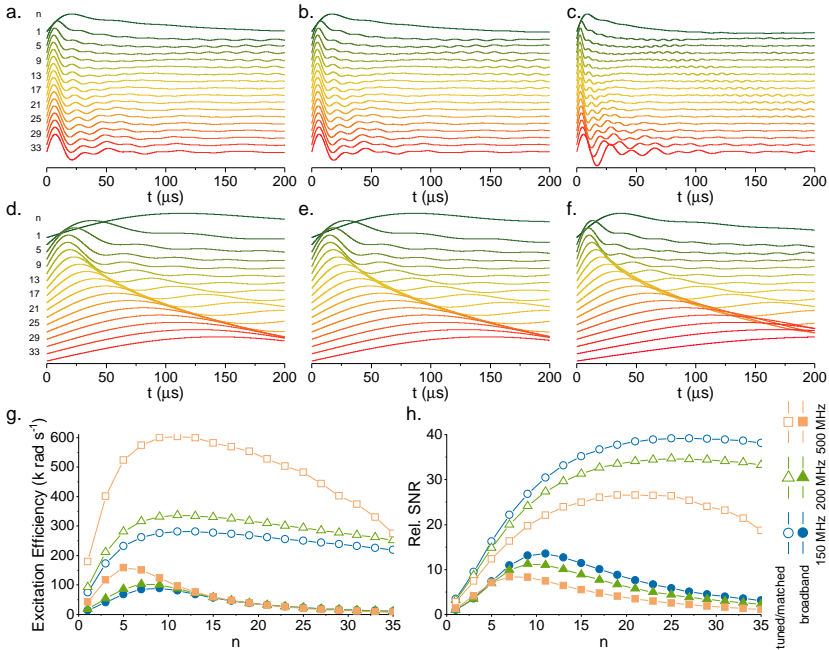
generated by calculating the current flowing in the coil for a unit power provided by the amplifier. For this purpose, the current was calculated based on the Equation 4.2 and Equation 4.1. The flip angle of each elementary voxel (a cube of  $10\ \mu\text{m}$ ) was calculated. The signal from each voxel was collected and superimposed according to the principle of reciprocity. In this process,  $B_0$  was assumed to be perfectly homogeneous. For each combination of the simulation frequency and number of turns, a nutation signal was calculated. These signals are depicted in Figure 4.5. It should be noted again that the tuning and matching affect the frequency of the nutation signal but the relative values of the peaks are independent of the tuning and matching conditions. For the sake of simplicity and ease of comparison, all the nutation signals were normalised with respect to their maximum amplitude. The nutation signals prove that the field homogeneity at the sample region increases with the number of turns.

The excitation efficiency was extracted based on the calculated nutation signals. Besides, SNR was also achieved using the signal amplitude at the  $90^\circ$  pulse. The relative SNR was calculated at the output of the LNA. Therefore, the noise factors of the LNAs have been taken into the account. These values were set according to the data given in Section 4.5.3.

Based on the excitation efficiency results for the tuned/matched case, the best number of turns is about 11-12. According to these data, the coil has the best excitation efficiency at 500 MHz. In addition, the self-resonance caused a faster decay of excitation efficiency at 500 MHz and for  $n \geq 27$  turn.

For the broadband case, the best number of turns is around 5 turns at 500 MHz, 7 turns at 200 MHz, and 9 turns at 150 MHz. The lower excitation efficiency in the broadband case can be compensated either by applying higher power levels for a certain excitation pulse or by increasing the duration of the excitation pulse for a certain power level.

The optimum numbers of turns, corresponding to different combinations of the tuning/matching conditions and frequencies, for SNR are larger in comparison to the excitation efficiency. It is attributed to the additional noise introduced by



**Figure 4.5:** Extracting the figures of merit of the NMR coil based on the simulation results. The nutation signals for a tuned/matched coil (a-c) and a broadband coil (d-f) with different numbers of turns and at different frequencies. The excitation efficiency of the coils with different numbers of turns and at different tuning/matching conditions and different frequencies can be extracted from the nutation signals (g). Relative SNR of the collected signal at the output of the LNA blocks can also be calculated based on the maximum signal amplitude of the nutation spectra for different numbers of turns, at different tuning/matching conditions, and at different frequencies (h).

the LNA. For the tuned/matched case, the best number of turns for the low- and mid-frequencies is 25 turns whereas it drops to 19 turns at 500 MHz.

For both SNR and excitation efficiency, the best values for the number of turns in the case of the broadband detector are less than the tuned/matched case. Accordingly, the best numbers of turns for a broadband detector and from the SNR point-of-view are 11, 9, 7, respectively for 150 MHz, 200 MHz, and 500 MHz. In order to compensate for the lower SNR values, either a higher number of averages or a higher sample concentration is required. However, this



**Table 4.1:** The numbers of turns for the best performance in both tuned/matched and broadband and at different frequencies. Comparing the figures of merit for optimised geometries highlights the total cost to be paid when selecting an optimum number of turn. Additionally, the relative performance of the optimised broadband coil in comparison with its optimised tuned/matched coil can be understood from these figures of merits.

	f (MHz)	excitation eff. (krads <sup>-1</sup> )			rel. SNR			$n_{\text{opt}}$
		$n_{\text{best}}$	best	opt.	$n_{\text{best}}$	best	opt.	
TM	150	12	282	274	25	38.9	36.7	17
	200	11	337	325	25	34.7	32.6	
	500	11	604	569	19	26.7	26.0	
BB	150	9	89	87	11	13.5	12.0	8
	200	7	103	102	9	11.2	10.6	
	500	5	159	137	7	8.4	8.3	

comparison holds for a single nucleus detection and for a fair comparison, a multi-nuclear detector with all its accompanying circuits should be taken into the account.

The best performance results for different combinations of tuning/matching conditions, working frequencies, and figures of merit are summarised in Table 4.1. In order to develop and fabricate a single coil, being optimised for all the frequency range, the optimum number of turns of 8 was selected for the broadband coil and 17 is selected for the tuned/matched coil. These values are achieved by averaging the six corresponding best values in each configuration. The comparison amongst each configuration shows the price to be paid in order to select a single-coil to work at all frequencies. Comparing the relative values shows that the excitation efficiency in the broadband case is 33 %, 31 %, and 22 % of the tuned/matched counterparts at 150 MHz, 200 MHz, and 500 MHz, respectively. The relative SNR at 150 MHz for the broadband case is 36 % of that of the tuned/matched case. Similarly, those values for 200 MHz and 500 MHz are respectively 34 % and 26 %.

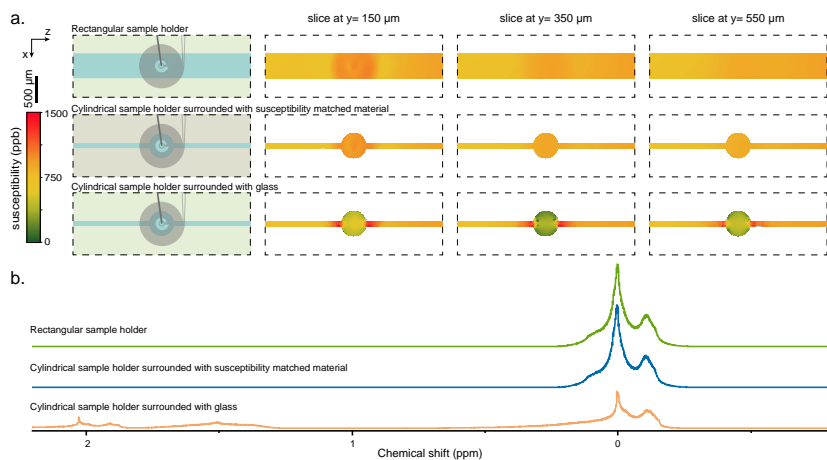
### 4.3.4 Microfluidics channel design

#### Susceptibility simulations

The microfluidic channel geometry and its surrounding material were studied to optimise the spectral resolution of the detector. In order to minimise the dead sample volume, i.e. the sample volume which does not contribute to the signal, a channel of 100  $\mu\text{m}$  width and 500  $\mu\text{m}$  height was assumed. The length of the channel was set to 8 mm so that the inlet and outlet are far enough from the coil and sealing does not conflict with the coil. In this case, the channel and sample volume were presumed to be patterned through a glass layer as shown in Figure 4.6.a. The susceptibility mismatch between the glass and sample (water in these simulations) perturbs  $B_0$  field substantially as shown in Figure 4.6.a. In order to eliminate  $B_0$  perturbations, one solution is to use a susceptibility matched material for the surrounding structures of the channel and the sample volume. A hypothetical material, having the same susceptibility as water and the same dielectric constant as the glass, was assigned to the surrounding material. The simulation results, presented in Figure 4.6.a, confirm the enhancement of  $B_0$  field homogeneity. Nonetheless, there are still some distortions caused by the coil. As the third option and a more practical solution, the channel width was extended to equal the sample holder diameter and glass was used as the surrounding material. With that, the material interface along  $B_0$  is eliminated. Accordingly, the field homogeneity is comparable to the susceptibility matched case. The penalty for that is a higher dead sample volume.

#### Post-processing simulation data

Since  $B_1$  field strength is not uniform all over the sample geometry, a simple  $B_0$  map cannot reveal the exact effect of the distortions on the NMR signal. Therefore, the field maps collected from the susceptibility simulations and the results of the RF simulations using the optimum coil geometry were processed together as discussed in Section 4.3.3 to generate NMR spectra. In these spectra, the line-broadening caused by  $T_2$  relaxation was ignored. The results



**Figure 4.6:** a. The susceptibility simulations at different distances from the coil reveals the effect of the coil and the surrounding environment of the sample on  $B_0$  distribution at the sample. b. NMR spectra corresponding to the different sample volumes and channel geometries.


for different sample geometries are demonstrated in Figure 4.6.b. The relative position of the signal in the chemical shift axis is adjusted manually so that the highest peaks appear at 0 ppm.



The spectrum collected from the cylindrical sample holder without susceptibility compensation consists of a pair of main peaks and multiple shorter peaks whereas those shorter peaks are absent in both susceptibility matched case and rectangular sample holder. Those peaks are attributed to the effect of the glass material surrounding the sample. The split in the main peak corresponds to the presence of the coil. The susceptibility mismatch between the sample and the coil decays with distance from the coil and so does  $B_1$  amplitude. Therefore, the higher peak located at the higher chemical shifts corresponds to the sample close to the coil whereas the second peak corresponds to the sample at the other end of the sample volume.

The detector geometry optimisation was started with optimising the coil geometry, assuming a perfectly homogeneous  $B_0$  field to calculate the total signal

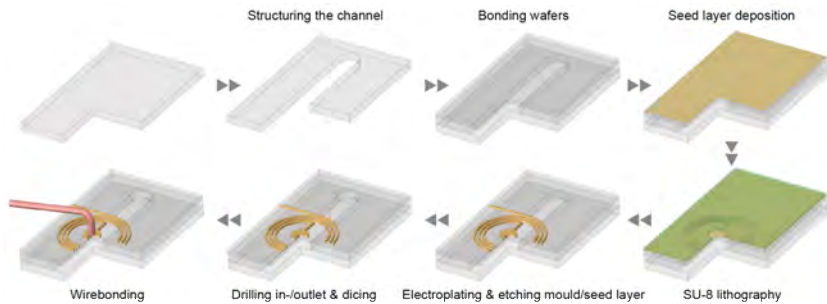
which can be collected from a sample. However, the inhomogeneity of  $B_0$  increases the broadening of the signal and reduces the height of the peaks, hence SNR. As a rule of thumb, the main factor affecting field homogeneity is the susceptibility mismatches whose projection along  $B_0$  field coincide with the sample, being in the field of view of the coil. Nevertheless, the material interfaces in the neighbourhood of the sample volume cause some distortions, too. The sample geometry and its surrounding were optimised in the next step based on  $B_0$  simulations and for the optimised coil geometry. The optimised detector design was concluded according to these results. This design can be found in Section A3.

## 4.4 Fabrication

The detector consists of three glass layers bonded together. The top layer, being 100  $\mu\text{m}$  thick, serves as the substrate for the metallic structures and acts as a spacer between the coil and the sample volume. Besides, the inlet and outlet of the microfluidic channel are drilled in this layer. The second layer is 500  $\mu\text{m}$  thick and is structured for the microfluidic channel. The third layer is 500  $\mu\text{m}$  thick and seals the channel. The lithography masks (designed using LayoutEditor® and printed on transparent foils with 12  $\mu\text{m}$  resolution) and CAD files were designed based on the optimum geometry. Further details of the fabrication steps, marked with , are given in Section A2.

As illustrated in Figure 4.7, the fabrication process starts with structuring the channels and alignment marks in a 4 inch, 500  $\mu\text{m}$ -thick D 263® T eco wafer using nanosecond Laser (PIRANHA® ACSYS). In the next step, the wafer was rinsed with isopropanol (IPA) and Acetone followed by plasma cleaning<sup></sup> (RIE plasma etcher Etchlab 200, SENTECH Instruments GmbH) for 30 min to remove all the residues. The dehydration bake step was performed on a hotplate at 200 °C for 5 min. A 4 inch, 100  $\mu\text{m}$ -thick D 263® T eco wafer was then rinsed with IPA and Acetone and cleaned with  $\text{O}_2$ -plasma<sup></sup> (RIE plasma etcher Etchlab 200, SENTECH Instruments GmbH) for 10 min followed by dehydration on a

hotplate at 200 °C for 5 min. These two wafers were bonded together employing an SU-8 layer. For this purpose, 5  $\mu\text{m}$  SU-8 3005 was coated<sup>[2]</sup> on the thin wafer and was partially baked<sup>[2]</sup>. As mentioned in Section 3.4, the partial bake maintains a reliable adhesion, as well as, uniformity of the photoresist. The coated side of the thin wafer was brought into contact with the top side of the structured wafer and they were bonded using compression bonding<sup>[2]</sup> (EVG 510®, EV Groups). After bonding, the assembly was exposed with 300  $\text{mJ cm}^{-2}$  using the mask aligner (EVG 620®, EV Groups) and baked on the hotplate at 90 °C for 240 min. The third wafer (4 inch, 500  $\mu\text{m}$ -thick D 263® T eco) was similarly cleaned and bonded to the backside of the assembly.



**Figure 4.7:** The fabrication process starts with structuring the channels in the middle wafer and bonding it to the top and bottom wafers. In the next step, the coil was patterned on the top side of the assembly using lithography and electroplating processes. The in-/outlets were patterned with a nanosecond laser followed by dicing the assembly into the individual chips. The wirebonding step connects the middle pad of the coil to its corresponding pad. As the last step, the MMBX connector is soldered to the chip.

The assembly was cleaned following by dehydration bake at 120 °C for 20 min. The seed layer was deposited on top of the assembly employing physical vapour deposition (PVD) technique for the target thickness of 20 nm and 60 nm for Cr and Au, respectively. The assembly was cleaned similar to the previous steps and was coated<sup>[2]</sup> with a layer of 25  $\mu\text{m}$  SU-8 3025. Softbake was performed at 90 °C for 15 min. The assembly was then exposed through a mask with an exposure dose of 330  $\text{mJ cm}^{-2}$  followed by the post-exposure bake for 4 min

at 90 °C. The structures were developed using PGMEA for 20 min and rinsed with IPA and DI-water. The final structures went through a dehydration step for 360 min at 30 °C inside a convection oven.

Electroplating the metallic objects was performed using pulsed gold electroplating<sup>□</sup> for the target height of 20 µm. The photoresist was etched physically using O<sub>2</sub>-Plasma<sup>□</sup> for 40 min and the seed layers were etched chemically. After cleaning and dehydration at 120 °C for 20 min, the inlet/outlet holes were structured on the top layer and the assembly was diced into individual chips using the nanosecond laser. The centre pad of the coil was connected to its corresponding track with a ball-wedge wirebond using an automated wirebonder (3100® ESEC, Switzerland). In the last step, an MMBX connector (HUBER + SUHNER, Switzerland) was soldered to the chip to provide access for the coaxial cable and the chip was mounted on the PMMA adaptor.

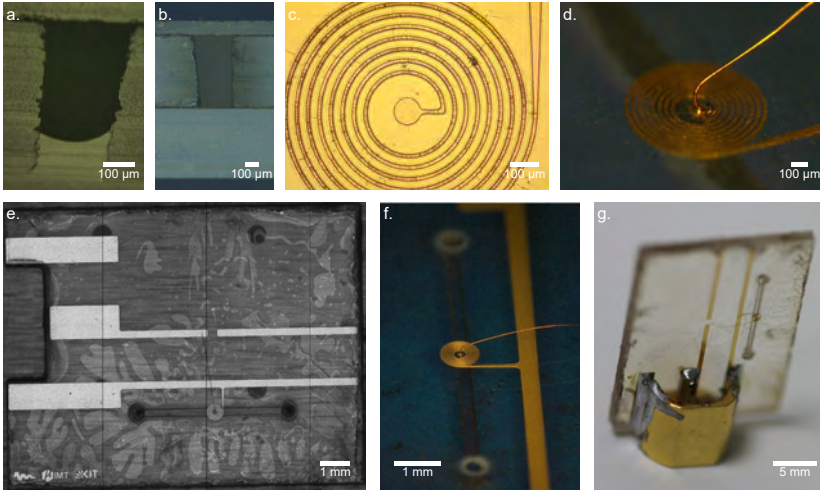
## Fabrication challenges

**Bonding:** Bonding the wafers using SU-8 as the adhesive material happens at the beginning of the fabrication process for two reasons: i) maintaining alignment of the structures on two different wafers was not possible with the current cleanroom equipment; ii) the force needed for the bonding could damage the structures (metallic structures or photoresist) on top of the assembly. Therefore, the bond should either withstand all the successive chemical and heat treatments during the fabrication process, or the process should be modified accordingly. It is especially important because of the different thermal behaviour of the SU-8 and D 263® T eco wafers. Therefore, all the successive heating treatment steps were limited to 120 °C. Applying higher pressure or temperature during the wafer-bonding process enhances the bond quality and stability. Nevertheless, it increases the reflow probability of the SU-8 which can flood the microfluidic channel and clog it (see Figure 4.8.a and .b). Therefore, the temperature was fixed at the glass-transition temperature of the non-cured

SU-8 and force was modified in order to achieve the best bond quality. The optimum parameters also strongly depend on the storage condition of SU-8 and its quality. Therefore, the optimisation process was repeated for each fabrication batch.

**Developing fine structures of the SU-8 mould:** A major bottleneck in the lithography process, to define the mould for the electroplating, is the reflection of the UV-light from the gold seed layer. It is especially challenging for the foil masks and objects with aspect ratio bigger than or equal to one. As a result, the edges of the mould are not sharp and residues of photoresist remain on the surface (see Figure 4.8.c). As discussed in Section 3.4, one method to eliminate the artefacts is to use anti-reflection coatings, e.g. AZ® BARLi® II (MicroChemicals, Germany), on top of the seed layer. However, AZ® BARLi® II requires a baking temperature of 200 °C which is not compatible with the adhesion layer. Therefore, the exposure dose was reduced in the lithography process to avoid under-exposure phenomena. Moreover, the structures were treated with a low-power O<sub>2</sub>-Plasma for few minutes to physically remove the residues. However, this treatment affects the other parts of the mould and makes the openings wider on top.

**Ball-Wedge wire bond on the channel:** Establishing a connection between the inner pad of the coil and its corresponding track using wirebonder was a challenge for three reasons: i) the pad size was made small to reduce its impact on B<sub>1</sub> distribution. As a result, the small pad size does not allow rebound in case of a failure. ii) The channel coincides with the pad location. It reduces the rigidity of the substrate and quality of the ball-bond. iii) SU-8 bonds limit the temperature of the process (it was set to 120 °C in this process). Since the bond is not rigid enough, it partially consumes the ultrasonic energy applied for the bond form which degrades the ball-bond quality. The main stress to the ball bond is during the wire forming. Figure 4.8.d shows a ball-bond with low quality. In order to



**Figure 4.8:** a. A cross-section of the channel reveals that the channel is partially filled with SU-8 during the bonding process. b. Optimisation of the bonding process results in a reliable bonding without flooding the channel. c. The poor resolution of the lithography process leaves photoresist residues. d. An unreliable ball-bond as a result of small pad size and low rigidity of the substrate. e. A photo of the chip after wirebonding. f. The relative position of the channel and the coil. g. The detector after soldering the MMBX connector.

reduce the stress, the speed of the wire forming process was adjusted to 10% of the standard speed.

## 4.5 Characterisation

### 4.5.1 Benchtop measurements

In order to verify the simulations and evaluate the performance of the coils, the impedance of the fabricated structures was measured using a Network Analyser (E5071C, Keysight® Stuttgart, Germany), probe station (MPS150, FormFactor® Thiendorf, Germany), Z-probe (Z0-20-K3N-GS-50, FormFactor® Thiendorf, Germany), and WinCal™ XE software (FormFactor® Thiendorf, Germany). For this purpose, extra test structures were added to the masks and

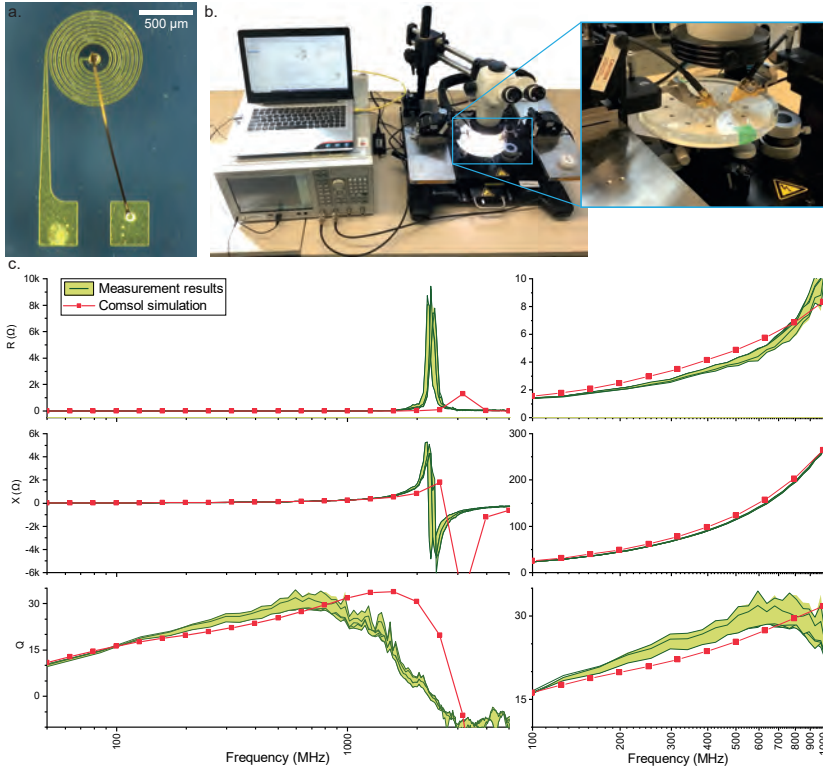


fabricated together with the detectors. These structures consist of a spiral coil with the same parameters as the main coil but the connections and tracks were adjusted to meet the requirements of the measurement setup. A test structure is shown in Figure 4.9.a. The metallic chunk of the impedance analyser was replaced with a PMMA plate in order to eliminate its parasitic effect on the measurements. The setup is depicted in Figure 4.9.b.

A coil similar to the tested structure was also simulated. The simulation and measurement results are presented in Figure 4.9. The simulation predicts a self-resonance frequency  $\sim 3$  GHz whereas the measured value is about  $\sim 2.2$  GHz. In the sub-GHz frequency range, measurement results are in good agreement with the simulations and confirm the accuracy of the simulations. Lower values for the resistance of the structure is attributed to a larger cross-section of the coil tracks, i.e., a thicker electroplated layer or wider openings of the electroplating mould. Similar coil quality-factors in both simulation and measurement confirms this hypothesis.

### 4.5.2 MRI measurements

A series of MRI experiments (FLASH sequence) were performed to evaluate the distribution of  $B_1$  field generated by the coil and verify both simulation and analytical predictions. The experiments were accomplished with an 11.74 T Avance III Bruker NMR system (Bruker BioSpin, Rheinstetten, Germany) and using ParaVision 6.0.1 (Bruker, Germany) on a distilled water sample and at 30 °C. The detector was mounted on top of a home-built probe [213], with the help of a PMMA adaptor. The detector was directly connected to the LNA block through a custom-made coaxial cable (HUBER + SUHNER, Switzerland) to bypass all the circuits embedded in the probe and reduce the signal loss or the additional noise. The cable (G\_02232\_D, HUBER + SUHNER, Switzerland) is 2 m long and terminated to an MMBX plug at one end and an N-type connector at the other end.

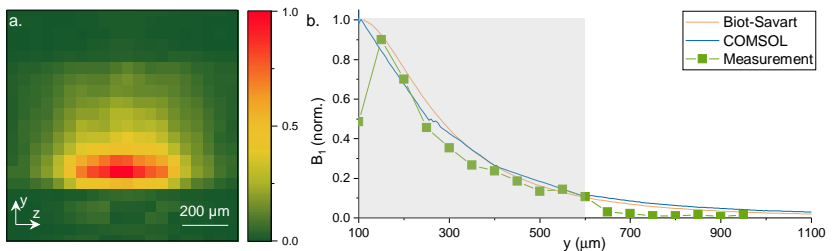


**Figure 4.9:** The impedance of the test structures (a) was measured employing a set-up consists of a Network Analyser, probe station, and Z-probes (b). The measurement results (c) are in good agreement with the simulation results, especially in the sub-GHz range (right hand side plots).

The settings for the sequence are: TR/TE - 1000 ms/4 ms, slice thickness - 100 μm along the nominal y-axis, in-plane resolution -  $32 \times 32$  μm, Tscan - 21 min, FOV  $1.6 \times 1.6$  mm<sup>2</sup>, bandwidth - 5.4 kHz, and 64 averages. The duration of the excitation pulse was fixed at 1.1 ms and the power level was swept from 0.1 mW to 640 mW logarithmically in 80 steps. 1 min delay was set between two consecutive experiments for the spins to fully relax. The results are depicted in Section A6.

The results were collected to form a 3D matrix in which the third dimension was the applied power. The matrix was processed in MATLAB® R2018a (Mathworks Inc., USA) to extract the evolution of the signals for each specific voxel and generate their corresponding nutation signals. Based on the frequency of the nutation signal,  $B_1$  amplitude at each certain voxel was obtained and plotted in Figure 4.10.a.

In order to compare the measurement results, the simulation results, and the analytical formula, they have been plotted together (Figure 4.10.b) at the axis of the coil as a function of distance from the coil. It shall be noticed that the measurement results are just valid for the locations where the sample exists (gray region). Within that range, the results are perfectly matched suggesting that the simulations and analytical formula are accurate. The only difference between the measurements and other data is at  $y = 100 \mu\text{m}$ . This difference is attributed to the boundary voxel being partially filled with the sample in the MRI experiment.



**Figure 4.10:** MRI experiments were performed and processed to evaluate  $B_1$  map (a). Comparison of the measurement results, the simulation results, and the prediction obtained using the analytical formula at the coil axis confirms the accuracy of the simulations (b).

### 4.5.3 NMR measurements

As depicted in Figure 4.2, the sample was loaded in the channel and the detector was mounted on top of the probehead for the NMR experiments. Seven different nuclei were targeted for the NMR measurements based on their receptivity and

the available hardware. For this purpose, two different samples were selected: an aqueous sample and a battery electrolyte sample.

### Sample preparation

**Aqueous sample:** 500 mM phosphate buffer saline (PBS) of pH 5.5 was made with PBS tablets in a mixture of 1.5 mL H<sub>2</sub>O and 1.5 mL D<sub>2</sub>O (99.9 atom % D). 500 mM <sup>13</sup>C labelled D-glucose ( $\geq 99.5\%$ ), 500 mM boric acid (ACS reagent,  $\geq 99.5\%$ ), 500 mM NaH<sub>2</sub>PO<sub>4</sub> (BioReagent, for molecular biology, anhydrous,  $\geq 98\%$  NaH<sub>2</sub>PO<sub>3</sub>), and 250 mM TSP (3-(trimethylsilyl)- propionic-2,2,3,3-d<sub>4</sub> acid sodium salt, 99.9 atom %, contains 0.05 wt. % TSP) were dispersed in the PBS solution. The mixture was stirred until it became highly translucent. This sample was used to detect <sup>1</sup>H, <sup>31</sup>P, <sup>11</sup>B, <sup>23</sup>Na, <sup>13</sup>C.

**Battery electrolyte sample:** 1 M Lithium bis(trifluoromethanesulfonyl)imide (LiTFSI, Tokyo Kasei, Tokyo, Japan) solution was made using 1-ethyl-3-methylimidazolium bis(trifluoromethanesulfonyl)imide (EMI-TFSI) (Tokyo Kasei, Tokyo, Japan) as the solvent. This sample was used to detect <sup>1</sup>H, <sup>19</sup>F, <sup>7</sup>Li.

### Measurement set-up

The NMR experiment setup was similar to the one described in the MRI experiment section. The NMR experiments were performed using TopSpin 3.5 (Bruker, Germany). The applied power was 1 W and the shimming was performed manually on the <sup>1</sup>H spectrum and was kept the same for all the other experiments. For the nutation plots, the data points corresponding to each certain pulse width were integrated and plotted as bar plots to reduce the distortions introduced by relaxation damping or B<sub>0</sub> inhomogeneities.

- **Experiments on the aqueous sample**

- **$^1\text{H}$  experiment at 500 MHz:**

Signal was routed through a narrow-band pre-amplifier (1H LNA MODULE 500, Bruker BioSpin, Rheinstetten, Germany) with 1 dB noise figure. Nutation experiments were performed to calculate the  $90^\circ$  pulse width. The nutation signal consists of 76 single scans with an increment of  $2\ \mu\text{s}$ . The relaxation delay between two consecutive scans was set to 15 s. The NMR spectrum was achieved at  $90^\circ$  pulse width, afterwards. The spectrum consisted of 512 scans each containing 20480 data points within 20 ppm spectral width. The relaxation delay was 10 s and the resulting signal was multiplied with an exponential function equivalent to 0.3 Hz line broadening. Signal was Fourier transformed together with an automatic baseline and phase adjustments.

- **$^{31}\text{P}$  experiment at 202 MHz:**

Signal was directed through a broadband pre-amplifier (XBB19F 2HS MODULE 500, Bruker BioSpin, Rheinstetten, Germany) with 2 dB noise figure. Nutation signal consists of 51 spectra each having 128 scans with an increment of  $2\ \mu\text{s}$ . Between two consecutive scans a relaxation delay of 4 s was applied. The NMR spectrum was collected at  $90^\circ$  pulse width and with 2048 scans. 30720 data points were accumulated at 60 ppm spectral width. The resulting signal was multiplied with an exponential function corresponding to 5 Hz line broadening. The Fourier transform was performed and the baseline and phase were adjusted automatically.

- **$^{11}\text{B}$  experiment at 160 MHz:**

The signal path was defined through the broadband pre-amplifier (XBB19F 2HS MODULE 500, Bruker BioSpin, Rheinstetten, Germany) with 2 dB noise figure. As the signal was very faint, nutation was not possible. Instead, different experiments were performed at

different pulse width with the range of 10  $\mu\text{s}$  and 20  $\mu\text{s}$ . The highest signal amplitude was found to be at 17  $\mu\text{s}$ . Therefore, it was assumed as the 90° pulse width. The final NMR spectrum consisted of 32768 scans. Each scan had 10240 data points with 250 ppm spectral width. The relaxation delay was set to 0.1 s. An exponential function equivalent to 100 Hz line broadening was multiplied to the signal and result was Fourier transformed. The phase of the final signal was adjusted manually and the baseline was set automatically.

### **<sup>23</sup>Na experiment at 132 MHz:**

The signal was routed through the broadband pre-amplifier (XBB19F 2HS MODULE 500, Bruker BioSpin, Rheinstetten, Germany) with 2 dB noise figure. Nutation signal is a collection of 51 spectra each consisting of 128 scans with a pulse width increment of 2  $\mu\text{s}$ . The relaxation delay between two consecutive scan was 5 s. The spectrum was sum of 2048 scans at 90° pulse width. Spectral width was set to 30 ppm having 2048 data points. An exponential signal corresponding to 1 Hz line broadening was multiplied to the time domain signal and then it was Fourier transformed. Automatic baseline and phase adjustments were performed.

### **<sup>13</sup>C experiment at 126 MHz:**

The signal directed through the broadband pre-amplifier (XBB19F 2HS MODULE 500, Bruker BioSpin, Rheinstetten, Germany) with 2 dB noise figure. As the signal was very weak, nutation was not possible. Instead, different experiments were performed at different pulse width within the range of 10  $\mu\text{s}$  and 20  $\mu\text{s}$ . 17  $\mu\text{s}$  pulse width resulted in the highest signal amplitude. Therefore, it was assumed as the 90° pulse width. The NMR spectrum consists of 32768 scans each having 20480 data points and 200 ppm spectral width. The relaxation delay was 0.1 s and the resulting signal was multiplied with an exponential function equivalent to 10 Hz line broadening fol-

lowed by Fourier transform. The baseline and phase were adjusted manually.

- **Experiments on the electrolyte sample**

- **<sup>1</sup>H experiment at 500 MHz:**

Signal was routed through a narrow-band pre-amplifier (1H LNA MODULE 500, Bruker BioSpin, Rheinstetten, Germany) with 1 dB noise figure. Nutation experiments were performed to calculate the 90° pulse width. The nutation signal consists of 76 single scans with an increment of 2 μs. The relaxation delay between two consecutive scans was set to 15 s. The NMR spectrum was achieved at 90° pulse width, afterwards. The spectrum consists of 256 scans each containing 20480 data points within 15 ppm spectral width. The relaxation delay was 10 s and the resulting signal was multiplied with an exponential function equivalent to 0.3 Hz line broadening. Signal was Fourier transformed together with automatic baseline and phase adjustments.

- **<sup>19</sup>F experiment at 471 MHz:**

Signal was directed through a broadband pre-amplifier (XBB19F 2HS MODULE 500, Bruker BioSpin, Rheinstetten, Germany) with 2 dB noise figure. Nutation experiments were performed to calculate the 90° pulse width. The nutation signal consists of 76 spectra each having 4 scans with an increment of 2 μs. The relaxation delay between two consecutive scans was set to 10 s. The NMR spectrum consists of 128 scans at 90° pulse width. 20480 data points were collected for each scan with 20 ppm spectral width and 10 s relaxation delay. The signal was multiplied with an exponential function equivalent to 10 Hz line broadening. The result was Fourier transformed and baseline and phase adjustments were performed automatically.

**<sup>7</sup>Li experiment at 194 MHz:**

Signal path was defined through broadband pre-amplifier (XBB19F 2HS MODULE 500, Bruker BioSpin, Rheinstetten, Germany) with 2 dB noise figure. The nutation signal consisted of 76 spectra. Each spectrum had 64 scans with an increment of 2  $\mu$ s. The relaxation delay between two consecutive scans was set to 1 s. The NMR spectrum consists of 512 scans. 5120 data points were collected for each scan with 20 ppm spectral width. The collected signal was multiplied with an exponential function corresponding to 2 Hz line broadening and it was then Fourier transformed. The baseline and phase were adjusted automatically.

**Results**

**Aqueous sample:** NMR spectra and nutation signals of the sample at different frequencies are plotted in Figure 4.11. The peaks corresponding to <sup>1</sup>H spectrum of TSP, H<sub>2</sub>O, and glucose are distinguishable. The peak splitting predicted by the simulation was fixed by shim compensation. Nevertheless, the peak shape has an asymmetric form similar to the simulated spectrum. SNR of the H<sub>2</sub>O peak was 4295 and the spectral resolution for TSP peak was 8.3 Hz. The spectral resolution enhancement was restricted by gradient current since it reached its maximum value, allowed by the software in one direction. As shown in Figure 4.2, the coil was placed at one side of the chip and about 5 mm away from the isocenter in order to be away from the MMBX connector and avoid susceptibility distortions. As a result, a proper shim cannot be achieved using conventional shim coils. More than 2 $\times$  enhancement in the spectral resolution is anticipated in case of proper shimming. It can be obtained by either releasing the software restrictions for the shims, allocating the coil at the isocenter and pushing the connector towards the edge of the chip, or employing on-chip shim structures. It is worth noting that in general, the broadband coils



have a better spectral resolution, compared to their tuned/matched coils, due to eliminating the capacitors and tank/trap circuits.

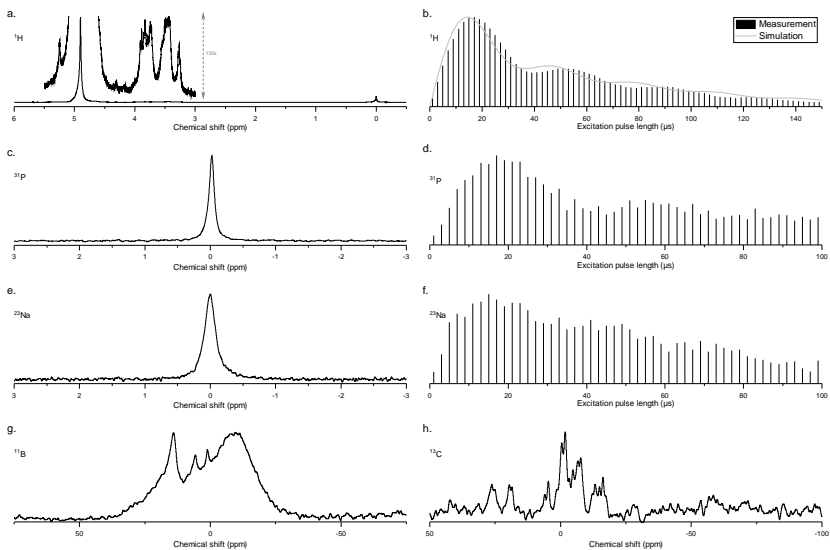
The  $^1\text{H}$  nutation signal is similar to the simulated signal in terms of relative heights of the peaks. The only difference is that the simulated signal is more compressed meaning that the power transfer efficiency in the experiment is  $\sim 15\%$  lower ( $90^\circ$  pulse width of  $17\ \mu\text{s}$  vs.  $14.5\ \mu\text{s}$  for measurements and simulations, respectively). It is attributed to the measurement non-idealities, e.g., power loss in the cable and connectors, the impedance of the amplifier, deviation in the distance between the coil and sample volume because of the adhesion material, which were not considered in the simulations.

$^{31}\text{P}$  spectrum shows a peak corresponding to the PBS. SNR of the collected signal is 112.5.  $^{31}\text{P}$  nutation signal suffers from more distortions because of lower intrinsic SNR. The  $90^\circ$  pulse width extracted from the nutation signal is  $17\ \mu\text{s}$ .

$^{11}\text{B}$  NMR spectrum shows a wide peak corresponding to the boric anhydride  $\text{B}_2\text{O}_3$  content in the substrate. Furthermore, there are three peaks which correspond to the Boric acid. This signal was achieved at a pulse width of  $17\ \mu\text{s}$ . In order to verify the spectrum, a set of experiments were performed on different samples using a commercially available coil. The corresponding results confirm that three peak spectrum is generated by the boric acid chemical reaction with glucose and forming the borate-glucose complex molecule [214, 215] under certain chemical pH environment. Further details can be found in Section A7.

$^{23}\text{Na}$  spectrum reveals a peak corresponding to the  $\text{NaH}_2\text{PO}_4$  with an SNR of 54.  $^{23}\text{Na}$  nutation signal also suffers from low SNR. The  $90^\circ$  pulse width is  $15\ \mu\text{s}$ .

$^{13}\text{C}$  NMR spectrum captures the glucose content with a very low SNR. It is attributed to the low receptivity of the carbon atoms. The excitation



**Figure 4.11:** NMR spectra of the aqueous sample collected from different isotopes at 11.74 T together with their corresponding nutation signals. The simulated nutation spectrum of the  $^1\text{H}$  is also plotted together with the measurement results for an easier comparison.

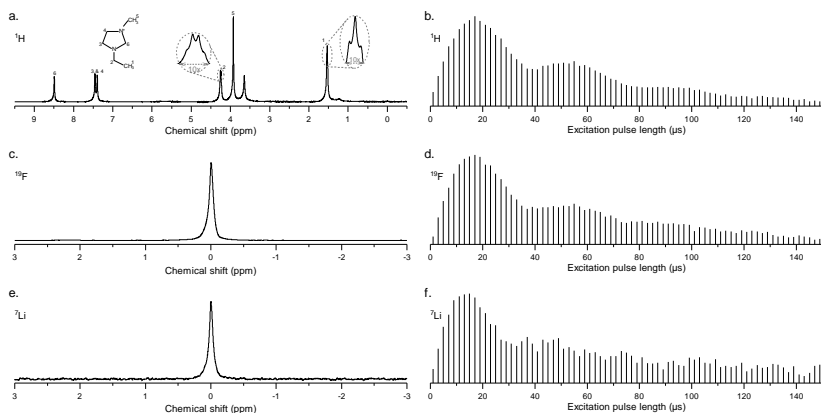
pulse applied for this signal has a width of  $17\ \mu\text{s}$ . The glucose spectrum experiences some changes because of the borate-glucose complex. Section A7 discusses that in more details.

**Battery electrolyte sample:** This sample was evaluated at three different frequencies as depicted in Figure 4.12.  $^1\text{H}$  spectrum reveals the structure of 1-Ethyl-3-methylimidazolium. SNR of the peak at 3.9 ppm (corresponding to  $\text{CH}_3$ ) is 830.5. The nutation signal is similar to  $^1\text{H}$  nutation signal of the aqueous sample which confirms that the power dissipation in the electrolyte sample is negligible. According to this experiment, the pulse width corresponding to the  $90^\circ$  flip angle is  $17\ \mu\text{s}$ . In this spectrum, the triplet signal at  $\sim 1.50 - 1.56$  ppm corresponds to the proton at position 1. The quartet at  $\sim 4.22$  ppm to  $\sim 4.48$  ppm represents carbon 2. The

methyl protons at carbon 5 generate the singlet at  $\sim 3.80$  ppm and the symmetric protons at carbon 3 and 4 form the doublet at the chemical shift from  $\sim 7.40$ – $7.50$  ppm. The singlet signal at  $\sim 8.50$  ppm is assigned to the proton at carbon 6.

$^{19}\text{F}$  spectrum shows a peak corresponding to the fluorine in the Lithium bis(trifluoromethanesulfonyl)imide and bis(trifluoromethanesulfonyl)imide. SNR of the peak is 597.9. Nutation signal at  $^{19}\text{F}$  experiment has the same behaviour as  $^1\text{H}$  nutation signal. The  $90^\circ$  pulse width for  $^{19}\text{F}$  was calculated to be  $17\ \mu\text{s}$ .

$^7\text{Li}$  spectrum shows a peak corresponding to the Lithium content in Lithium bis(trifluoromethanesulfonyl)imide. This peak has an SNR of 82.5.  $^7\text{Li}$  Nutation signal has a lower SNR, compared to other nuclei. Nevertheless, the SNR suffices for  $90^\circ$  calculation ( $90^\circ$  pulse width is  $17\ \mu\text{s}$ ).



**Figure 4.12:** NMR spectra of the battery electrolyte sample collected from different isotopes at 11.74 T together with their corresponding nutation signals.

## 4.6 Discussion and conclusion

Limit of detection (LOD) is a measure to evaluate the detection performance of the micro-coils. This parameter represents the total number of spins required to give an SNR of 3 for total acquisition time of 1 s. Therefore, this parameter is defined as:

$$LOD = \frac{3 \times n \times \sqrt{t_{ef}}}{SNR} \quad (4.11)$$

where  $n$  is the total number of spins contributing to the signal,  $t_{aq}$  is the acquisition time, SNR is the signal to noise ratio for the peaks. In order to exclude the effect of static magnetic field ( $B_0$ ), LOD value is usually converted to a second parameter ( $nLOD = LOD \times (14.0954/B_0)^{7/4}$ ) corresponding to 14.0954 T static field which is taken as the basis for the comparison. The nLOD calculated for different nuclei are given in Table 4.2.

The  $88 \text{ nmols}^{1/2}$  nLOD, calculated for  $^1\text{H}$ , is comparable to the single resonant detectors reported in the literature [13]. The main obstacle to further increase this number is the shimming issue. The linewidth can be easily enhanced to 2 Hz by either applying higher shim current amplitudes or moving the coil and sample to the isocentre of the magnet. With this enhancement, the nLOD can be improved to  $\sim 20 \text{ nmols}^{1/2}$ .

Moreover, this broadband detector holds the record for the total number of observed nuclei without any modification to the hardware. This feature accelerates the multinuclear experiments by saving the time for hardware modifications and shim adjustments.

### 4.6.1 Challenges and suggestions

The main challenge is the low spectral resolution of the detector. Considering the same performance, enhancing the spectral resolution improves SNR considerably.  $B_0$  distortions mainly originate from the coil. By using a material which has a susceptibility closer to the sample, e.g., copper, the resolution improves.

**Table 4.2:** NMR experiment results at seven different frequencies prove the broadband performance of the detector. The nLOD value corresponding to  $^1\text{H}$  is comparable to the state of the art [10, 12, 13].

	aqueous sample					electrolyte sample		
	$^1\text{H}$	$^{31}\text{P}$	$^{11}\text{B}$	$^{23}\text{Na}$	$^{13}\text{C}$	$^1\text{H}$	$^{19}\text{F}$	$^7\text{Li}$
power (W)	1	1	1	1	1	1	1	1
$\pi/2$ pulse ( $\mu\text{s}$ )	17	17	17	15	17	17	17	15
averages (#)	$2^9$	$2^{11}$	$2^{11}$	$2^{15}$	$2^{15}$	$2^8$	$2^7$	$2^9$
SNR	4295	113	-	54	8	831	598	83
nLOD (nmols $^{1/2}$ )	88	135	-	1025	-	-	36	66

The other solution is to encapsulate the coil with a dielectric material having a similar susceptibility. Employing a more advanced material engineering steps, e.g., adding air pockets or additional material to make up for the distortions, is another possibility.

The spectral resolution issue can also be compensated by improving the shim performance. Either employing higher shim currents, relocating the detector and sample volume to the isocentre of the magnet, or adding shim-on-chip structures.

Integration of electronics together with the coil is another feature which has been exploited for the micro-coils [147, 216–218]. As a result, the power transfer efficiency between the coil and electronics can be improved by avoiding long signal paths. Besides, Grisi showed that switching between different frequencies or even sweeping a bandwidth can be performed employing integrated electronics [219]. In case of a broadband coil, the electronics can be modified to improve impedance matching between the coil and electronics and additionally perform multi-dimensional experiments without requiring external filters.



## 5 Broadband NMR stripline, an add-on for standard NMR coils

### 5.1 Overview

Although micro-coils have been widely developed and are gaining more attention, implementing them in an experiment is not straight forward. Therefore, NMR studies on the micro-samples is still a challenge and the field still lacks a "user-friendly" tool which enhances the NMR experiment efficiency for micro-samples and does not require major modification to the standard hardware. Besides, several NMR applications such as thin-films are not compatible with the standard coils and require their own application-specific coils. Experiments which involve metallic structures inside the NMR detection zone, e.g. energy storage devices, pose a different challenge. In this study, we aim for an add-on, which can be employed together with the conventional NMR coil and facilitate a wide range of experiments such as the ones mentioned above. This adaptor exhibits a wideband performance and can be employed in the same way as a standard sample tube.

This chapter starts with reviewing the challenges regarding the handling of micro-coils and micro-samples. Before discussing the add-on, the Lenz lens adaptors are reviewed briefly in order to gain an understanding of the working principle of these add-ons. The discussion continues with studying the additional features of the design which broadens its application to solve the current issues of the NMR hardware, e.g. incompatibility with 2D samples and metallic electrodes. The figures of merit of this detector are considered in the next section followed by performance simulation of the add-on. Based on the simulation results, an

optimised geometry is proposed for a certain sample volume. The fabrication and experimental evaluation of the design are presented followed by a discussion and conclusion.

The concept introduced in this work together with the preliminary results have been filed as an **European Patent** [HD4]. A detailed discussion with experimental evaluation of the design is the subject of a manuscript which is under preparation.

## 5.2 Introduction

Micro-coils are proved to enhance the detection performance for the small sample volumes. Nevertheless, several challenges are associated with the micro-coils. Two disadvantages of the micro-coils were listed in Chapter 4, i.e., intrinsic low spatial resolution because of their compactness, and their inefficiency in multinuclear detection.

Another challenge preventing the wide-spread use of micro-coils is the handling of the coil and sample. Loading the sample in these coils is not as simple as a standard coil. In general, there are two different methods for this purpose: i) using a piping system which transfers the sample from the reservoir to the detection zone and collects it back [31, 220, 221]; ii) loading the sample manually at the sample chamber next to the coil [26, 29, 39]. The piping system requires a relatively large amount of sample to ensure that the sample is properly loaded at the detection zone. It means that most of the sample stays in the piping system and does not contribute to the signal, which contradicts the main purpose of the micro-coils, being useful where the sample is limited. Manual loading of the sample into the detection zone is also time-consuming and requires special care to avoid air bubbles. Furthermore, it requires the probe to be removed from the bore and inserted back after sample loading. As a result, a fine shim is required every time the probe is inserted. In general micro-coils offer a lower filling factor since all the domains do not scale down similarly. Moreover, since NMR



is a non-destructive test and the sample can be recollected after the experiment, the need for a low sample volume is trivial.

As discussed in Chapter 3, a more general deficiency of the NMR experiments (regardless if in micro-domain or not) is the case where conductive structures exist inside the field of view (FOV) of the coil. It was concluded that the best designs employ either conductors parallel to the  $B_1$  direction or ultra-thin conductive layers. It is worth mentioning again that ultra-thin layers are not a choice when high current amplitudes are required, e.g. current collectors of an energy storage device.

Another issue, stemming from the low sensitivity nature of the NMR, is the case where sample geometry and coil geometry are not compatible. Therefore, the filling factor of the coil is small, i.e. the total number of spins in the FOV is small. A class of potentially interesting samples to be studied with NMR are 2D samples, e.g. sputtered thin material layers, deposited and laminated layers, spray-coated films, inkjet-printed objects, biofilms, such as biological tissue slices as well as thin tissue biopsies. Therefore, volume coils such as conventional saddle or solenoid coils are not very efficient for these samples. The planar coils are more favourable in this case as they offer a higher filling factor. Nevertheless, even for a planar coil, the efficiency of the experiment is not very high since the overlap between the sample and FOV is not large.

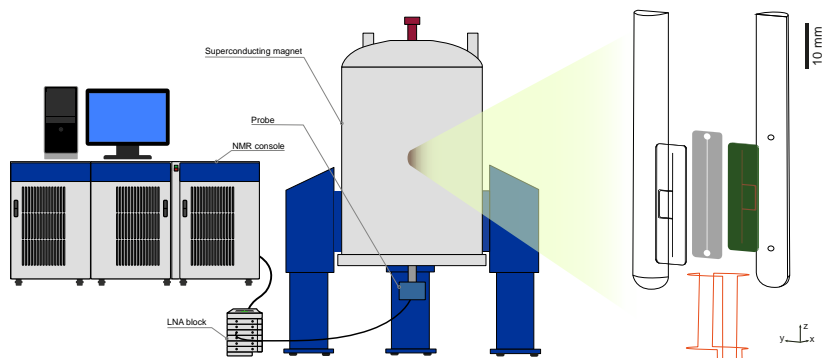
This chapter introduces a novel design consisting of a pair of passive elements, as illustrated in Figure 5.1. This structure is coupled to the standard saddle coil and focuses  $B_1$  field at a certain volume. The focused field is perpendicular to the initial  $B_1$  field due to the unique geometry of the adaptor. Employing a specifically designed holder, this adaptor, known as broadband stripline Lenz-lenses (BBSL), can be treated similar to a standard sample tube. It means that the sample can be loaded into the adaptor outside the magnet and after proper sealing, the assembly can be dropped inside the magnet. The only point to be considered is the direction of the wings with respect to the saddle coil. As the result, a small amount of sample is required for the experiment and, at the same time, no adjustment to the hardware is required, hence the shim is maintained.

Thanks to its planar geometry, inherited from its stripline design, the susceptibility distortions are minimised and the final signal exhibits high resolution. The self-resonance frequency of these structures are relatively high (GHz range) and their performance is frequency independent. Therefore, the broadband stripline has a broadband performance and can be employed at any desired frequency as long as the conventional NMR coil is capable of providing that frequency. Therefore, unlike micro-coils, this adaptor is fully compatible with multinuclear detection.

Regarding the 2D samples, the sample can be sandwiched between the lobes of the broadband stripline. The filling factor is improved as the adaptor focuses the field at the sample region. Besides, since the field is flipped, broadband stripline is a good choice to penetrate inside the samples which contain conductive elements. In its extreme case, the whole adaptor can be designed to simultaneously function as both flux concentrating element and, for example, an energy storage device. In contrary to the standard NMR experiments on the energy storage devices, where field attenuation by the electrodes is considerable, employing broadband stripline amplifies the field and enhances sensitivity remarkably. This enhancement enables higher temporal and/or spatial resolutions, which is extremely advantageous for *in situ* experiments. Considering all these features, broadband stripline is a good candidate for analysing and studying small sample volumes, can enhance the NMR experiments on the hard geometries, and unlocks new applications for NMR.

### 5.2.1 Experimental set-up

The experimental setup is designed based on a conventional NMR experiment. An 11.74 T superconducting magnet, a standard NMR probe, and the signal processing chain have been used as depicted in Figure 5.1. In addition, a conventional 10 mm saddle coil similar to the commercially available coils was used in this experiment. The coil is oriented so that the RF field at the centre of the coil is along the  $x$ -axis. A broadband stripline adaptor is used in



**Figure 5.1:** The experimental setup consisting of the standard NMR hardware (saddle coil, probe, superconducting magnet, etc.) and broadband stripline insert. The insert is designed so that it has an outer geometry similar to the 10 mm tube and consists of two PCBs patterned for the metallic loops and a membrane to hold the sample.

this experiment instead of the 10 mm sample tube. As shown in Figure 5.1, the proposed adaptor consists of three elements: i) a dielectric membrane in which the microfluidic channel is defined; ii) a pair of PCBs with broadband stripline patterns; iii) a pair of PMMA pieces which serves to fix PCBs and the microfluidic membrane.

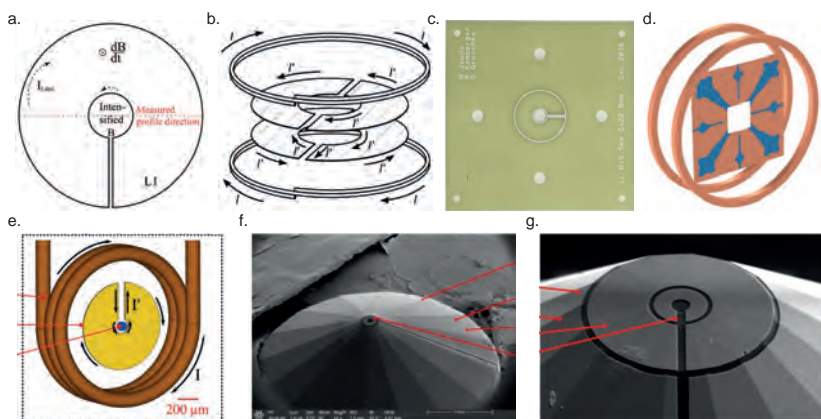
The metallic loops patterned on the PCBs consist of two main segments: the straight stripline which is along the nominal  $z$ -axis, and the flux collection segment which can be in a rounded or rectangular shape. In order to achieve the best performance, the loops shall be identical with the straight segments facing each other at two sides of the microfluidic channel and the flux collector segments at the opposite sides of the channel.

## 5.3 Theory

### 5.3.1 Working principle of Lenz lenses

Lenz lens is a metallic structure, being inductively coupled to an external coil. This add-on works based on the Lenz law and collects the flux at a wide area

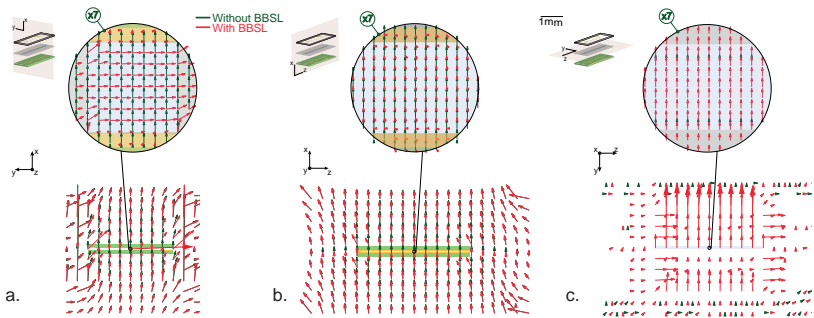
(corresponding to a closed loop) and generates a secondary field according to the current induced in the loop [222]. This tool has been exploited as an intermediate stage to adapt the sample and coil geometries and enhance the sensitivity of the NMR detector [50–52, 56]. Figure 5.2 depicts different Lenz lens structures, being studied in the literature. These add-ons have been proved useful in extreme situations (extra high pressure or temperature), where NMR coils fail to operate, in order to guide and concentrate the flux at the detection point [53–55]. Although their flux collection and concentration performance are poorer compared to the resonator circuits [52], the broadband performance of the Lenz lens structures makes them a unique tool for multinuclear detection experiments.



**Figure 5.2:** Different Lenz lens structures reported in the literature; a. a disk structure (reproduced from Ref. [222]). b. Two disk structures coupled to Helmholtz coil (reproduced from Ref. [50]). c. A wireframe structure based on PCB technology (reproduced from Ref. [52]). d. A topology-optimised structure couple to a Helmholtz coil (reproduced from Ref. [56]). e. A disk structure (reproduced from Ref. [53]). f. A two-stage disk structure couple to a solenoid coil (reproduced from Ref. [54]). g. A three-stage disk structure (reproduced from Ref. [55]).

Unlike the previously studied Lenz lenses, broadband stripline consists of two identical lobes. Each lobe of broadband stripline acts as an obstacle for the incident flux and deforms it to circumvent the lobe. Considering just one lobe,

the flux is more concentrated around its periphery and returns to the primary distribution at far distances from the lobe. By adding the secondary lobe to the system, in a configuration illustrated in Figure 5.1, the flux is compressed in between the two lobes at their overlapping edge. As shown in Figure 5.3, this compression results in a high-intensity laminar flux, which is  $90^\circ$  rotated with respect to the primary flux. This region can be exploited as the sample volume in order to take advantage of the field amplification. Moreover, projection of the  $B_1$  into a second direction can be employed to circumvent conductive objects shielding the sample, e.g. electrodes in the energy storage device, electrochemistry experiments, electrophoresis, dielectrophoresis.



**Figure 5.3:** Distribution of the magnetic flux in the absence and the presence of the BSLL at different cross-sections. BSLL flips the flux by  $90^\circ$  and also concentrates it at the detection zone (highlighted with light blue). The insets show the flux distribution at the sample volume. In order to facilitate the comparison, the flux in the absence of broadband stripline is multiplied by seven in the insets.

### 5.3.2 Figures of merit

In order to evaluate the performance of the proposed design and optimise the geometry, four figures of merit have been considered. Accordingly, the results of the RF simulations were post-processed to generate the nutation signal corresponding to each design.  $B_0$  simulations were also performed for different geometries and the results were processed together with the RF simulations to

produce the NMR spectra. The effect of  $T_2$  relaxation was not considered here. Therefore, the width of the spectrum at its half-height (FWHM) is not a reliable parameter to determine the spectral resolution. Instead, the ratio between the amplitude of the highest peak and the integral of the spectrum for each geometry is considered as the measure for the spectral resolution. The calculated spectra are in the absence of any shim. Additionally,  $B_0$  in the absence of the saddle coil and the inserts was assumed perfectly uniform.

### 5.3.3 Pre-adjustments

#### Geometrical settings

As the main NMR coil, a saddle coil with 12 mm diameter,  $120^\circ$  loop opening angle, 20 mm height, and  $100\ \mu\text{m}$  wire diameter was considered. In order to collect maximum flux using the loops and simultaneously be compatible with the standard 10 mm NMR tube geometry, the flux collectors were assumed rectangular with the width equal to 4 mm. The thickness of the stripline and the flux collector segments were set  $40\ \mu\text{m}$  to be consistent with the metal thickness in PCB technology ( $35\ \mu\text{m}$ ). The other parameters to be evaluated were the stripline length, the stripline width, the width of the flux collector track, and the distance between the lobes. Without loss of generality, all the analysis were performed assuming a total sample volume of 600 nl.

The stripline width determines the field homogeneity, field magnification, and the power dissipation in that segment. Nevertheless, the width of the flux collector track is of less importance and should be selected more than the stripline width in order to reduce the total power dissipation in the loops and consequently the noise level. In this case, it was selected  $3 \times$  the stripline width. The stripline length was adjusted based on the total sample volume, the width of the sample volume, and the height of the sample volume. The upper limit for the stripline length is the coil height. RF field maps at different configurations reveal that the homogeneous RF field region, generated by the striplines, can be extended to about 50 % beyond the stripline width. It means that the width

of the sample volume can be adjusted accordingly. The channel height was assumed the same as the distance between the two striplines.

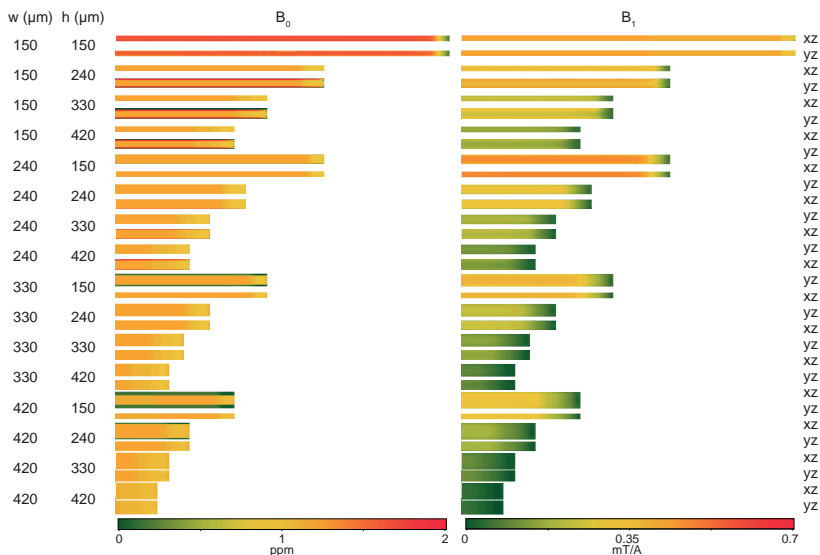
### Simulation preferences and settings

**RF simulations:** *Electromagnetic Waves, Frequency Domain* interface of *RF module* of COMSOL MultiPhysics® 5.5 (COMSOL AB, Sweden) was used to perform the RF simulations. The maximum tolerable relative error for these simulations was adjusted to 0.01 %. Geometry optimisations were performed at 500 MHz corresponding to the  $^1\text{H}$  Larmor frequency at 11.74 T. The final design was then also simulated at 150 MHz and 200 MHz to evaluate the frequency response of the device. These values were selected considering three frequency bands in which NMR active nuclei are distributed in (see Figure 2.1 and Section 4.3.2 for more details). All the simulations were performed using 1 W applied power to the coil terminals. In RF simulations for the geometry optimisation, the effects of the PCB substrate, sample, and the membrane were ignored to reduce the computation costs. The corresponding material properties, e.g., permittivity and permeability values, were assigned according to Sections A1.

**Susceptibility simulations:** *Magnetic Fields, No Currents* (MFNC) interface of *AC/DC module* of COMSOL MultiPhysics® 5.5 (COMSOL AB, Sweden) was employed for the susceptibility simulations. The maximum tolerable relative error of these simulations was set to 0.01 ppb. The permeability values of different materials are listed in Section A1.

#### 5.3.4 Geometry optimisation

Both stripline width ( $w$ ) and spacing between the loops ( $h$ ) were swept from 150  $\mu\text{m}$  to 420  $\mu\text{m}$  with steps of 90  $\mu\text{m}$ . The simulation results for 16 different combinations of  $w$  and  $h$  are given in Figure 5.4. Since the structures are symmetric with respect to the  $xy$ -plane, just half of the sample volume is plotted.

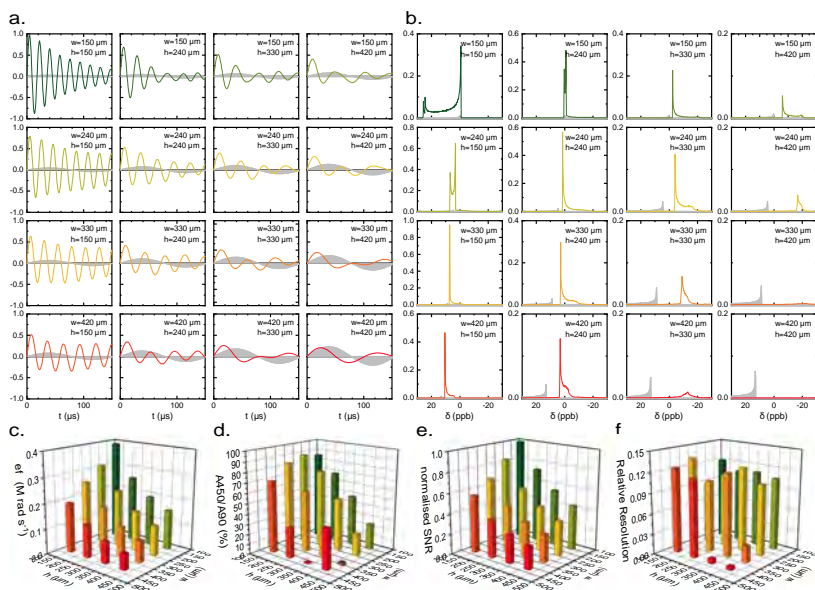


**Figure 5.4:**  $B_0$  and  $B_1$  distribution of broadband stripline with different  $h$  and  $w$ . The plots correspond to just half of the sample volume and to the middle of the channel.

In  $B_0$  plots just the  $z$  component of the field is illustrated whereas in  $B_1$  plots the projection of the field on the  $xy$ -plane is shown.  $B_0$  simulation results reveal that there is an almost uniform field all over the sample volume except at the extremes where the flux collection segment meets the straight stripline and also the stripline ends. Considering  $B_1$  simulations, the field amplitude reduces by  $w$  and  $h$ . Besides, the sample volume corresponding to the joint has a lower field amplitude, compared to the rest of the sample. It is mainly because of the direction of current in that region which results in a field along the  $z$ -axis.

The simulation results, in the sample region, were post-processed with MATLAB® R2018a (Mathworks Inc., USA) to calculate the nutation signals and the NMR spectra. The spatial sampling ( $7\ \mu\text{m}$ ) was performed on the simulation results while collecting the data for post-processing. Figure 5.5 summarises the results. In addition, similar sample geometries were simulated and post-processed for the case where no broadband stripline adaptor exists. These





**Figure 5.5:** 16 different configurations for the broadband stripline adaptor have been simulated in order to determine the optimum combination of the width of the strips ( $w$ ) and the spacing between the lobes ( $h$ ). The simulation results were processed to calculate: a. nutation signals for different configurations in comparison with the case where no broadband stripline adaptor is used (grey signals); b. NMR spectra following a  $90^\circ$ -pulse and collected for different configurations together with the case where no broadband stripline adaptor is employed (grey spectra); c. excitation efficiency; d.  $B_1$  homogeneity; e. relative SNR, f.  $B_0$  homogeneity (indicated by the sharpness of the spectra).

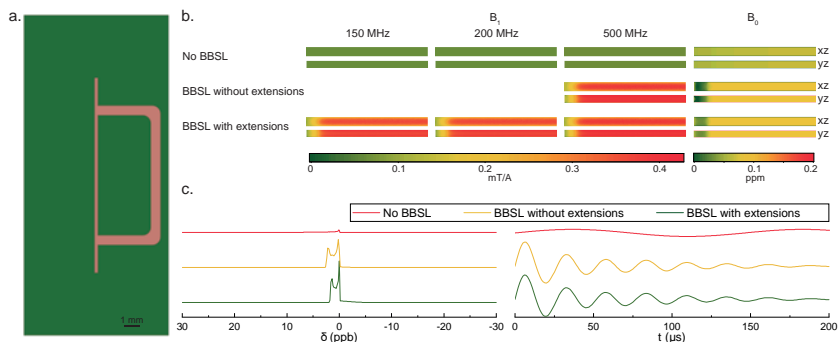
simulations (shown in grey colour) serve as the reference to evaluate the performance of broadband stripline adaptor. The results, presented in Figure 5.5, show that the excitation efficiency and the relative SNR decrease with strip width and spacing between the loops.  $B_1$  homogeneity is maximum when the strip width is  $240\ \mu\text{m}$  for all spacings between the loops. Nevertheless, the spacing between the loops degrades  $B_1$  homogeneity.

The spectral sharpness is a more complex parameter. While there are two distinct peaks in the first spectrum (corresponding to  $w = 150\ \mu\text{m}$  and  $h = 150\ \mu\text{m}$ ), these peaks merge into one by increasing either the strip width or the spacing

between the loops. According to the results, the best spectral sharpness belongs to the case with  $w = 330 \mu\text{m}$  and  $h = 150 \mu\text{m}$ . It corresponds to the fact that for  $h = 150 \mu\text{m}$ , the whole sample volume is distorted almost uniformly as a result of copper tracks. In addition, distance between the edges of tracks is so that the distortions resulting from microfluidic walls is negligible. As a good compromise and also considering the restrictions imposed by the fabrication (given in Section 5.4), a strip width of  $200 \mu\text{m}$  and the spacing between the loops equal to  $230 \mu\text{m}$  were selected. Consequently, the length of the strip is  $8.7 \text{ mm}$ .

In order to further improve the spectral resolution,  $B_0$  distribution at the sample region was further investigated. As depicted in Figure 5.4, the material discontinuity at two extremes of the stripline is one of the reasons of the susceptibility distortions and line broadening. Therefore, the straight segments were extended 20 % along the  $z$ -axis at each side (see Figure 5.6) to push these distortions out of the detection zone. As these segments do not carry current and do not produce any RF field, they do not contribute to the signal. Accordingly,  $B_0$  distortions in their vicinity do not have a destructive effect on the performance of the system. According to the simulation results presented in Figure 5.6, the spectral sharpness is enhanced (by 33 %) in the presence of the extensions while the other parameters are intact.

In the next step, the broadband performance of the final design was studied. In order to decouple the performance of the adaptor from the performance of the saddle coil, the same sample volume and coil have been simulated without considering the broadband stripline insert in a secondary simulation. The sample geometries in the second simulations were considered to be the same as broadband stripline case but the PCB and copper tracks were replaced with the membrane. For this purpose, the performance was studied at 150 MHz, 200 MHz, and 500 MHz. Figure 5.6 depicts the simulation results for these configurations. The figures of merit are also listed in Table 5.1. According to these results, the nutation frequency increases  $\sim 5.8 \times$  regardless of frequency whereas SNR experiences  $\sim 5.3 \times$  enhancement. The improvements are



**Figure 5.6:** a. CAD design of the broadband stripline with the extensions on a PCB. b.  $B_0$  and  $B_1$  simulations for the optimum geometry compared to the case where no broadband stripline adaptor exists and where the broadband stripline adaptor does not have any extensions.  $B_1$  simulations at different frequencies prove that the performance of the broadband stripline adaptor is frequency independent.  $B_0$  simulations show improvement at the extremes of the sample volume when the extension is adapted. c. NMR spectra (at 500 MHz) and nutation signals also reveal superior performance of the case where a broadband stripline adaptor is equipped with the extensions.

achieved with the cost of a lower  $B_1$  homogeneity. The spectral resolution is also enhanced according to the simulation results. It is attributed to the fact that the optimised geometry was selected so that the copper tracks and PCBs have a constructive effect on the overall field distribution inside the sample region.

**Table 5.1:** Figures of merit of a broadband stripline Lenz lens in comparison to the saddle coil (in brackets) for the same sample volume.

	150 MHz	200 MHz	500 MHz
excitation efficiency ( $\text{Mrads}^{-1}$ )	75 [13]	100 [17]	249 [43]
$B_1$ homogeneity (%)	52 [100]	53 [100]	54 [100]
Relative SNR (-)	5.3 [1]	5.3 [1]	5.3 [1]
Spectral sharpness ( $\text{Hz}^{-1}$ )	0.10 [0.03]	0.10 [0.03]	0.10 [0.03]

## 5.4 Fabrication and assembly

### 5.4.1 PCB

The final geometry discussed and evaluated in the previous section was selected for the fabrication. The PCB layout was designed by EAGLE® (Autodesk Inc., USA). PCBs were manufactured by multi-cb® (Poole, GB). The PCB specifications are: substrate material-FR4, substrate thickness-0.3 mm, metallisation layers-1, metallisation thickness-35  $\mu\text{m}$ , metallisation surface finish-chemical silver, with a passivation layer on top of the metallic layers and markings on the backside of the PCBs.

### Material selection

In order to avoid oxidation of the copper structures, a surface finish layer is employed. Although the electroless nickel immersion gold (chemical gold) and electroless nickel electroless palladium immersion gold offer better performance in terms of mechanical and chemical stability, the Nickel content in those materials can hinder the NMR performance. Instead, chemical silver is employed as the surface finish.

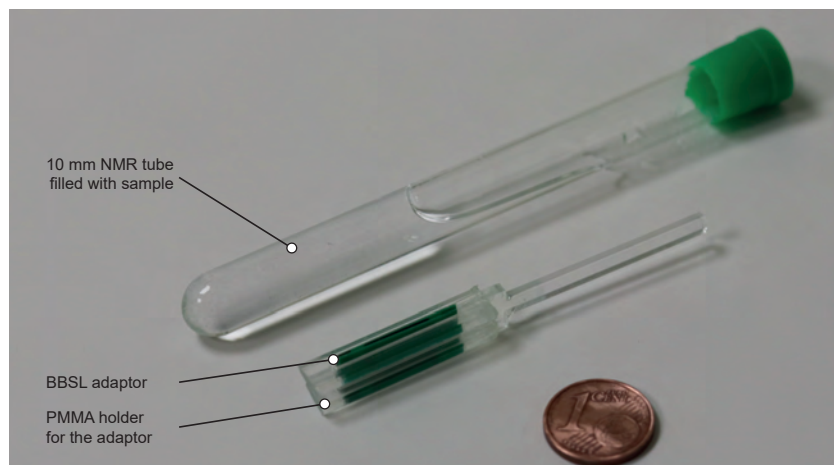
### 5.4.2 Membrane

The membrane is a double-sided clear polyester tape (HB397F, hi-bond® tapes Ltd., UK) with 230  $\mu\text{m}$  thickness. Engraving the channel in the membrane and cutting it into the required size was performed using an infrared Laser (VLS3.50, UNIVERSAL® Laser Systems Ltd., Austria). The membrane was then sandwiched between two PCBs as depicted in Figure 5.1.

### 5.4.3 Holder

The holder is supposed to form a geometry similar to the 10 mm sample tube. It consists of two sides with especial grooves for the PCBs and membrane, as well as the inlet and outlet for the microfluidics. These two sides were

tightened together as shown in Figure 5.1. For the proof-of-concept experiments a simplified holder was employed. This holder (shown in Figure 5.7) consists of a PMMA stick to carry the PCB assembly and fix its location inside the 10 mm NMR tube. In addition, the membrane was also eliminated to allow the sample all around the PCBs.



**Figure 5.7:** A photograph of the configuration for the MRI experiment consisting of a 10 mm tube filled with the sample, the broadband stripline Lenz lens adaptor, and the PPMA holder.

## 5.5 Characterisation

### 5.5.1 Experiment configuration

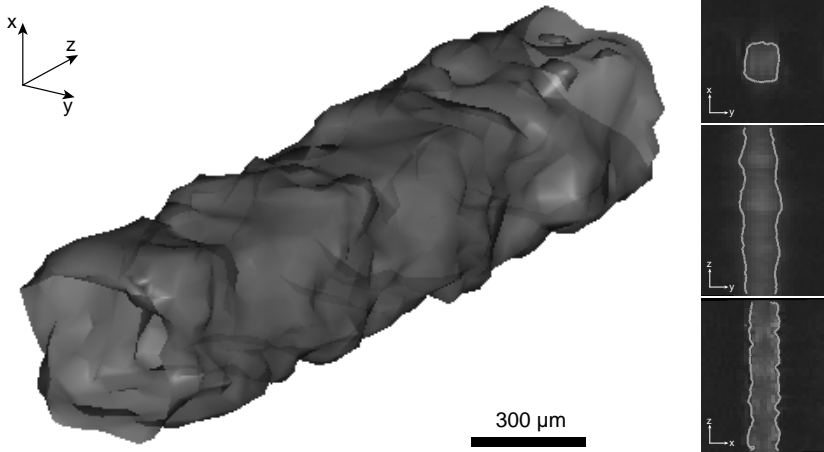
The simplified assembly was inserted inside a 10 mm sample tube and the tube was filled with 4 mM copper sulphate ( $\text{CuSO}_4 \cdot 5\text{H}_2\text{O}$ ) and 75 mM sodium chloride ( $\text{NaCl}$ ) in deionised water. All the chemicals were purchased from Sigma Aldrich® (Germany). Since the sample is not limited by the membrane, the MRI experiment can reveal the field distribution all over the space between the PCBs and around them.

The experiments were performed with an 11.74T Avance III Bruker NMR system (Bruker BioSpin, Rheinstetten, Germany) and using ParaVision 6.0.1 (Bruker, Germany) at 30 °C. The standard 10 mm saddle coil was mounted on top of the probe. Signal was routed through a narrow-band pre-amplifier (1H LNA MODULE 500, Bruker BioSpin, Rheinstetten, Germany) with 1 dB noise figure. The gradient sleeve was inserted afterwards and the tube was fixed to the gradient so that the broadband stripline insert is located inside the saddle coil and its wings are perpendicular to the field generated by the coil.

A 3D FLASH sequence was performed to evaluate the distribution of  $B_1$  field. The settings for the sequence are: TR/TE - 100 ms/4 ms, isotropic resolution - 50  $\mu\text{m}$ , Tscan - 850 min, FOV -  $2 \times 2 \times 2 \text{ mm}^3$ , bandwidth - 7.5 kHz, and 325 averages. Duration of the excitation pulse was fixed at 1.4 ms.

### 5.5.2 MRI results

The reference power for a block pulse of 1 ms was automatically calculated by ParaVision to be 0.183 W. This value determines the average  $B_1$  field all over the sample volume. Since  $B_1$  field at the space between the loops is much higher than the rest of the sample, the flip angle was adjusted manually to have the best contrast between the volume under-study and the rest of the sample. The best contrast was achieved at  $1^\circ$  flip angle corresponding to an excitation power of 0.18 mW. Figure 5.8 shows the reconstructed sensitive region. 3D reconstruction of the image was performed using Slicer 14.10.2 (<https://www.slicer.org/>) [223]. According to this result, the sensitive volume is a cuboid with the average cross-section of  $300 \times 250 \mu\text{m}^2$ . The length of the cuboid is limited by the FOV set in the MRI experiment (2 mm). The  $zx$ -cross-section shows a steep contrast which is defined by the PCBs and strips. In contrary, the  $yz$ -cross-section shows a gradual transition from bright to dark voxels at the margins. It is attributed to the presence of the sample around the PCBs and gradual decay of the field amplitude.



**Figure 5.8:** The reconstructed 3D image of the sensitive volume of the broadband stripline together with the cross-sections of the sensitive volume at different planes.

## 5.6 Discussion and conclusion

Lenz lens structures found to be useful in NMR experiments specially if investigation on a certain location of the sample is required. In addition to their simple geometry, their broadband performance paves the road for their wide-use. Despite their interesting performance, they have not been exploited for the standard NMR coils, where these adaptors can be especially helpful to adapt the micro-samples to the macro-coils. In this work, a novel topology of the Lenz lens structures is proposed to address this need. In addition to RF field concentration and filling factor improvement, this design also flips the RF field at the region of interest. This feature facilitates hyphenated NMR experiments where conductor elements are required inside the detection zone. The stripline based design of these add-ons results in minor susceptibility distortions and compatibility with thin-film samples. The broadband stripline structure is designed to look like a 10 mm sample tube and can be treated similarly. Therefore,

the sample handling issues, e.g., being time-consuming and not efficient, for micro-coils can be eliminated.

Performance of the broadband stripline have been simulated considering both  $B_0$  and  $B_1$  fields. The simulation results were processed to extract four figures of merit. Based on these figures of merit and restrictions imposed by the fabrication, an optimum geometry for the broadband stripline has been selected for a total sample volume of 600 nl. Moreover, it was shown that extending the striplines length beyond the loops enhances spectral resolution. The broadband behaviour of the broadband stripline was also studied through the simulations. The MRI experiment performed using the optimum geometry is in good agreement with the simulation results and clearly shows field concentrating at the region of interest.

### **5.6.1 Challenges**

#### **Alignment of the strips to $B_0$ and $B_1$**

Similar to the stripline based NMR coils, alignment of the adaptor to  $B_0$  field is crucial. Additionally, in this design, the sample is relatively long and therefore a slight misalignment can influence the results considerably. Moreover, the alignment of the insert to  $B_1$  field plays a major role. Misalignment in this case reduces the collected flux by the loops and the RF field at the sample region.

#### **Sealing the channel and inlet/outlet**

This works relies on low-cost manufacturing processes to fabricate the inserts. Therefore, PCB and off-the-shelf materials (PMMA, and double-sided polyester tape) were used. As one of the disadvantages, the channel could not be sealed efficiently. Therefore, sample leakage and air bubbles formation can happen during the experiment. The bubbles destroy the results by introducing susceptibility mismatches. As the second issue, the alignment of the two lobes was not precise. The other challenge is the susceptibility issues arising from the PCB material and the voids happening between the membrane and the PCBs. The background



signal stemming from the PCBs, the membrane, and the PMMA structures is also another disadvantage of this technique. In order to eliminate these issues, the assembly can be fabricated using MEMS techniques. Thanks to the planar geometry of the assembly, the fabrication process is straight forward. Integration of the microfluidic channel is also easier in this case. Moreover, smaller strip width and spacing between the loops is achievable when migrating to the cleanroom-based techniques. Microfabrication also allows for proper material selection considering both background signals and susceptibility matching. Another source of  $B_0$  distortions is the surface of the metallic tracks. As the RF field is very strong at the surface, even a slight  $B_0$  distortion at those locations contributes to the spectral resolution. The effect of metal roughness for stripline coils has been thoroughly studied by Chen [39]. A surface treatment procedure can be helpful to address this issue. A secondary option is to eliminate sample at those regions by employing a thin passivation layer which is transparent to the NMR application and has a susceptibility matched to that of metallic structures.

### **Sample loading inside the channel**

Hydrophobicity of the PCB surface and microfluidic channel exacerbate the filling process of the microfluidic channel. Besides, it increases the possibility of trapped air bubbles inside the channel. In order to ensure reliable filling of the sample, the PCB surface was treated with  $O_2$ -Plasma before manufacturing the assembly. As a complimentary process, after filling the channel with sample, the assembly was left inside a vacuum chamber for few minutes to remove air bubbles.

### **5.6.2 Suggestions**

As mentioned in the previous section, fabricating the structures using cleanroom techniques can enhance the performance of the system considerably. The main improvements which can be expected are better alignment of the struc-

tures, higher spectral resolution, finer structures, enhanced hydrophilicity of the microfluidic channel, less trapped air bubbles, and less background signal. These structures can also be designed to have tapered shape in order to enhance sensitivity at certain locations. Tijssen [40] has proposed a tapered stripline coil to generate a field gradient. Similar geometries can be employed using the broadband stripline inserts.

## 6 Conclusion and outlook

### 6.1 Conclusion

Since its first successful demonstration in 1995, micro-NMR has been evolved to push the boundaries of NMR applications beyond standard techniques. One of the main advantages of micro-NMR is its customizability. It means that, contrary to the conventional NMR, the hardware developer has the freedom to modify and optimise the detection hardware according to the specific problem. As a result, numerous types of detectors and hardware can be found in the literature. Building upon this advantage, this thesis has studied and demonstrated three solutions for different micro-NMR applications.

In the third chapter, a miniaturised electrochemistry cell is discussed which is compatible to the Helmholtz coil. Out of eight potential geometries introduced and studied theoretically, four were fabricated and tested experimentally. The ultra-thin electrode geometry, with electrode thickness  $0.001 \times$  the skin depth, was found to be fully compatible with NMR. Besides, mindful design of the narrow-channel sidewall geometry exhibited an even superior performance compared to the case where no electrode exists. Thanks to these two geometries, NMR was employed for the first time to monitor *in situ* electrodeposition processes and localised multi-enzyme reactions in micro-scales.

The fourth chapter reports on a broadband detector, consisting of a coil and a microfluidic channel, which enables NMR measurements at a wide bandwidth. A thorough study of the excitation and the detection process was performed in order to investigate the performance of the broadband coils. The coil geometry and microfluidic channel were optimised accordingly. NMR spectra of

seven different nuclei, which is already a record, were collected without any modification to the hardware using this detector.

The fifth chapter introduces a broadband adaptor, being employed together with a standard NMR coil, in order to focus the field at a small sample volume. This adaptor additionally flips the RF field at the detection region. This feature makes this add-on especially advantageous in order to circumvent obstacles, such as conductive elements, in the detection region. Simulations reveal  $5.3\times$  improvements in the SNR of the collected signal. MRI experiments confirm this enhancement.

In parallel to these milestones, a simulation toolkit was developed to predict and optimise these micro-devices reliably. Thanks to this simulation toolkit, 'digital twin's of the NMR spectra were obtained and NMR figures of merit were calculated as the objective functions for the geometrical optimisation. This process accelerated the development phase by avoiding unnecessary iterations of fabrication and experiments.

Considering the ultimate goal of studying proteins using NMR, the achievements of this research can be considered as a leap towards a hybrid lab-on-a-chip solution. Nevertheless, multiple other steps should be taken in order to fulfil this ambitious goal.

## 6.2 Outlook

Several directions can be taken in order to continue on the achievements of this thesis. The potential hardware enhancements or applications were discussed in each chapter individually. Various other interesting applications are anticipated by combining the achievements of different chapters.

The simulation toolkit discussed in this thesis can be adapted to topology optimisation procedures to improve design performance. Furthermore, fabrication and physical constraints can be included in the topology optimisation procedures. Considering the customizability of the micro-NMR devices, this automation process can fuel future progress in the field.

The electrode structures of the electrochemistry platform can be readily integrated into the broadband stripline add-on. For this purpose, the striplines of the add-on can be exploited as both electrochemistry sites and RF current paths. This system can be employed in numerous micro-NMR applications, e.g., energy storage devices or electrochemical process, with no modification to the standard NMR hardware. Nevertheless, the additional filters are required to block the RF signals from leaking to the DC lines.

Employing both sidewall and ultra-thin planar electrodes enable a more sophisticated electrode array structure. This structure, being supplied with a programmable demultiplexer circuit, can be employed to generate arbitrary gel topologies. Coupling various enzymes to different segments of the gel arrays would unlock new features towards organ-on-a-chip systems. This system can be integrated into a broadband NMR detector to perform multi-dimensional NMR experiments. Observation of the mimicked biochemical reactions of the organs, employing multi-dimensional NMR, would be a breakthrough in the field.

Integrating the electrochemistry platform and the broadband detector is a wish towards the ultimate goal of this research. In this case, multi-nuclear NMR techniques can be applied to monitor the on-going reactions or study enzymes and, in a more ambitious case, proteins. Nevertheless, in this case, the spectral resolution considerations are stricter. Consequently, the system should be equipped with proper shim-on-chip structures. Moreover, the multi-dimensional NMR experiments mandate additional filter stages between the coil and the electronics to route the signals and prevent any damage to the hardware. Employing an on-chip LNA, which is "co-optimised" for the broadband coil and integrating all the required filter elements into the LNA, would be a further step towards the ultimate goal.



## Bibliography

- [1] Chen, C.-N., and Hoult, D. I. *Medical Science Series*; Adam Hilger: Bristol and New York, **1989**; p 341.
- [2] Levitt, M. H. *John Wiley & Sons Ltd*, 2nd ed.; John Wiley & Sons Ltd: Chichester, **2008**; p 752.
- [3] Mispelter, J., Lupu, M., and Briguet, A. *NMR Probeheads for Biophysical and Biomedical Experiments*, 2nd ed.; IMPERIAL COLLEGE PRESS: London, **2015**.
- [4] Hoult, D. The origins and present status of the radio wave controversy in NMR, *Concepts in Magnetic Resonance Part A*, **2009**, *34A*, 193–216.
- [5] Hoult, D., and Ginsberg, N. The Quantum Origins of the Free Induction Decay Signal and Spin Noise, *Journal of Magnetic Resonance*, **2001**, *148*, 182–199.
- [6] Hoult, D. I. The principle of reciprocity in signal strength calculations - A mathematical guide, *Concepts in Magnetic Resonance*, **2000**, *12*, 173–187.
- [7] Hoult, D. I., and Richards, R. E. The signal-to-noise ratio of the nuclear magnetic resonance experiment, *Journal of Magnetic Resonance (1969)*, **1976**, *24*, 71–85.
- [8] Hoult, D. The NMR receiver: A description and analysis of design, *Progress in Nuclear Magnetic Resonance Spectroscopy*, **1978**, *12*, 41–77.

- [9] Webb, A. Microcoil nuclear magnetic resonance spectroscopy, *J. Pharm. Biomed. Anal.*, **2005**, 38, 892–903.
- [10] Webb, A. Radiofrequency microcoils for magnetic resonance imaging and spectroscopy, *Journal of Magnetic Resonance*, **2013**, 229, 55–66.
- [11] Kentgens, A. P. M., Bart, J., van Bentum, P. J. M., Brinkmann, A., van Eck, E. R. H., Gardeniers, J. G. E., Janssen, J. W. G., Knijn, P., Vasa, S., and Verkuijlen, M. H. W. High-resolution liquid- and solid-state nuclear magnetic resonance of nanoliter sample volumes using microcoil detectors, *The Journal of Chemical Physics*, **2008**, 128, 052202.
- [12] Fratila, R. M., and Velders, A. H. Small-Volume Nuclear Magnetic Resonance Spectroscopy, *Annual Review of Analytical Chemistry*, **2011**, 4, 227–249.
- [13] Badilita, V., Meier, R. C., Spengler, N., Wallrabe, U., Utz, M., and Korvink, J. G. Microscale nuclear magnetic resonance: a tool for soft matter research, *Soft Matter*, **2012**, 8, 10583.
- [14] Olson, D. L., Peck, T. L., Webb, A. G., Magin, R. L., and Sweedler, J. V. High-Resolution Microcoil <sup>1</sup>H-NMR for Mass-Limited, Nanoliter-Volume Samples, *Science*, **1995**, 270, 1967–1970.
- [15] Badilita, V., Kratt, K., Baxan, N., Mohmmadzadeh, M., Burger, T., Weber, H., Elverfeldt, D. V., Hennig, J., Korvink, J. G., and Wallrabe, U. On-chip three dimensional microcoils for MRI at the microscale, *Lab on a Chip*, **2010**, 10, 1387.
- [16] Xue, K., Sarkar, R., Motz, C., Asami, S., Camargo, D. C. R., Decker, V., Wegner, S., Tosner, Z., and Reif, B. Limits of Resolution and Sensitivity of Proton Detected MAS Solid-State NMR Experiments at 111 kHz in Deuterated and Protonated Proteins, *Scientific Reports*, **2017**, 7, 7444.



- 
- [17] van Bentum, P. J. M., and Kentgens, A. P. M. *Modern Magnetic Resonance*; Springer Netherlands: Dordrecht, **2006**; pp. 353–361.
- [18] Bart, J., Janssen, J., van Bentum, P., Kentgens, A., and Gardeniers, J. Optimization of stripline-based microfluidic chips for high-resolution NMR, *Journal of Magnetic Resonance*, **2009**, *201*, 175–185.
- [19] Conradi, M. S., Altobelli, S. A., and McDowell, A. F. Coil extensions improve line shapes by removing field distortions, *Journal of Magnetic Resonance*, **2018**, *291*, 23–26.
- [20] Kc, R., Henry, I. D., Park, G. H., Aghdasi, A., and Raftery, D. New solenoidal microcoil NMR probe using zero-susceptibility wire, *Concepts Magn. Reson. Part B Magn. Reson. Eng.*, **2010**, *37B*, 13–19.
- [21] van Meerten, S. G. J., van Bentum, P. J. M., and Kentgens, A. P. M. Shim-on-Chip Design for Microfluidic NMR Detectors, *Analytical Chemistry*, **2018**, *90*, 10134–10138.
- [22] Olson, D. L., Lacey, M. E., and Sweedler, J. V. High-Resolution Microcoil NMR for Analysis of Mass-Limited, Nanoliter Samples, *Analytical Chemistry*, **1998**, *70*, 645–650.
- [23] Kratt, K., Badilita, V., Burger, T., Korvink, J. G., and Wallrabe, U. A fully MEMS-compatible process for 3D high aspect ratio micro coils obtained with an automatic wire bonder, *Journal of Micromechanics and Microengineering*, **2010**, *20*, 015021.
- [24] Gruschke, O. G., Baxan, N., Clad, L., Kratt, K., von Elverfeldt, D., Peter, A., Hennig, J., Badilita, V., Wallrabe, U., and Korvink, J. G. Lab on a chip phased-array MR multi-platform analysis system, *Lab Chip*, **2012**, *12*, 495–502.
- [25] Badilita, V., Fassbender, B., Kratt, K., Wong, A., Bonhomme, C., Sakellariou, D., Korvink, J. G., and Wallrabe, U. Microfabricated Inserts

- for Magic Angle Coil Spinning (MACS) Wireless NMR Spectroscopy, *PLOS ONE*, **2012**, 7, 1–8.
- [26] Spengler, N., Moazenzadeh, A., Meier, R. C., Badilita, V., Korvink, J. G., and Wallrabe, U. Micro-fabricated Helmholtz coil featuring disposable microfluidic sample inserts for applications in nuclear magnetic resonance, *Journal of Micromechanics and Microengineering*, **2014**, 24, 034004.
- [27] Meier, R. C., Höfflin, J., Badilita, V., Wallrabe, U., and Korvink, J. G. Microfluidic integration of wirebonded microcoils for on-chip applications in nuclear magnetic resonance, *Journal of Micromechanics and Microengineering*, **2014**, 24, 045021.
- [28] Adhikari, S. S., Zhao, L., Dickmeis, T., Korvink, J. G., and Badilita, V. Inductively coupled magic angle spinning microresonators benchmarked for high-resolution single embryo metabolomic profiling, *The Analyst*, **2019**, 144, 7192–7199.
- [29] Wang, N., Meissner, M. V., MacKinnon, N., Luchnikov, V., Mager, D., and Korvink, J. G. Fast prototyping of microtubes with embedded sensing elements made possible with an inkjet printing and rolling process, *Journal of Micromechanics and Microengineering*, **2018**, 28, 025003.
- [30] Nassar, O., Mager, D., and Korvink, J. G. Wireless Double Micro-Resonator for Orientation Free Tracking of MR-Catheter During Interventional MRI, *IEEE Journal of Electromagnetics, RF and Microwaves in Medicine and Biology*, **2020**, 1–1.
- [31] Wensink, H., Benito-Lopez, F., Hermes, D. C., Verboom, W., Gardeniers, H. J., Reinhoudt, D. N., and van den Berg, A. Measuring reaction kinetics in a lab-on-a-chip by microcoil NMR, *Lab on a Chip*, **2005**, 5, 280–284.

- [32] Eroglu, S., Gimi, B., Roman, B., Friedman, G., and Magin, R. L. NMR spiral surface microcoils: Design, fabrication, and imaging, *Concepts in Magnetic Resonance*, **2003**, *17B*, 1–10.
- [33] Massin, C., Boero, G., Vincent, F., Abenhaim, J., Besse, P.-A., and Popovic, R. High-Q factor RF planar microcoils for micro-scale NMR spectroscopy, *Sensors and Actuators A: Physical*, **2002**, *97-98*, 280–288.
- [34] Grisi, M., Vincent, F., Volpe, B., Guidetti, R., Harris, N., Beck, A., and Boero, G. NMR spectroscopy of single sub-nL ova with inductive ultra-compact single-chip probes, *Scientific Reports*, **2017**, *7*, 1–8.
- [35] Syed Mohammed, Z. A., Puiu, P. D., and Aditya, S. Fabrication of silicon-embedded low resistance high-aspect ratio planar copper microcoils, *Journal of Micro/Nanolithography, MEMS, and MOEMS*, **2018**, *17*, 1.
- [36] Massin, C., Vincent, F., Homsy, A., Ehrmann, K., Boero, G., Besse, P.-A., Daridon, A., Verpoorte, E., de Rooij, N., and Popovic, R. Planar microcoil-based microfluidic NMR probes, *Journal of Magnetic Resonance*, **2003**, *164*, 242–255.
- [37] van Bentum, P. J. M., Janssen, J. W. G., and Kentgens, A. P. M. Towards nuclear magnetic resonance  $\mu$ -spectroscopy and  $\mu$ -imaging, *The Analyst*, **2004**, *129*, 793–803.
- [38] Butler, M. C., Mehta, H. S., Chen, Y., Reardon, P. N., Renslow, R. S., Khbeis, M., Irish, D., and Mueller, K. T. Toward high-resolution NMR spectroscopy of microscopic liquid samples, *Physical Chemistry Chemical Physics*, **2017**, *19*, 14256–14261.
- [39] Chen, Y., Mehta, H. S., Butler, M. C., Walter, E. D., Reardon, P. N., Renslow, R. S., Mueller, K. T., and Washton, N. M. High-resolution

- microstrip NMR detectors for subnanoliter samples, *Physical Chemistry Chemical Physics*, **2017**, *19*, 28163–28174.
- [40] Tijssen, K. C., Bart, J., Tiggelaar, R. M., Janssen, J. H., Kentgens, A. P., and van Bentum, P. J. M. Spatially resolved spectroscopy using tapered stripline NMR, *Journal of Magnetic Resonance*, **2016**, *263*, 136–146.
- [41] van Bentum, P., Janssen, J., Kentgens, A., Bart, J., and Gardeniers, J. Stripline probes for nuclear magnetic resonance, *Journal of Magnetic Resonance*, **2007**, *189*, 104–113.
- [42] van Meerten, S., van Zelst, F., Tijssen, K., and Kentgens, A. An Optimized NMR Stripline for Sensitive Supercritical Fluid Chromatography-Nuclear Magnetic Resonance of Microliter Sample Volumes, *Analytical Chemistry*, **2020**, *92*, 13010–13016.
- [43] Finch, G., Yilmaz, A., and Utz, M. An optimised detector for in-situ high-resolution NMR in microfluidic devices, *Journal of Magnetic Resonance*, **2016**, *262*, 73–80.
- [44] Bart, J., Kolkman, A. J., Vries, A. J. O. D., Koch, K., Nieuwland, P. J., Janssen, H. J., van Bentum, J. P., Ampt, K. A., Rutjes, F. P., Wijmenga, S. S., Gardeniers, H. J., and Kentgens, A. P. A Microfluidic high-resolution NMR flow probe, *Journal of the American Chemical Society*, **2009**, *131*, 5014–5015.
- [45] Oosthoek-De Vries, A. J., Bart, J., Tiggelaar, R. M., Janssen, J. W., van Bentum, P. J. M., Gardeniers, H. J., and Kentgens, A. P. Continuous Flow <sup>1</sup>H and <sup>13</sup>C NMR Spectroscopy in Microfluidic Stripline NMR Chips, *Analytical Chemistry*, **2017**, *89*, 2296–2303.
- [46] Maguire, Y., Chuang, I. L., Zhang, S., and Gershenfeld, N. Ultra-small-sample molecular structure detection using microslot waveguide nuclear spin resonance, *Proceedings of the National Academy of Sciences of the United States of America*, **2007**, *104*, 9198–9203.

- 
- [47] Sharma, M., and Utz, M. Modular transmission line probes for microfluidic nuclear magnetic resonance spectroscopy and imaging, *Journal of Magnetic Resonance*, **2019**, *303*, 75–81.
- [48] Sakellariou, D., Goff, G. L., and Jacquinot, J.-F. High-resolution, high-sensitivity NMR of nanolitre anisotropic samples by coil spinning, *Nature*, **2007**, *447*, 694–697.
- [49] Adhikari, S. S., Wallrabe, U., Badilita, V., and Korvink, J. G. Capacitor re-design overcomes the rotation rate limit of MACS resonators, *Concepts Magn. Reson. Part B Magn. Reson. Eng.*, **2017**, *47B*, e21362.
- [50] Spengler, N., While, P. T., Meissner, M. V., Wallrabe, U., and Korvink, J. G. Magnetic Lenz lenses improve the limit-of-detection in nuclear magnetic resonance, *PLOS ONE*, **2017**, *12*, e0182779.
- [51] Kamberger, R., Göbel-Gueniot, K., Gerlach, J., Gruschke, O., Hennig, J., LeVan, P., Haas, C., and Korvink, J. Improved method for MR microscopy of brain tissue cultured with the interface method combined with Lenz lenses, *J. Magn. Reson. Imaging*, **2018**, *52*, 24 – 32.
- [52] Jouda, M., Kamberger, R., Leupold, J., Spengler, N., Hennig, J., Gruschke, O., and Korvink, J. G. A comparison of Lenz lenses and LC resonators for NMR signal enhancement, *Concepts Magn. Reson. Part B Magn. Reson. Eng.*, **2017**, *47B*, e21357.
- [53] Meier, T., Nan Wang., Mager, D., Korvink, J. G., Petitgirard, S., and Dubrovinsky, L. Magnetic flux tailoring through Lenz lenses for ultrasmall samples: A new pathway to high-pressure nuclear magnetic resonance, *Science Advances*, **2017**, *3*, eaao5242.
- [54] Meier, T., Petitgirard, S., Khandarkhaeva, S., and Dubrovinsky, L. Observation of nuclear quantum effects and hydrogen bond symmetrisation in high pressure ice, *Nature Communications*, **2018**, *9*, 1–7.

- [55] Meier, T., Trybel, F., Khandarkhaeva, S., Steinle-Neumann, G., Chariton, S., Fedotenko, T., Petitgirard, S., Hanfland, M., Glazyrin, K., Dubrovinskaia, N., and Dubrovinsky, L. Pressure-Induced Hydrogen-Hydrogen Interaction in Metallic FeH Revealed by NMR, *Physical Review X*, **2019**, *9*, 031008.
- [56] Wadhwa, S., Jouda, M., Deng, Y., Nassar, O., Mager, D., and Korvink, J. G. Topologically optimized magnetic lens for magnetic resonance applications, *Magnetic Resonance*, **2020**, *1*, 225–236.
- [57] Korvink, J. G., MacKinnon, N., Badilita, V., and Jouda, M. "Small is beautiful" in NMR, *Journal of Magnetic Resonance*, **2019**, *306*, 112–117.
- [58] McKay, R. A. Double-tuned single coil probe for nuclear magnetic resonance spectrometer. Patent num. US 4446431, **1984**; Monsanto Company.
- [59] Holl, S. M., McKay, R. A., Gullion, T., and Schaefer, J. Rotational-echo triple-resonance NMR, *J. Magn. Reson. (1969)*, **1990**, *89*, 620–626.
- [60] Kc, R., Henry, I. D., Park, G. H. J., and Raftery, D. Design and construction of a versatile dual volume heteronuclear double resonance microcoil NMR probe, *Journal of Magnetic Resonance*, **2009**, *197*, 186–192.
- [61] Leach, M. O., Hind, A., Sauter, R., Requardt, H., and Weber, H. The design and use of a dual-frequency surface coil providing proton images for improved localization in  $^{31}\text{P}$  spectroscopy of small lesions, *Med. Phys.*, **1986**, *13*, 510–3.
- [62] Spengler, N., Höfflin, J., Moazenzadeh, A., Mager, D., MacKinnon, N., Badilita, V., Wallrabe, U., and Korvink, J. G. Heteronuclear Micro-Helmholtz Coil Facilitates  $\mu\text{m}$ -Range Spatial and Sub-Hz Spectral

- Resolution NMR of nL-Volume Samples on Customisable Microfluidic Chips, *PLOS ONE*, **2016**, *11*, e0146384.
- [63] Doty, F. D., Inners, R. R., and Ellis, P. D. A multinuclear double-tuned probe for applications with solids or liquids utilizing lumped tuning elements, *J. Magn. Reson. (1969)*, **1981**, *43*, 399–416.
- [64] Grant, C. V., Sit, S. L., De Angelis, A. A., Khuong, K. S., Wu, C. H., Plesniak, L. A., and Opella, S. J. An efficient  $^1\text{H}/^{31}\text{P}$  double-resonance solid-state NMR probe that utilizes a scroll coil, *J. Magn. Reson.*, **2007**, *188*, 279–284.
- [65] Li, Y., Logan, T. M., Edison, A. S., and Webb, A. Design of small volume HX and triple-resonance probes for improved limits of detection in protein NMR experiments, *J. Magn. Reson.*, **2003**, *164*, 128–135.
- [66] Brauckmann, J. O., Janssen, J. W. G. H., and Kentgens, A. P. M. High resolution triple resonance micro magic angle spinning NMR spectroscopy of nanoliter sample volumes, *Phys. Chem. Chem. Phys.*, **2016**, *18*, 4902–4910.
- [67] Collier, K. A., Sengupta, S., Espinosa, C. A., Kelly, J. E., Kelz, J. I., and Martin, R. W. Design and construction of a quadruple-resonance MAS NMR probe for investigation of extensively deuterated biomolecules, *Journal of Magnetic Resonance*, **2017**, *285*, 8–17.
- [68] Martineau, C., Engelke, F., and Taulelle, F. Multiple resonance heteronuclear decoupling under MAS: Dramatic increase of spectral resolution at moderate magnetic field and MAS frequencies, *J. Magn. Reson.*, **2011**, *212*, 311–319.
- [69] Wetterling, F., Högler, M., Molkenthin, U., Junge, S., Gallagher, L., Mhairi Macrae, I., and Fagan, A. J. The design of a double-tuned two-port surface resonator and its application to in vivo Hydrogen- and Sodium-MRI, *J. Magn. Reson.*, **2012**, *217*, 10–18.

- [70] Stromski, M. E., Arias-Mendoza, F., Alger, J. R., and Shulman, R. G. Hepatic gluconeogenesis from alanine:  $^{13}\text{C}$  nuclear magnetic resonance methodology for in vivo studies, *Magn. Reson. Med.*, **1986**, 3, 24–32.
- [71] Doty, F. D. Doubly Broadband Triple Resonance or Quad Resonance NMR Probe Circuit. Patent num. US 5424645A, **1995**; Doty Scientific Inc.
- [72] Doty, F. D., Connick, T. J., Ni, X. Z., and Clingan, M. N. Noise in high-power, high-frequency double-tuned probes, *J. Magn. Reson. (1969)*, **1988**, 77, 536–549.
- [73] Lin, E. C., Wu, C. H., Yang, Y., Grant, C. V., and Opella, S. J.  $^1\text{H}$ - $^{13}\text{C}$  separated local field spectroscopy of uniformly  $^{13}\text{C}$  labeled peptides and proteins, *J. Magn. Reson.*, **2010**, 206, 105–111.
- [74] Kendrick, R. D., and Yannoni, C. S. High-power  $^1\text{H}$ - $^{19}\text{F}$  excitation in a multiple-resonance single-coil circuit, *J. Magn. Reson. (1969)*, **1987**, 75, 506–508.
- [75] Subramanian, R., Lam, M., and Webb, A. RF Microcoil Design for Practical NMR of Mass-Limited Samples, *Journal of Magnetic Resonance*, **1998**, 133, 227–231.
- [76] Subramanian, R., Lam, M., and Webb, A. RF Microcoil Design for Practical NMR of Mass-Limited Samples, *J. Magn. Reson.*, **1998**, 133, 227–231.
- [77] Martin, R. W., Paulson, E. K., and Zilm, K. W. Design of a triple resonance magic angle sample spinning probe for high field solid state nuclear magnetic resonance, *Rev. Sci. Instrum.*, **2003**, 74, 3045–3061.
- [78] Doty, F. D., Kulkarni, J., Turner, C., Entzminger, G., and Bielecki, A. Using a cross-coil to reduce RF heating by an order of magnitude in



- triple-resonance multinuclear MAS at high fields, *J. Magn. Reson.*, **2006**, *182*, 239–253.
- [79] Schaefer, J., and McKay, R. A. Multi-Tuned Single Coil Transmission Line Probe for Nuclear Magnetic Resonance Spectrometer. Patent num. US 5861748A, **1999**.
- [80] Lim, Y. A., and Maas, W. E. NMR probe circuit for generating close frequency resonances. Patent num. EP1555539A3, **2005**; Bruker Analytik GmbH.
- [81] Frydel, J. A., Krzystyniak, M., Pienkowski, D., Pietrzak, M., De Sousa Amadeu, N., Ratajczyk, T., Idzik, K., Gutmann, T., Tietze, D., Voigt, S., Fenn, A., Limbach, H. H., and Buntkowsky, G. Efficient design of multituned transmission line NMR probes: The electrical engineering approach, *Solid State Nucl. Magn. Reson.*, **2011**, *39*, 72–80.
- [82] Scott, F. J., Alaniva, N., Golota, N. C., Sesti, E. L., Saliba, E. P., Price, L. E., Albert, B. J., Chen, P., O'Connor, R. D., and Barnes, A. B. A versatile custom cryostat for dynamic nuclear polarization supports multiple cryogenic magic angle spinning transmission line probes, *J. Magn. Reson.*, **2018**, *297*, 23–32.
- [83] Nelson, F. A. Nuclear magnetic resonance probe apparatus having double tuned coil systems for spectrometers employing an internal reference. Patent num. US 3434043A, **1969**; Varian Medical Systems Inc.
- [84] Stoll, M. E., Vega, A. J., and Vaughan, R. W. Simple single-coil double resonance NMR probe for solid state studies, *Rev. Sci. Instrum.*, **1977**, *48*, 800–803.
- [85] Zhang, X., Sweedler, J., and Webb, A. A Probe Design for the Acquisition of Homonuclear, Heteronuclear, and Inverse Detected NMR Spectra from Multiple Samples, *J. Magn. Reson.*, **2001**, *153*, 254–258.

- [86] Kan, S., Fan, M., and Courtieu, J. A single-coil triple resonance probe for NMR experiments, *Rev. Sci. Instrum.*, **1980**, *51*, 887–890.
- [87] Cross, V. R., Hester, R. K., and Waugh, J. S. Single coil probe with transmission-line tuning for nuclear magnetic double resonance, *Rev. Sci. Instrum.*, **1976**, *47*, 1486–1488.
- [88] Doty, F. D. Balanced multi-tuned high-power broadband coil for NMR. Patent num. US 005162739A, **1992**; Doty Scientific Inc.
- [89] Zhang, Q., Zhang, H., Lakshmi, K., Lee, D., Bradley, C., and Wittebort, R. Double and Triple Resonance Circuits for High-Frequency Probes, *J. Magn. Reson.*, **1998**, *132*, 167–171.
- [90] Zens, A. P. Double tuned circuit for distributed lumped capacitance observe coils. Patent num. US 4833412A, **1989**; Varian Inc.
- [91] Jiang, Y. J., Pugmire, R. J., and Grant, D. M. An efficient double-tuned  $^{13}\text{C}/^1\text{H}$  probe circuit for CP/MAS NMR and its importance in linewidths, *J. Magn. Reson. (1969)*, **1987**, *71*, 485–494.
- [92] Najim, E., and Grivet, J.-P. Efficiency estimation for single-coil, separate-input, double-tuned NMR probes, *J. Magn. Reson. (1969)*, **1991**, *93*, 27–33.
- [93] Tang, P., Chien, W. J., and Harbison, G. S. Double-resonance circuit for nuclear magnetic resonance spectroscopy, *Solid State Nucl. Magn. Reson.*, **1993**, *2*, 343–348.
- [94] Leidich, S., Braun, M., Gessner, T., and Riemer, T. Silicon cylinder spiral coil for nuclear magnetic resonance spectroscopy of nanoliter samples, *Concepts Magn. Reson. Part B Magn. Reson. Eng.*, **2009**, *35*, 121–132.

- 
- [95] Nevzorov, A. A., Milikisiyants, S., Marek, A. N., and Smirnov, A. I. Multi-resonant photonic band-gap/saddle coil DNP probehead for static solid state NMR of microliter volume samples, *J. Magn. Reson.*, **2018**, 297, 113–123.
- [96] Park, S. H., De Angelis, A. A., Nevzorov, A. A., Wu, C. H., and Opella, S. J. Three-Dimensional Structure of the Transmembrane Domain of Vpu from HIV-1 in Aligned Phospholipid Bicelles, *Biophys. J.*, **2006**, 91, 3032–3042.
- [97] Grant, C. V., Wu, C. H., and Opella, S. J. Probes for high field solid-state NMR of lossy biological samples, *J. Magn. Reson.*, **2010**, 204, 180–188.
- [98] Zeiger, H. Sample head for nuclear resonance measurements. Patent num. US 5229724A, **1993**; Bruker Analytik GmbH.
- [99] Zeiger, H. Probehead for nuclear magnetic resonance measurements. Patent num. US 006307371B1, **2001**; Bruker Analytik GmbH.
- [100] Gor'kov, P. L., Chekmenev, E. Y., Fu, R., Hu, J., Cross, T. A., Cotten, M., and Brey, W. W. A large volume flat coil probe for oriented membrane proteins, *J. Magn. Reson.*, **2006**, 181, 9–20.
- [101] Leroy-Willig, A., Bittoun, J., Kan, S., and Gonord, P. A simplified double-tuned  $^{31}\text{P}$ - $^1\text{H}$  circuit for NMR in vivo spectroscopic experiments, *Rev. Sci. Instrum.*, **1990**, 61, 799–801.
- [102] Fiat, D., and Dolinsek, J. Double resonance MRI coil. Patent num. US 8680863B1, **1997**; Florida State University Research Foundation Inc.
- [103] Stringer, J. A., and Drobny, G. P. Methods for the analysis and design of a solid state nuclear magnetic resonance probe, *Rev. Sci. Instrum.*, **1998**, 69, 3384–3391.

- [104] Schnall, M., Subramanian, V. H., Leigh, J., and Chance, B. A new double-tuned probed for concurrent  $^1\text{H}$  and  $^{31}\text{P}$  NMR, *J. Magn. Reson.* (1969), **1985**, 65, 122 – 129.
- [105] Schnall, M. D., Barlow, C., Subramanian, V. H., and Leigh, J. S. Wireless implanted magnetic resonance probes for in vivo NMR, *J. Magn. Reson.* (1969), **1986**, 68, 161–167.
- [106] Schnall, M., Harihara Subramanian, V., and Leigh, J. The application of overcoupled tank circuits to NMR probe design, *J. Magn. Reson.* (1969), **1986**, 67, 129–134.
- [107] Schnall, M. D., Leigh, J. S., and Subramanian, V. H. Multiple tuning NMR probe. Patent num. US 4742304A, **1988**; Varian Inc., University of Pennsylvania.
- [108] Schnall, M. *In-Vivo Magnetic Resonance Spectroscopy I: Probeheads and Radiofrequency Pulses Spectrum Analysis*; Springer Berlin Heidelberg: Berlin, Heidelberg, **1992**; pp. 33–63.
- [109] Kan, S., and Gonord, P. Single-input double-tuned mutually coupled surface coil circuits: An analysis, *Rev. Sci. Instrum.*, **1991**, 62, 2427–2429.
- [110] Tadanki, S., Colon, R. D., Moore, J., and Waddell, K. W. Double tuning a single input probe for heteronuclear NMR spectroscopy at low field, *J. Magn. Reson.*, **2012**, 223, 64–67.
- [111] Otake, Y., Soutome, Y., Hirata, K., Ochi, H., and Bito, Y. Double-tuned Radiofrequency Coil for  $^{19}\text{F}$  and  $^1\text{H}$  Imaging, *Magn. Reson. Med. Sci.*, **2014**, 13, 199–205.
- [112] Haase, J., Curro, N. J., and Slichter, C. P. Double Resonance Probes for Close Frequencies, *J. Magn. Reson.*, **1998**, 135, 273–9.

- [113] Chang, L. H., Chew, W. M., Weinstein, P. R., and James, T. L. A balanced-matched double-tuned probe for in vivo  $^1\text{H}$  and  $^{31}\text{P}$  NMR, *J. Magn. Reson.*, **1987**, 72, 168–172.
- [114] Blum, H., and Schnall, M. D. Multiply-tuned probe for magnetic resonance imaging or spectroscopy. Patent num. US 005243289, **1993**; The Trustees of the University of Pennsylvania.
- [115] Subramanian, V. H., Schnall, M. D., Chance, B., and Leigh, J. In vivo NMR Probes for Multiple Nuclei, *Proc. Int. Soc. Magn. Reson. Med.*, **1985**, 1985, 1122–1123.
- [116] Rodgers, C. T., Clarke, W. T., Snyder, C., Vaughan, J. T., Neubauer, S., and Robson, M. D. Human cardiac  $^{31}\text{P}$  magnetic resonance spectroscopy at 7 tesla, *Magn. Reson. Med.*, **2014**, 72, 304–315.
- [117] Eleff, S. M., Schnall, M. D., Ligetti, L., Osbakken, M., Subramanian, V. H., Chance, B., and Leigh, J. S. Concurrent measurements of cerebral blood flow, sodium, lactate, and high-energy phosphate metabolism using  $^{19}\text{F}$ ,  $^{23}\text{Na}$ ,  $^1\text{H}$ , and  $^{31}\text{P}$  nuclear magnetic resonance spectroscopy, *Magn. Reson. Med.*, **1988**, 7, 412–24.
- [118] Fitzsimmons, J. R., Brooker, H. R., and Beck, B. A transformer-coupled double-resonant probe for NMR imaging and spectroscopy, *Magn. Reson. Med.*, **1987**, 5, 471–7.
- [119] Sunder Rajan, S., Wehrle, J. P., and Glickson, J. D. A novel double-tuned circuit for in Vivo NMR, *J. Magn. Reson. (1969)*, **1987**, 74, 147–154.
- [120] Gonnella, N. C., and Silverman, R. F. Design and construction of a simple double-tuned, single-input surface-coil probe, *J. Magn. Reson. (1969)*, **1989**, 85, 24–34.

- [121] Inukai, M., and Takeda, K. Double-resonance magic angle coil spinning, *J. Magn. Reson.*, **2010**, *202*, 274–278.
- [122] Collins, D. J., Prock, T., and Leach, M. O. A Flexible Dual Resonant  $^1\text{H}/^{19}\text{F}$  RF Coil for In-Vivo Magnetic Resonance Spectroscopy, *Proc. Intl. Soc. Mag. Reson. Med.*, **2000**, *8*, 1417.
- [123] Hu, S., Reimer, J. A., and Bell, A. T. Single-input double-tuned circuit for double resonance nuclear magnetic resonance experiments, *Rev. Sci. Instrum.*, **1998**, *69*, 477–478.
- [124] Mazurkewitz, P., and Leussler, C. Double resonant transmit receive solenoid coil for MRI. Patent num. US 20090160442A1, **2009**; Koninklijke Philips NV.
- [125] Hu, L., Hockett, F. D., Chen, J., Zhang, L., Caruthers, S. D., Lanza, G. M., and Wickline, S. A. A generalized strategy for designing  $^{19}\text{F}/^1\text{H}$  dual-frequency MRI coil for small animal imaging at 4.7 Tesla, *J. Magn. Reson. Imaging*, **2011**, *34*, 245–252.
- [126] Paulson, E. K., Martin, R. W., and Zilm, K. W. Cross polarization, radio frequency field homogeneity, and circuit balancing in high field solid state NMR probes, *J. Magn. Reson.*, **2004**, *171*, 314–323.
- [127] Fitzsimmons, J. R., Brooker, H. R., and Beck, B. A comparison of double-tuned surface coils, *Magn. Reson. Med.*, **1989**, *10*, 302–9.
- [128] Cao, P., Zhang, X., Park, I., Najac, C., Nelson, S. J., Ronen, S., and Larson, P. E.  $^1\text{H}$ - $^{13}\text{C}$  independently tuned radiofrequency surface coil applied for in vivo hyperpolarized MRI, *Magn. Reson. Med.*, **2016**, *76*, 1612–1620.
- [129] Grist, T. M., Jesmanowicz, A., Kneeland, J. B., Froncisz, W., and Hyde, J. S. Doubly tuned local coils for MRI and MRS at 1.5 T, *Magn. Reson. Med.*, **1988**, *6*, 253–264.

- 
- [130] van Hecke, P., Decanniere, C., and Vanstapel, F. Double-tuned resonator designs for NMR spectroscopy, *J. Magn. Reson. (1969)*, **1989**, 84, 170–176.
- [131] Volotovskyy, V., Tomanek, B., Corbin, I., Buist, R., Tuor, U. I., and Peeling, J. Doubly tunable double ring surface coil, *Concepts Magn. Reson. Part B Magn. Reson. Eng.*, **2003**, 17, 11–16.
- [132] Pang, Y., Zhang, X., Xie, Z., Wang, C., and Vigneron, D. B. Common-Mode Differential-Mode (CMDM) Method for Double-Nuclear MR Signal Excitation and Reception at Ultrahigh Fields, *IEEE Trans. Med. Imaging*, **2011**, 30, 1965–1973.
- [133] Lowe, I. J., and Engelsberg, M. A fast recovery pulsed nuclear magnetic resonance sample probe using a delay line, *Rev. Sci. Instrum.*, **1974**, 45, 631–639.
- [134] Lowe, I. J., and Whitson, D. W. Homogeneous RF field delay line probe for pulsed nuclear magnetic resonance, *Rev. Sci. Instrum.*, **1977**, 48, 268–274.
- [135] Kubo, A., and Ichikawa, S. Ultra-broadband NMR probe: numerical and experimental study of transmission line NMR probe, *J. Magn. Reson.*, **2003**, 162, 284–299.
- [136] Scharfetter, H., Petrovic, A., Eggenhofer, H., and Stollberger, R. A no-tune no-match wideband probe for nuclear quadrupole resonance spectroscopy in the VHF range, *Meas. Sci. Technol.*, **2014**, 25, 125501.
- [137] Scott, E., Stettler, J., and Reimer, J. A. Utility of a tuneless plug and play transmission line probe, *J. Magn. Reson.*, **2012**, 221, 117–119.
- [138] Tang, J. A., Wiggins, G. C., Sodickson, D. K., and Jerschow, A. Cutoff-free travelling wave NMR, *Concepts Magn. Reson. Part A*, **2011**, 38A, 253–267.

- [139] Murphree, D., Cahn, S. B., Rahmlow, D., and DeMille, D. An easily constructed, tuning free, ultra-broadband probe for NMR, *J. Magn. Reson.*, **2007**, *188*, 160–167.
- [140] Murphree, J. D. H., DeMille, D. P., and Cahn, S. B. Transmission line probe for NMR. Patent num. US 8164336B1, **2012**.
- [141] Fratila, R. M., Gomez, M. V., Sýkora, S., and Velders, A. H. Multinuclear nanoliter one-dimensional and two-dimensional NMR spectroscopy with a single non-resonant microcoil, *Nat. Commun.*, **2014**, *5*, 3025.
- [142] Velders, A. H., Fratila, R. M., Almagro, M. V. G., and Sýkora, S. Nuclear magnetic resonance (NMR) spectroscopy device. Patent num. US 9733323B2, **2017**; Wageningen Universiteit.
- [143] Stokes, H. T., Case, T. A., Ailion, D. C., and Wang, C. H. NMR observations of molecular motions and Zeeman-quadrupole cross relaxation in 1,2-difluorotetrachloroethane, *J. Chem. Phys.*, **1979**, *70*, 3563.
- [144] Webber, G. D., and Riedi, P. C. Broad band NMR spectrometer for the study of hyperfine fields in ferromagnetic materials, *J. Phys. E: Sci. Instrum.*, **1981**, *14*, 1159–1163.
- [145] Abraham, A., Prins, R., van Bokhoven, J. A., van Eck, E. R. H., and Kentgens, A. P. M. Multinuclear Solid-State High-Resolution and  $^{13}\text{C}$ - $\{^{27}\text{Al}\}$  Double-Resonance Magic-Angle Spinning NMR Studies on Aluminum Alkoxides, *J. Phys. Chem. B*, **2006**, *110*, 6553–6560.
- [146] Mandal, S., and Song, Y. Q. Two-dimensional NQR using ultra-broadband electronics, *J. Magn. Reson.*, **2014**, *240*, 16–23.



- [147] Mandal, S., Utsuzawa, S., and Song, Y. Q. An extremely broadband low-frequency MR system, *Micropor. Mesopor. Mater.*, **2013**, *178*, 53–55.
- [148] Mandal, S., Utsuzawa, S., Cory, D. G., Hürlimann, M., Poitzsch, M., and Song, Y. Q. An ultra-broadband low-frequency magnetic resonance system, *J. Magn. Reson.*, **2014**, *242*, 113–125.
- [149] Spengler, N. Modular  $\mu$ NMR Probe. dissertation, University of Freiburg, **2016**.
- [150] von Harbou, E., Behrens, R., Berje, J., Brächer, A., and Hasse, H. Studying Fast Reaction Kinetics with Online NMR Spectroscopy, *Chemie Ingenieur Technik*, **2017**, *89*, 369–378.
- [151] Friebe, A., Fröscher, A., Münnemann, K., von Harbou, E., and Hasse, H. In situ measurement of liquid-liquid equilibria by medium field nuclear magnetic resonance, *Fluid Phase Equilibria*, **2017**, *438*, 44–52.
- [152] Friebe, A., Von Harbou, E., Münnemann, K., and Hasse, H. Reaction Monitoring by Benchtop NMR Spectroscopy Using a Novel Stationary Flow Reactor Setup, *Industrial and Engineering Chemistry Research*, **2019**, *58*, 18125–18133.
- [153] Dalitz, F., Kreckel, L., Maiwald, M., and Guthausen, G. Quantitative Medium-Resolution NMR Spectroscopy Under Non-Equilibrium Conditions, Studied on the Example of an Esterification Reaction, *Applied Magnetic Resonance*, **2014**, *45*, 411–425.
- [154] Kern, S., Meyer, K., Guhl, S., Gräber, P., Paul, A., King, R., and Maiwald, M. Online low-field NMR spectroscopy for process control of an industrial lithiation reaction-automated data analysis, *Analytical and Bioanalytical Chemistry*, **2018**, *410*, 3349–3360.

- [155] Giraudeau, P., and Felpin, F. X. Flow reactors integrated with in-line monitoring using benchtop NMR spectroscopy, *Reaction Chemistry and Engineering*, **2018**, 3, 399–413.
- [156] Kibrik, É. J., Steinhof, O., Scherr, G., Thiel, W. R., and Hasse, H. On-line NMR spectroscopic reaction kinetic study of urea-formaldehyde resin synthesis, *Industrial and Engineering Chemistry Research*, **2014**, 53, 12602–12613.
- [157] Bernstein, M. A., Štefinović, M., and Sleight, C. J. Optimising reaction performance in the pharmaceutical industry by monitoring with NMR, *Magnetic Resonance in Chemistry*, **2007**, 45, 564–571.
- [158] Do, N. M., Olivier, M. A., Salisbury, J. J., and Wager, C. B. Application of quantitative  $^{19}\text{F}$  and  $^1\text{H}$  NMR for reaction monitoring and in situ yield determinations for an early stage pharmaceutical candidate, *Analytical Chemistry*, **2011**, 83, 8766–8771.
- [159] Yushmanov, P. V., and Furó, I. A rapid-mixing design for conventional NMR probes, *Journal of Magnetic Resonance*, **2005**, 175, 264–270.
- [160] Yue, J., Schouten, J. C., and Alexander Nijhuis, T. Integration of microreactors with spectroscopic detection for online reaction monitoring and catalyst characterization, *Industrial and Engineering Chemistry Research*, **2012**, 51, 14583–14609.
- [161] Harel, E. Lab-on-a-chip detection by magnetic resonance methods, *Progress in Nuclear Magnetic Resonance Spectroscopy*, **2010**, 57, 293–305.
- [162] Brächer, A., Behrens, R., von Harbou, E., and Hasse, H. Application of a new micro-reactor  $^1\text{H}$  NMR probe head for quantitative analysis of fast esterification reactions, *Chemical Engineering Journal*, **2016**, 306, 413–421.

- [163] Brächer, A., Hoch, S., Albert, K., Kost, H. J., Werner, B., Von Harbou, E., and Hasse, H. Thermostatted micro-reactor NMR probe head for monitoring fast reactions, *Journal of Magnetic Resonance*, **2014**, *242*, 155–161.
- [164] Swyer, I., Von der Ecken, S., Wu, B., Jenne, A., Soong, R., Vincent, F., Schmidig, D., Frei, T., Busse, F., Stronks, H. J., Simpson, A. J., and Wheeler, A. R. Digital microfluidics and nuclear magnetic resonance spectroscopy for in situ diffusion measurements and reaction monitoring, *Lab on a Chip*, **2019**, *19*, 641–653.
- [165] Hale, W., Rossetto, G., Greenhalgh, R., Finch, G., and Utz, M. High-resolution nuclear magnetic resonance spectroscopy in microfluidic droplets, *Lab Chip*, **2018**, *18*, 3018–3024.
- [166] Ryan, H., Smith, A., and Utz, M. Structural shimming for high-resolution nuclear magnetic resonance spectroscopy in lab-on-a-chip devices, *Lab on a Chip*, **2014**, *14*, 1678–1685.
- [167] Jia, F., Kumar, R., and Korvink, J. G. Optimal magnetic susceptibility matching in 3D, *Magnetic Resonance in Medicine*, **2013**, *69*, 1146–1156.
- [168] Wu, B., Ecken, S., Swyer, I., Li, C., Jenne, A., Vincent, F., Schmidig, D., Kuehn, T., Beck, A., Busse, F., Stronks, H., Soong, R., Wheeler, A. R., and Simpson, A. Rapid Chemical Reaction Monitoring by Digital Microfluidics-NMR: Proof of Principle Towards an Automated Synthetic Discovery Platform, *Angewandte Chemie Int Ed*, **2019**, *58*, 15372–15376.
- [169] Sorte, E. G., Banek, N. A., Wagner, M. J., Alam, T. M., and Tong, Y. J. In Situ Stripline Electrochemical NMR for Batteries, *ChemElectroChem*, **2018**, *5*, 2336–2340.

- [170] Sorte, E. G., Jilani, S., and Tong, Y. J. Methanol and Ethanol Electrooxidation on PtRu and PtNiCu as Studied by High-Resolution In Situ Electrochemical NMR Spectroscopy with Interdigitated Electrodes, *Electrocatalysis*, **2017**, 8, 95–102.
- [171] Han, O. H., Han, K. S., Shin, C. W., Lee, J., Kim, S.-S., Um, M. S., Joh, H.-I., Kim, S.-K., and Ha, H. Y. Observation of Methanol Behavior in Fuel Cells In Situ by NMR Spectroscopy, *Angewandte Chemie International Edition*, **2012**, 51, 3842–3845.
- [172] Lobo, C. M., Gomes, B. F., Bouzouma, H., Danieli, E., Blümich, B., and Colnago, L. A. Improving in operando low field NMR copper electrodeposition analyses using inductively coupled coils, *Electrochimica Acta*, **2019**, 298, 844–851.
- [173] Richards, J. A., and Evans, D. H. Flow Cell for Electrolysis within the Probe of a Nuclear Magnetic Resonance Spectrometer, *Analytical Chemistry*, **1975**, 47, 964–966.
- [174] da Silva, P., Gomes, B., Lobo, C., Júnior, L., Danieli, E., Carmo, M., Blümich, B., and Colnago, L. Electrochemical NMR spectroscopy: Electrode construction and magnetic sample stirring, *Microchem J*, **2019**, 146, 658–663.
- [175] Tong, Y. J. In situ electrochemical nuclear magnetic resonance spectroscopy for electrocatalysis: Challenges and prospects, *Current Opinion in Electrochemistry*, **2017**, 4, 60–68.
- [176] Bussy, U., and Boujtita, M. Review of advances in coupling electrochemistry and liquid state NMR, *Talanta*, **2015**, 136, 155–160.
- [177] Mairanovsky, V. G., Yusefovich, L. Y., and Filippova, T. M. NMR-electrolysis combined method (NMREL). Basic principles and some applications, *Journal of Magnetic Resonance (1969)*, **1983**, 54, 19–35.

- [178] Felhofer, J. L., Blanes, L., and Garcia, C. D. Recent developments in instrumentation for capillary electrophoresis and microchip-capillary electrophoresis, *ELECTROPHORESIS*, **2010**, *31*, 2469–2486.
- [179] Oosthoek-de Vries, A. J., Nieuwland, P. J., Bart, J., Koch, K., Janssen, J. W. G., van Bentum, P. J. M., Rutjes, F. P. J. T., Gardeniers, H. J. G. E., and Kentgens, A. P. M. Inline Reaction Monitoring of Amine-Catalyzed Acetylation of Benzyl Alcohol Using a Microfluidic Stripline Nuclear Magnetic Resonance Setup, *Journal of the American Chemical Society*, **2019**, *141*, 5369–5380.
- [180] León, L., and Mozo, J. Designing spectroelectrochemical cells: A review, *TrAC Trends in Analytical Chemistry*, **2018**, *102*, 147–169.
- [181] Klod, S., Ziegls, F., and Dunsch, L. In Situ NMR Spectroelectrochemistry of Higher Sensitivity by Large Scale Electrodes, *Analytical Chemistry*, **2009**, *81*, 10262–10267.
- [182] Mincey, D. W., Popovich, M. J., Faustino, P. J., Hurst, M. M., and Caruso, J. A. Monitoring of Electrochemical Reactions by Nuclear Magnetic Resonance Spectrometry, *Analytical Chemistry*, **1990**, *62*, 1197–1200.
- [183] Prenzler, P. D., Bramley, R., Downing, S. R., and Heath, G. A. High-field NMR spectroelectrochemistry of spinning solutions: Simultaneous in situ detection of electrogenerated species in a standard probe under potentiostatic control, *Electrochemistry Communications*, **2000**, *2*, 516–521.
- [184] Albert, K., Dreher, E.-L., Straub, H., and Rieker, A. Monitoring electrochemical reactions by <sup>13</sup>C NMR spectroscopy, *Magnetic Resonance in Chemistry*, **1987**, *25*, 919–922.
- [185] Ni, Z., Cui, X., Cao, S., and Chen, Z. A novel in situ electrochemical NMR cell with a palisade gold film electrode, *Aip Adv*, **2017**, *7*, 085205.

- [186] Webster, R. D. In Situ Electrochemical-NMR Spectroscopy. Reduction of Aromatic Halides, *Analytical Chemistry*, **2004**, *76*, 1603–1610.
- [187] Gomes, B., da Silva, P., Lobo, C., da Santos, M., and Colnago, L. Strong magnetoelectrolysis effect during electrochemical reaction monitored in situ by high-resolution NMR spectroscopy, *Anal Chim Acta*, **2017**, *983*, 91–95.
- [188] Erhardt, J. B., Fuhrer, E., Gruschke, O. G., Leupold, J., Wapler, M. C., Hennig, J., Stieglitz, T., and Korvink, J. G. Should patients with brain implants undergo MRI?, *Journal of Neural Engineering*, **2018**, *15*, 041002.
- [189] Schenck, J. F. The role of magnetic susceptibility in magnetic resonance imaging: MRI magnetic compatibility of the first and second kinds, *Medical Physics*, **1996**, *23*, 815–850.
- [190] Lacey, M. E., Subramanian, R., Olson, D. L., Webb, A. G., and Sweedler, J. V. High-Resolution NMR Spectroscopy of Sample Volumes from 1 nL to 10  $\mu$ L, *Chemical Reviews*, **1999**, *99*, 3133–3152.
- [191] Krojanski, H. G., Lambert, J., Gerikalan, Y., Suter, D., and Hergenröder, R. Microslot NMR Probe for Metabolomics Studies, *Analytical Chemistry*, **2008**, *80*, 8668–8672.
- [192] Patra, B., Sharma, M., Hale, W., and Utz, M. Time-resolved non-invasive metabolomic monitoring of a single cancer spheroid by microfluidic NMR, *Scientific Reports*, **2021**, *11*, 53.
- [193] Jones, C. J., and Larive, C. K. Could smaller really be better? Current and future trends in high-resolution microcoil NMR spectroscopy, *Analytical and Bioanalytical Chemistry*, **2012**, *402*, 61–68.
- [194] Milazzo, G., Caroli, S., and Braun, R. D. Tables of standard electrode potentials, *Journal of The Electrochemical Society*, **1978**, *125*, 261C.

- 
- [195] Bard, A. J., Parsons, R., and Jordan, J. *Standard potentials in aqueous solution*, 1st ed.; Routledge: New York and Basel, **1985**.
- [196] Celozzi, S., Araneo, R., and Lovat, G. *Electromagnetic Shielding*; Wiley Series in Microwave and Optical Engineering; John Wiley & Sons, Inc.: Hoboken, **2008**; pp. 1–358.
- [197] COMSOL, RF Module User's Guide. version COMSOL 5.5, CM021001.
- [198] Wapler, M. C., Leupold, J., Dragonu, I., von Elverfeld, D., Zaitsev, M., and Wallrabe, U. Magnetic properties of materials for MR engineering, micro-MR and beyond, *Journal of Magnetic Resonance*, **2014**, *242*, 233–242.
- [199] COMSOL, AC/DC Module User's Guide. version COMSOL 5.5, CM020104.
- [200] Yu, L., Tay, F. E. H., Xu, G., Chen, B., Avram, M., and Iliescu, C. Adhesive bonding with SU-8 at wafer level for microfluidic devices, *Journal of Physics: Conference Series*, **2006**, *34*, 776–781.
- [201] Bruker BioSpin MRI GmbH, ParaVision 360 User Manual. version 001, Document Number: 9007199893001739.
- [202] Gruschke, O. Receive-only Micro Phased Coil Array for Magnetic Resonance. dissertation, University of Freiburg, **2013**.
- [203] Nordin, N., Bordonali, L., Badilita, V., and MacKinnon, N. Spatial and Temporal Control Over Multilayer Bio-Polymer Film Assembly and Composition, *Macromolecular Bioscience*, **2019**, *19*, 1800372.
- [204] Liu, Y., Kim, E., Ghodssi, R., Rubloff, G. W., Culver, J. N., Bentley, W. E., and Payne, G. F. Biofabrication to build the biology–device interface, *Biofabrication*, **2010**, *2*, 022002.

- [205] Geng, Z., Wang, X., Guo, X., Zhang, Z., Chen, Y., and Wang, Y. Electrodeposition of chitosan based on coordination with metal ions in situ-generated by electrochemical oxidation, *Journal of Materials Chemistry B*, **2016**, *4*, 3331–3338.
- [206] Hoell, I. A., Vaaje-Kolstad, G., and Eijsink, V. G. Structure and function of enzymes acting on chitin and chitosan, *Biotechnology and Genetic Engineering Reviews*, **2010**, *27*, 331–366.
- [207] Wang, Y., Liu, Y., Cheng, Y., Kim, E., Rubloff, G. W., Bentley, W. E., and Payne, G. F. Coupling Electrodeposition with Layer-by-Layer Assembly to Address Proteins within Microfluidic Channels, *Advanced Materials*, **2011**, *23*, 5817–5821.
- [208] Yan, K., Ding, F., Bentley, W. E., Deng, H., Du, Y., Payne, G. F., and Shi, X.-W. Coding for hydrogel organization through signal guided self-assembly, *Soft Matter*, **2014**, *10*, 465–469.
- [209] da S. Pinto, T., Alves, L. A., de Azevedo Cardozo, G., Munhoz, V. H., Verly, R. M., Pereira, F. V., and de Mesquita, J. P. Layer-by-layer self-assembly for carbon dots/chitosan-based multilayer: Morphology, thickness and molecular interactions, *Materials Chemistry and Physics*, **2017**, *186*, 81 – 89.
- [210] Cheng, Y., Luo, X., Betz, J., Buckhout-White, S., Bekdash, O., Payne, G. F., Bentley, W. E., and Rubloff, G. W. In situ quantitative visualization and characterization of chitosan electrodeposition with paired sidewall electrodes, *Soft Matter*, **2010**, *6*, 3177–3183.
- [211] Nordin, N. Development of a microfluidic platform for NMR analysis of biological samples. dissertation, Karlsruhe Institute of Technology (KIT), **2020**.
- [212] Wheeler, H. Simple Inductance Formulas for Radio Coils, *Proceedings of the IRE*, **1928**, *16*, 1398–1400.



- 
- [213] Fuhrer, E. Advanced interfaces for biomedical engineering applications in high- and low field NMR/MRI. dissertation, Karlsruhe Institute of Technology (KIT), **2019**.
- [214] Smith, P., Donovan, K., Szekely, O., Baias, M., and Frydman, L. Ultrafast NMR T1 relaxation measurements: Probing molecular properties in real time, *ChemPhysChem*, **2013**, *14*, 3138–3145.
- [215] Swyer, I., Soong, R., Dryden, M. D., Fey, M., Maas, W. E., Simpson, A., and Wheeler, A. R. Interfacing digital microfluidics with high-field nuclear magnetic resonance spectroscopy, *Lab on a Chip*, **2016**, *16*, 4424–4435.
- [216] Boero, G., Frounchi, J., Furrer, B., Besse, P.-A., and Popovic, R. S. Fully integrated probe for proton nuclear magnetic resonance magnetometry, *Rev. Sci. Instrum.*, **2001**, *72*, 2764–2768.
- [217] Anders, J., Chiaramonte, G., SanGiorgio, P., and Boero, G. A single-chip array of NMR receivers, *J. Magn. Reson.*, **2009**, *201*, 239–249.
- [218] Jouda, M., Gruschke, O. G., and Korvink, J. G. A new fully integrated multichannel receiver design for magnetic resonance imaging, *Concepts Magn. Reson. Part B Magn. Reson. Eng.*, **2016**, *46B*, 134–145.
- [219] Grisi, M., Gualco, G., and Boero, G. A broadband single-chip transceiver for multi-nuclear NMR probes, *Rev. Sci. Instrum.*, **2015**, *86*, 044703.
- [220] Kamberger, R., Moazenzadeh, A., Korvink, J. G., and Gruschke, O. G. Hollow microcoils made possible with external support structures manufactured with a two-solvent process, *J. Micromech. Microeng.*, **2016**, *26*, 065002.
- [221] Gomez, M. V., Juan, A., Jimenez-Marquez, F., de la Hoz, A., and Velders, A. H. Illumination of Nanoliter-NMR Spectroscopy Chips for

- Real-Time Photochemical Reaction Monitoring, *Analytical Chemistry*, **2018**, *90*, 1542–1546.
- [222] Schoenmaker, J., Pirota, K. R., and Teixeira, J. C. Magnetic flux amplification by Lenz lenses, *Review of Scientific Instruments*, **2013**, *84*, 085120.
- [223] Fedorov, A., Beichel, R., Kalpathy-Cramer, J., Finet, J., Fillion-Robin, J.-C., Pujol, S., Bauer, C., Jennings, D., Fennessy, F., Sonka, M., Buatti, J., Aylward, S., Miller, J. V., Pieper, S., and Kikinis, R. 3D Slicer as an image computing platform for the Quantitative Imaging Network, *Magnetic Resonance Imaging*, **2012**, *30*, 1323 – 1341, Quantitative Imaging in Cancer.

## Publications

- [HD1] **Davoodi, H.**, Jouda, M., Korvink, J. G., MacKinnon, N., and Badilita, V. Broadband and multi-resonant sensors for NMR, *Progress in Nuclear Magnetic Resonance Spectroscopy*, **2019**, *112-113*, 34–54.
- [HD2] **Davoodi, H.**, Nordin, N., Bordonali, L., Korvink, J. G., MacKinnon, N., and Badilita, V. An NMR-compatible microfluidic platform enabling in situ electrochemistry, *Lab on a Chip*, **2020**, *20*, 3202–3212.
- [HD3] **Davoodi, H.**, Nordin, N., Korvink, J. G., MacKinnon, N., and Badilita, V. Untuned broadband spiral micro-coils achieve sensitive multi-nuclear NMR TX/RX from microfluidic samples, *Scientific Reports*, **2021**, *11*, 7798.
- [HD4] **Davoodi, H.**, Badilita, V., and Korvink, J. Broadband NMR stripline. European Patent, **2020**; filed.
- [HD5] Nordin, N., Bordonali, L., **Davoodi, H.**, Ratnawati, N. D., Gygli, G., Korvink, J. G., Badilita, V., and MacKinnon, N. Real-Time NMR Monitoring of Spatially Segregated Enzymatic Reactions in Multilayered Hydrogel Assemblies, *Angewandte Chemie International Edition*, **2021**, *60*, 19176–19182.
- [HD6] Beyaz, M., Baelhadj, H., Habibiabad, S., Adhikari, S., **Davoodi, H.**, and Badilita, V. A non-resonant kinetic energy harvester for bioimplantable applications, *Micromachines*, **2018**, *9*.

- [HD7] Baelhadj, H. C., Adhikari, S. S., **Davoodi, H.**, Badilita, V., and Beyaz, M. İ. A sub-cm<sup>3</sup> energy harvester for in-vivo biosensors, *Microelectronic Engineering*, **2020**, 226, 111288.
- [HD8] Toto, S., Jouda, M., Korvink, J. G., Sundarayyan, S., Voigt, A., **Davoodi, H.**, and Brandner, J. J. Characterization of a wireless vacuum sensor prototype based on the SAW-Pirani principle, *Processes*, **2020**, 8, 1685.

## List of Figures

2.1	Gyromagnetic ratios of different NMR active isotopes . . . . .	9
2.2	Nuclei spin and relaxation . . . . .	10
2.3	NMR signal processing chain . . . . .	16
2.4	Flash pulse sequence . . . . .	17
2.5	Different micro-coil geometries . . . . .	24
2.6	Multinuclear NMR topologies employing a single coil . . . . .	27
2.7	Multiresonant networks employing a single coil . . . . .	28
2.8	Trap circuit characteristics . . . . .	29
2.9	Tank circuit characteristics . . . . .	33
2.10	Trap topologies . . . . .	35
2.11	Tank topologies . . . . .	39
2.12	Miscellaneous topologies to realise multinuclear NMR . . . . .	41
2.13	Broadband NMR coils . . . . .	44
2.14	Multinuclear NMR probes reported in the literature . . . . .	46
3.1	Experimental setup for <i>in situ</i> electrochemistry experiments . . . . .	53
3.2	Simulated static field distortions introduced by nano-layers . . . . .	62
3.3	Simulation results of different electrode geometries . . . . .	63
3.4	Disk electrode evaluation employing RF simulations . . . . .	64
3.5	Simulated NMR spectra and nutation signals for different electrode geometries . . . . .	69
3.6	Fabrication process of <i>in situ</i> electrochemistry inserts . . . . .	72
3.7	Electrode geometries in electrochemistry inserts . . . . .	75
3.8	NMR measurements employing different inserts . . . . .	79
3.9	MRI results employing different inserts . . . . .	82

---

3.10	<i>in situ</i> monitoring of CS deposition . . . . .	86
3.11	Multiplex enzyme reactions monitored with NMR . . . . .	89
4.1	Multiresonant micro-coils . . . . .	96
4.2	Experimental setup for broadband NMR . . . . .	97
4.3	$B_1$ field distribution of the broadband coil . . . . .	105
4.4	Electrical characteristics of the broadband coil . . . . .	106
4.5	Simulated figures of merit of broadband coil . . . . .	108
4.6	$B_0$ map and NMR spectra of the broadband detector . . . . .	111
4.7	Fabrication process of the broadband detector . . . . .	113
4.8	Fabrication results of the broadband detector . . . . .	116
4.9	Bench-top evaluation of the broadband coils . . . . .	118
4.10	MRI experiments with the broadband detector . . . . .	119
4.11	NMR experiments with the broadband detector and the aqueous sample . . . . .	126
4.12	NMR experiments with the broadband detector and the battery electrolyte sample . . . . .	127
5.1	Experimental setup for the broadband stripline adaptor . . . . .	135
5.2	Different Lenz lens structures reported in the literature . . . . .	136
5.3	Flux distribution of the broadband stripline adaptor . . . . .	137
5.4	$B_0$ and $B_1$ distribution of the broadband stripline adaptor with different $h$ and $w$ . . . . .	140
5.5	Figures of merit of the broadband stripline adaptor with different geometries . . . . .	141
5.6	Fine adjustments of the broadband stripline adaptor geometry . . . . .	143
5.7	Test configuration of the broadband stripline adaptor . . . . .	145
5.8	Reconstructed 3D image of the sensitive volume . . . . .	147
A1	Electrochemistry-NMR inserts technical drawing . . . . .	193
A2	Broadband detector technical drawing . . . . .	194
A3	$B_1$ distribution for different electrode geometries . . . . .	200
A4	$B_1$ distribution broadband spiral coil . . . . .	201
A5	Benchmarking experiments for $^{11}\text{B}$ . . . . .	203

## List of Tables

2.1	Trap circuit configurations . . . . .	32
3.1	Electrode geometries for <i>in situ</i> electrochemistry experiments . . .	59
3.2	Simulated NMR figures of merits for different electrodes . . . . .	70
3.3	Experimental characterisation of the nano-layers . . . . .	77
4.1	Optimised figures of merit for different configurations . . . . .	109
4.2	Summary of NMR experiments using broadband detector . . . . .	129
5.1	Figures of merit of the broadband stripline Lenz lens . . . . .	143
A1	Material properties employed for COMSOL simulations. . . . .	189





# Appendix

## A1 Material properties

**Table A1:** Material properties employed for COMSOL simulations.

Material	$\chi$ (ppm)	$\epsilon_r$ (-)	$\sigma$ (S/m)	ref.
Air	0	1	0	[189]
Glass (BF33)	-11.059	4.6	$1 \times 10^{-6}$	[198], <a href="http://www.schott.com">www.schott.com</a>
Water	-9.035	80	$5.5 \times 10^{-6}$	[198]
SU-8	-9.735	3	$3 \times 10^{-6}$	[198]
Gold	-34	1	$4.1 \times 10^7$	[189], COMSOL library
Copper	-9.63	1	$6.0 \times 10^7$	[189], COMSOL library
FR4 PCB	-3.745	4.6	$4 \times 10^{-4}$	[198], COMSOL library
Membrane (RTV 615)	8.035	2.7	$55 \times 10^{-9}$	[198], <a href="http://www.momentive.com">www.momentive.com</a>

## A2 Fabrication process details

### Plasma cleaning

Pressure: 10 mTorr, Power: 120 W, O<sub>2</sub> flow rate: 50 sccm.

### Modified plasma cleaning

Pressure: 100 mTorr, Bias: -170 V, O<sub>2</sub> flow rate: 50 sccm.

### Spincoat SU-8 3005 for 5 μm height

---

Duration (sec)	Acceleration (rpm/sec)	Speed (rpm)
10	100	500
60	1000	3000
10	500	0

---

### Spincoat SU-8 3025 for 20 μm height

---

Duration (sec)	Acceleration (rpm/sec)	Speed (rpm)
10	100	500
60	1000	4000
10	500	0

---

### Spincoat SU-8 3025 for 25 μm height

---

Duration (sec)	Acceleration (rpm/sec)	Speed (rpm)
10	100	500
60	1000	3000
10	500	0

---

**Spincoat SU-8 3025 for 70  $\mu\text{m}$  height**

Duration (sec)	Acceleration (rpm/ sec)	Speed (rpm)
30	100	500
60	100	0
60	300	1200
60	100	0

**Spincoat SU-8 3025 for 90  $\mu\text{m}$  height**

Duration (sec)	Acceleration (rpm/ sec)	Speed (rpm)
30	100	500
60	100	0
60	300	1000
60	100	0

**Softbake 5  $\mu\text{m}$ -thick SU-8 3005 as adhesive medium**

Raise time (min)	Temperature ( $^{\circ}\text{C}$ )	Stall time (min)
1	95	4.5
5	22	-

**Softbake 70  $\mu\text{m}$ -thick SU-8 3025**

Raise time (min)	Temperature ( $^{\circ}\text{C}$ )	Stall time (min)
30	75	60
30	95	70
330	22	-

**Softbake 90  $\mu\text{m}$ -thick SU-8 3025**

Raise time (min)	Temperature ( $^{\circ}\text{C}$ )	Stall time (min)
30	75	60
30	95	90
360	22	-

**Post exposure bake 70  $\mu\text{m}$ -thick SU-8 3025**

Raise time (min)	Temperature ( $^{\circ}\text{C}$ )	Stall time (min)
30	65	20
120	22	-

**Post exposure bake 90  $\mu\text{m}$ -thick SU-8 3025**

Raise time (min)	Temperature ( $^{\circ}\text{C}$ )	Stall time (min)
30	65	30
120	22	-

**Gold electrodeposition**

Duty cycle: 33 % , Frequency: 0.67 Hz, Current density:  $3 \text{ mA mm}^{-2}$ ,  
Deposition rate: 52.1 nm/ min.

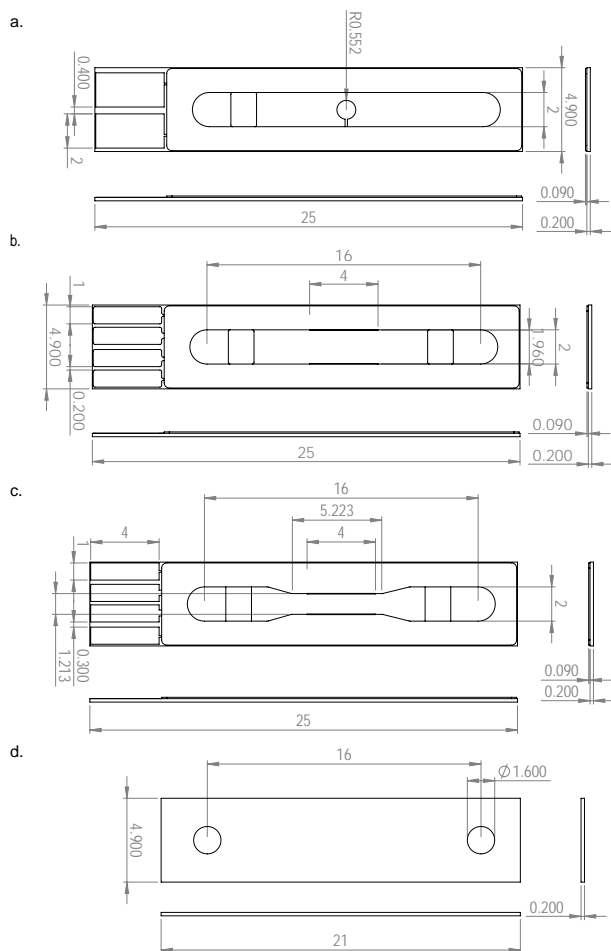
**O<sub>2</sub>-Plasma stripping**

Pressure: 10 mTorr, Power: 1200 W, Temperature: 22  $^{\circ}\text{C}$ , N<sub>2</sub> flow rate:  
70 sccm, CF<sub>4</sub> flow rate: 70 sccm, Frequency: 2.45 GHz.

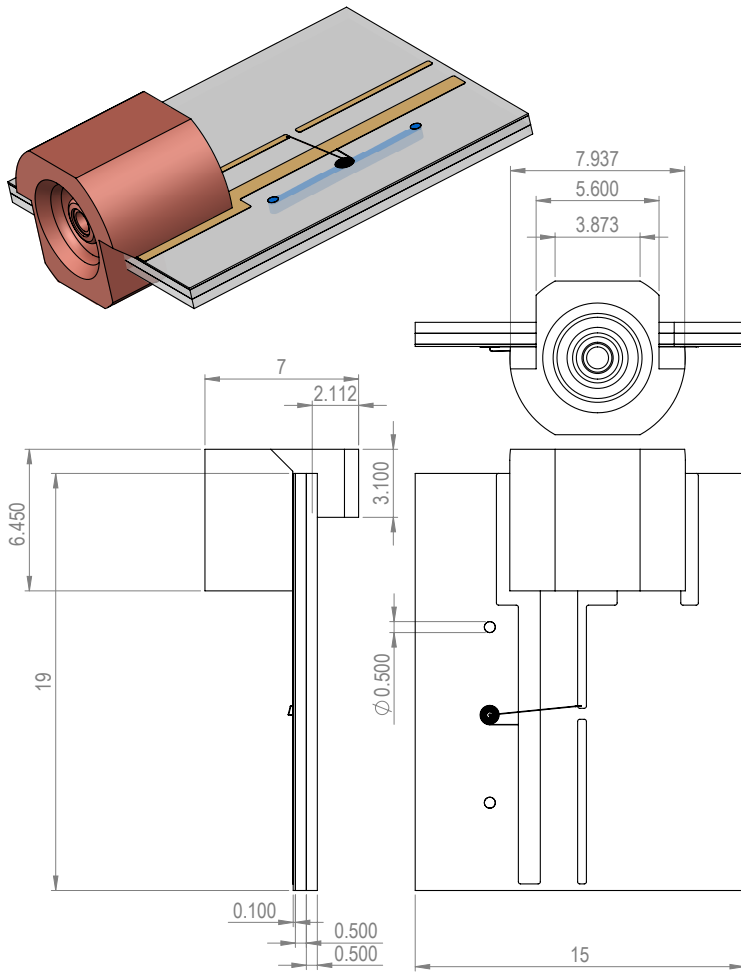
**Wafer bonding**

Temperature: 55  $^{\circ}\text{C}$ , Force: 5 kN, Duration: 300 min, Cool down duration:  
300 min.

## A3 Technical drawings



**Figure A1:** Different insert geometries employed for *in situ* electrochemistry experiments. a. Planar electrode. b. Wide channel sidewall electrode. c. Narrow channel sidewall electrode. d. The top glass layer which seals different inserts. The top layer is bounded to each individual insert however for the illustration purposes, it has been shown separately. Dimensions are in mm.



**Figure A2:** Broadband detector chip. Dimensions are in mm.

## A4 Matlab codes

An exemplary Matlab code to generate the digital twins of NMR signals and calculate the figures of merit

```

1 clear all;
2 clc
3
4 % GUI: ask for user's input
5 prompt = {'Frequency (MHz):', 'Power (W)', '
           Spectral resolution (ppb)', 'with (1) or
           without (2) MSL?', 'Strip width (um)', '
           Channel height (um)'};
6 dlg_title = 'Input';
7 num_lines = 1;
8 defaultans = {'500', '1', '1', '1', '200', '230'};
9 ans = inputdlg(prompt, dlg_title, num_lines,
                defaultans);
10
11 LarmorFreq=str2num(ans{1})*1e6;
12 P=str2num(ans{2});
13 spec_resolution=str2num(ans{3})*1e-9;
14 w=str2num(ans{4});
15 l=str2num(ans{5});
16 h=6e-10/(w*1);
17
18 B00=11.74;
19
20 % Constructing the nutation signal
21 t=(7/scale)*[0:0.3e-6:150e-6];
22 nut_signal(:,1)=t';
23 NMRspectra=[-10:spec_resolution*1e6:10]';

```

```
24
25
26 %   Setting the sampling datapoints
27 stepsize=10e-6;
28 x00=stepsize:stepsize:0.9*w/2;
29 x0=[-fliplr(x00),0,x00];
30 y00=stepsize:stepsize:0.9*l/2;
31 y0=[-fliplr(y00),0,y00];
32 z00=stepsize:stepsize:0.9*h/2;
33 z0=[-fliplr(z00),0,z00];
34
35 [x,y,z]=meshgrid(x0,y0,z0);
36
37 sample=[x(:),y(:),z(:)]';
38
39 %   GUI: Read B1 simulation file and import data
40 %   B1 field simulations performed for 1A current
    applied to the coil
41 [file] = uigetfile({'*.mph'},'Select a simulation
    file for B1');
42 model_B1=mphopen(file);
43 B1 = mphinterp(model_B1,'abs(sqrt((emw.Bx)^2+(emw.
    By)^2))','coord',sample)';
44 impedance = mphglobal(model_B1,'emw.Zport_1');
45 I= sqrt(P/real(impedance));
46
47 %   GUI: Read B0 simulation file and import data
48 [file] = uigetfile({'*.mph'},'Select a simulation
    file for B0');
49 model_B0=mphopen(file0);
```



```

50 B0 = 1/B00*round(1/spec_resolution*abs((mphinterp(
    model_B0, 'mfnc.Bz', 'coord', sample)')))*
    spec_resolution; % normalised to B00
51
52 % Generate the nuttion curve
53 theta=B1*t*I_inuse*gamma;
54 nut_sig=B1'*sin(2*pi*theta);
55 nut_signal(:,i+1)=nut_sig';
56
57 % Generate the NMR spectrum
58 tau=nut_signal(find(nut_signal(:,i+1)==max(
    nut_signal(:,i+1))),1);
59 weight= B1.*sin(2*pi*B1*tau*I_inuse*gamma);
    %amplitude of signal from each voxel
    at 90degree flip angel
60 subs=round(1/spec_resolution*(B0-min(B0))+1);
    % generate bins for spectrum
61 bins=round(1/spec_resolution*(max(B0)-min(B0))+1);
62 histw = accumarray(subs,weight,[bins,1]);
    %signal intensity considering B1 homogeneity
    as a function of B0
63 xx=(min(B0)+[1:bins]*spec_resolution)*1e6;
    %ppm
64 xx= xx-xx(find(histw==max(histw))); % adjust
    the chimacal shift
65
66
67 lowerband=[-10:spec_resolution*1e6:min(xx)];
68 upperband=[max(xx)+spec_resolution*1e6:
    spec_resolution*1e6:10+2*spec_resolution];

```

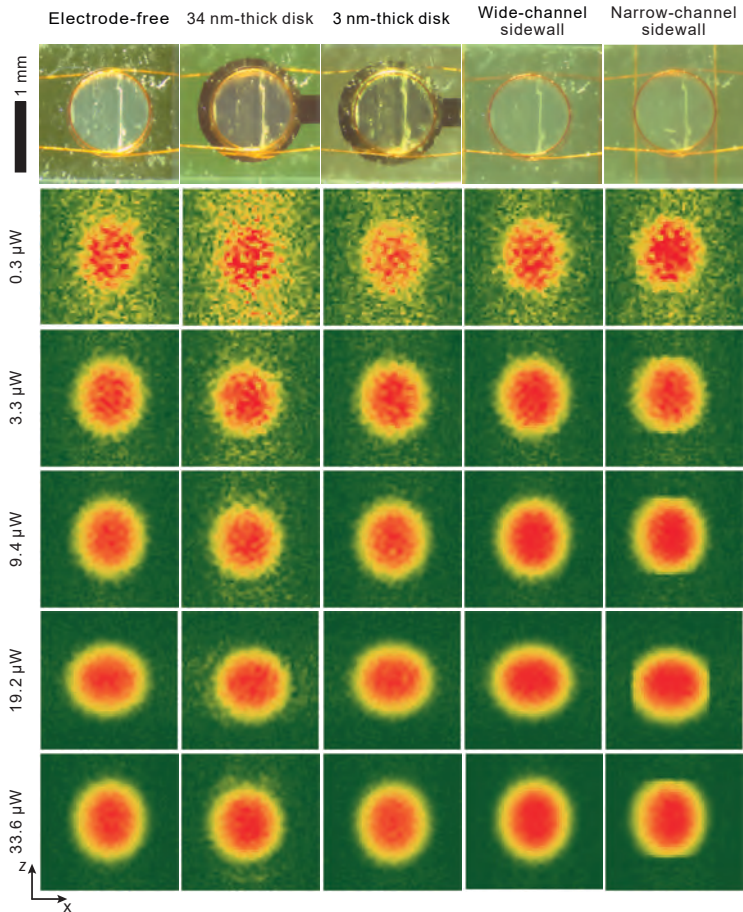
```

69 NMRspectrum=[lowerband , xx , upperband ; 0*
    lowerband , histw ' , 0*upperband ] ' ;
70 NMRspectra (: , i+1)=NMRspectrum (1 : round (20/(
    spec_resolution * 1e6)+1) , 2) ;
71
72 %plot data
73 subplot (2 , 1 , 1) , plot (nut_signal (: , 1) , nut_signal
    (: , 2))
74 hold on
75 subplot (2 , 1 , 2) , plot (NMRspectra (: , 1) , NMRspectra
    (: , 2))
76
77 %% FoM
78 Blu=mean (B1) ;           % ave(B1) per unit applied
    current
79 F=10^(1/10) ;           % Amplifier noise figure
80 V_FID=max (nut_signal (: , 2:3)) ;
81 etta=V_FID ./ sqrt (F * real (Z)) ; %sensitivity
82
83 [ iii , i90m]=max (nut_signal (: , 2:3)) ;
84 Tm=t (i90m) ;           % 90degree pulse
    length
85 exc_eff=pi / 2 / Tm ;           % excitation efficiency
86
87 [ iiii , i450m]=max (nut_signal (3 * i90m : 5 * i90m , 2)) ;
88 B1_hom(i)= iiii / iii ;     % B1 homogeneity
89 SS=max (nut_signal (: , 2:3)) ./ max (NMRspectra (: , 2:3)) ;
    % spectral sharpness
90 Output=[w , l , h , real (Z) ' , Blu ' , etta ' , Tm ' ,
    exc_eff ' , B1_hom ' , SS ' ] ;
91

```

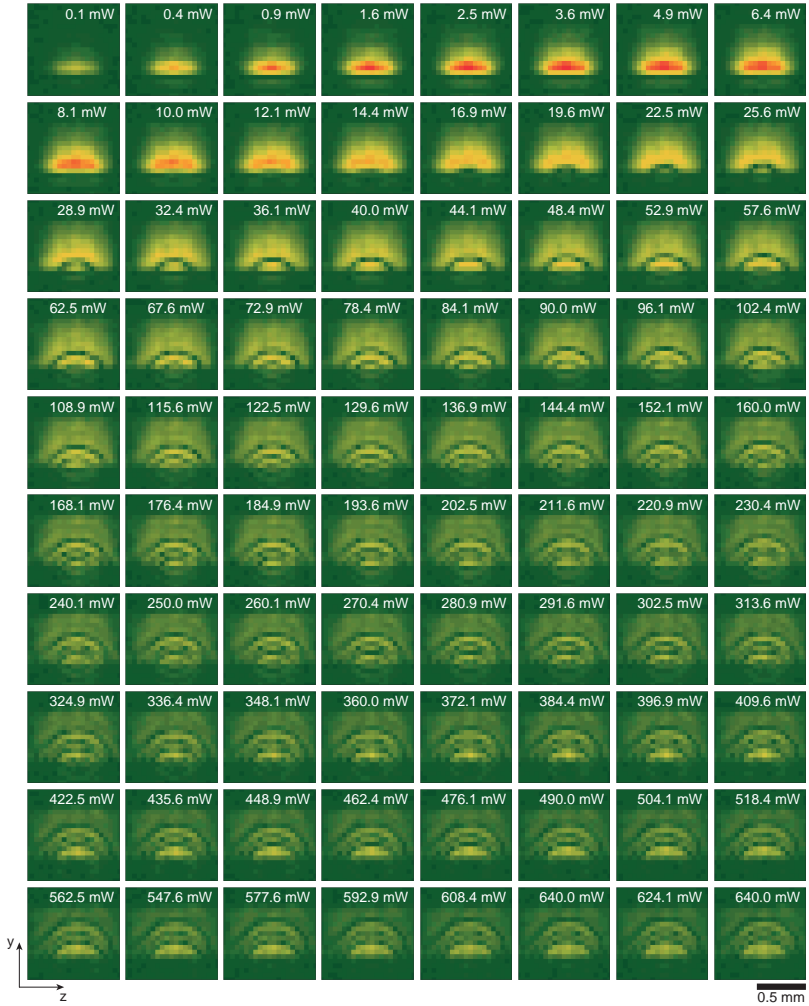
```
92 % Export data
93 [FileName, PathName, FilterIndex] = uiputfile('*' ,
    'Save data as:');
94 if ~ischar(FileName)
95     disp('User aborted the dialog! Data are NOT
    exported. ');
96 else
97     exportfilename = strcat(FileName, '_NutSignal.
    txt');
98     File= fullfile(PathName, exportfilename);
99     dlmwrite(File, nut_signal, 'delimiter', '\t', '
    precision', 6)
100
101     exportfilename = strcat(FileName, '_NMRspectra.
    txt');
102     File= fullfile(PathName, exportfilename);
103     dlmwrite(File, NMRspectra, 'delimiter', '\t', '
    precision', 6)
104
105     exportfilename = strcat(FileName, '_FoM.txt');
106     File= fullfile(PathName, exportfilename);
107     dlmwrite(File, Output, 'delimiter', '\t', '
    precision', 5)
108
109     disp(strcat('Data are exported as:', {' '},
    FileName, '_NutSignal.txt and', {' '}, FileName,
    '_NMRspectrum.txt. They can be found in:', {'
    ' }, PathName));
110 end
```

## A5 RF field distribution for different electrode geometries



**Figure A3:**  $B_1$  map at the sample volume and for different flip angles. The figure is reproduced from [HD2]

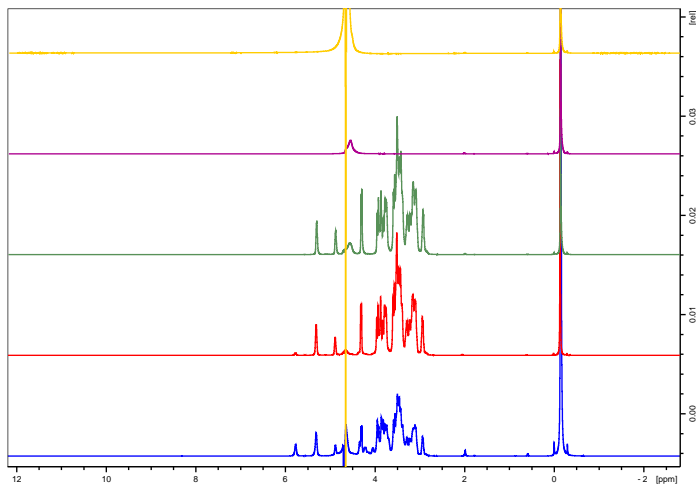
## A6 RF field distribution of the broadband spiral coil



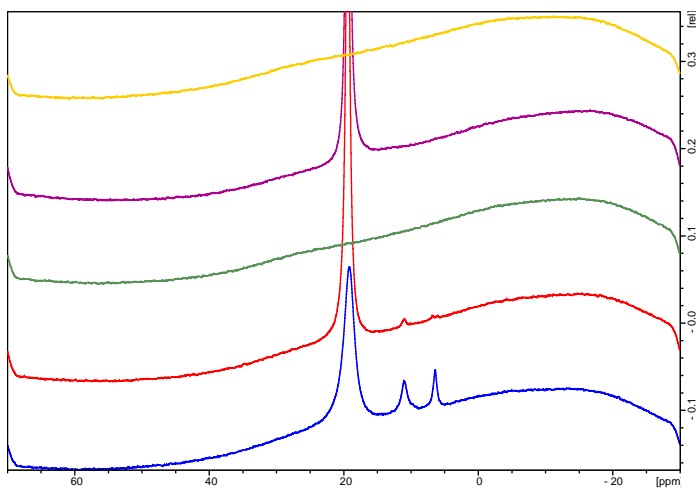
**Figure A4:**  $B_1$  field distribution generated by the broadband spiral coil with different applied power at 500 MHz.

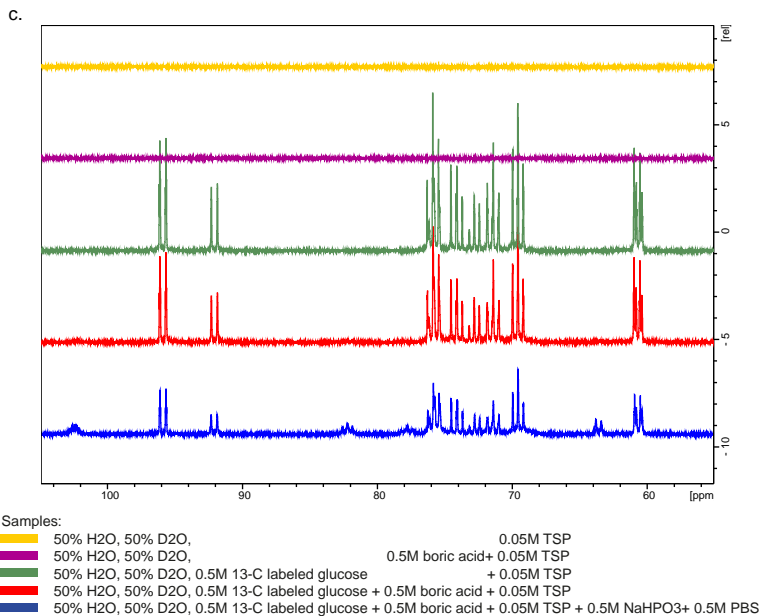
## A7 Benchmarking experiments on borate-glucose complex

a.



b.





**Figure A5:** Benchmarking experiments reveal a reaction between boric acid and glucose in the presence of the buffer at three different frequencies ( corresponding to  $^1\text{H}$ : a,  $^{11}\text{B}$ : b, and  $^{13}\text{C}$ : c). The experiments were performed with different samples and in a 9.4 T superconductive magnet (Bruker Avance III HD spectrometer, 1H/19F,X BBI.). As a result,  $^{11}\text{B}$  has three individual peaks. Accordingly, new peaks appeared in both  $^1\text{H}$  and  $^{13}\text{C}$  spectra and the amplitude of the glucose peaks is reduced. The broad background signal in  $^{11}\text{B}$  stems from the boron content in the glass capillary.





## Acknowledgement

I would like to express my gratitude and appreciation to my supervisor, Prof. Dr. Jan Korvink. His continuous guidance, invaluable advice, and overall insights in this field have made this journey a wonderful experience for me.

I am deeply grateful to my group leader, Dr. Vlad Badilita, for his dedicated support and guidance. He was always willing and enthusiastic to help throughout the research project, as well as professional and personal life. In the same manner, I would like to express my best gratitude to Dr. Neil MacKinnon. I learnt a lot from him. Neil has been a great help to me through these years.

I am also pleased to say thank you to Prof. Andrew G. Webb for being my examiner. His research and publications were always sources of inspiration to me. It was a great pleasure to have him in the examination committee.

I would thank Dr. Nurdiana Nordin for the nice team-work. Diana was always my first reference when facing a chemistry issue. I was lucky to share the office with Shyam Adhikari and Mohammad Abdo and, later, Albina Julius. I would always remember the fun-time we spent together. Shyam was my tutor for cleanroom fabrication. I would never forget his support.

It was a pleasure to spend time with all group members in a professional yet friendly environment. Special thanks to Dr. Mazin Jouda, Dr. Lorenzo Bordonali, Prof. Dr. Jürgen Brandner, Sofia Toto, Emil Mamleyev, Dr. Erwin Fuhrer, Omar Nassar, Mehrdad Alinaghian, Sagar Wadhwa, Pedro Silva, Andrea Rivera, and Julia Schulte-Hermann. I also acknowledge Dr. Ali Moazenzadeh for his patience and support with the wirebonder.

I also appreciate all the help from IMT cleanroom team. Dr. Uwe Köhler, Mrs. Heike Fornasier, Mrs. Barbara Matthis, Mr. Marco Heiler, Mr. Marc Schneider,

and Dr. Richard Thelen were incredible help during fabrication. I am also thankful to Achim Voigt for his supports.

I would like to recognise the assistance that the master students, guest researchers, and HiWis provided. Raji G. Haddad, Atiqur Rahman, Jianyi Liang, and Yin-Kuang Yang helped me with simulation, fabrication, and measurements.

Dr. Herrade Weis was very supportive during the patent procedure. I would appreciate her efforts and time. I would like to offer a special thank to Dr. Claudia Muhle-Goll who helped with the bench-marking NMR experiments.

I would also thank all the external collaborators with whom I could accomplish multiple projects. Prof. Hirokazu Munakata from Tokyo Metropolitan University, and Prof. Mustafa İlker Beyaz and Mr. Hacene C. Baelhadja from Antalya Bilim University.

This PhD work was funded by DFG (Deutsche Forschungsgemeinschaft) through the Bio-PRICE project (DFG BA 4275/4-1) and using several infrastructures from Karlsruhe Nano Micro Facility (KNMF). I highly appreciate both institutions. I also acknowledge Karlsruhe Institute of Technology (KIT) and Institute of Microstructure Technology (IMT) for their continued support. I would also like to say a heartfelt thank you to my mom, dad, and siblings, as well as my wife's family. It was their prayers and blessing that made it possible. Most importantly, I wish to thank my loving and supportive wife, Sevda. She provided unending supports through all ups and downs during these years. It was her who gave me the courage to embark on this journey in the first place. I am indebted to her.





- Band 1** Georg Obermaier  
Research-to-Business Beziehungen: Technologietransfer  
durch Kommunikation von Werten (Barrieren, Erfolgs-  
faktoren und Strategien).  
ISBN 978-3-86644-448-5
- Band 2** Thomas Grund  
Entwicklung von Kunststoff-Mikroventilen im  
Batch-Verfahren.  
ISBN 978-3-86644-496-6
- Band 3** Sven Schüle  
Modular adaptive mikrooptische Systeme in Kombination  
mit Mikroaktoren.  
ISBN 978-3-86644-529-1
- Band 4** Markus Simon  
Röntgenlinsen mit großer Apertur.  
ISBN 978-3-86644-530-7
- Band 5** K. Phillip Schierjott  
Miniaturisierte Kapillarelektrophorese zur kontinuierlichen  
Überwachung von Kationen und Anionen in Prozess-  
strömen.  
ISBN 978-3-86644-523-9
- Band 6** Stephanie Kißling  
Chemische und elektrochemische Methoden zur  
Oberflächenbearbeitung von galvanogeformten  
Nickel-Mikrostrukturen.  
ISBN 978-3-86644-548-2

- Band 7**    **Friederike J. Gruhl**  
Oberflächenmodifikation von Surface Acoustic Wave (SAW)  
Biosensoren für biomedizinische Anwendungen.  
ISBN 978-3-86644-543-7
- Band 8**    **Laura Zimmermann**  
Dreidimensional nanostrukturierte und superhydrophobe  
mikrofluidische Systeme zur Tröpfchengenerierung und  
-handhabung.  
ISBN 978-3-86644-634-2
- Band 9**    **Martina Reinhardt**  
Funktionalisierte, polymere Mikrostrukturen für die  
dreidimensionale Zellkultur.  
ISBN 978-3-86644-616-8
- Band 10**   **Mauno Schelb**  
Integrierte Sensoren mit photonischen Kristallen auf  
Polymerbasis.  
ISBN 978-3-86644-813-1
- Band 11**   **Daniel Auernhammer**  
Integrierte Lagesensorik für ein adaptives mikrooptisches  
Ablensystem.  
ISBN 978-3-86644-829-2
- Band 12**   **Nils Z. Danckwardt**  
Pumpfreier Magnetpartikeltransport in einem  
Mikroreaktionssystem: Konzeption, Simulation  
und Machbarkeitsnachweis.  
ISBN 978-3-86644-846-9
- Band 13**   **Alexander Kolew**  
Heißprägen von Verbundfolien für mikrofluidische  
Anwendungen.  
ISBN 978-3-86644-888-9

- Band 14 Marko Brammer**  
Modulare Optoelektronische Mikrofluidische  
Backplane.  
ISBN 978-3-86644-920-6
- Band 15 Christiane Neumann**  
Entwicklung einer Plattform zur individuellen Ansteuerung  
von Mikroventilen und Aktoren auf der Grundlage eines  
Phasenüberganges zum Einsatz in der Mikrofluidik.  
ISBN 978-3-86644-975-6
- Band 16 Julian Hartbaum**  
Magnetisches Nanoaktorsystem.  
ISBN 978-3-86644-981-7
- Band 17 Johannes Kenntner**  
Herstellung von Gitterstrukturen mit Aspektverhältnis 100 für die  
Phasenkontrastbildgebung in einem Talbot-Interferometer.  
ISBN 978-3-7315-0016-2
- Band 18 Kristina Kreppenhofer**  
Modular Biomicrofluidics - Mikrofluidikchips im Baukasten-  
system für Anwendungen aus der Zellbiologie.  
ISBN 978-3-7315-0036-0
- Band 19 Ansgar Waldbaur**  
Entwicklung eines maskenlosen Fotolithographiesystems  
zum Einsatz im Rapid Prototyping in der Mikrofluidik und  
zur gezielten Oberflächenfunktionalisierung.  
ISBN 978-3-7315-0119-0
- Band 20 Christof Megnin**  
Formgedächtnis-Mikroventile für eine fluidische Plattform.  
ISBN 978-3-7315-0121-3
- Band 21 Srinivasa Reddy Yeduru**  
Development of Microactuators Based on  
the Magnetic Shape Memory Effect.  
ISBN 978-3-7315-0125-1

- Band 22 Michael Röhrig**  
Fabrication and Analysis of Bio-Inspired Smart Surfaces.  
ISBN 978-3-7315-0163-3
- Band 23 Taleieh Rajabi**  
Entwicklung eines mikrofluidischen Zweikammer-  
Chipsystems mit integrierter Sensorik für die Anwendung  
in der Tumorforschung.  
ISBN 978-3-7315-0220-3
- Band 24 Frieder Märkle**  
Laserbasierte Verfahren zur Herstellung hochdichter  
Peptidarrays.  
ISBN 978-3-7315-0222-7
- Band 25 Tobias Meier**  
Magnetoresistive and Thermoresistive Scanning  
Probe Microscopy with Applications in Micro- and  
Nanotechnology.  
ISBN 978-3-7315-0253-1
- Band 26 Felix Marschall**  
Entwicklung eines Röntgenmikroskops für  
Photonenenergien von 15 keV bis 30 keV.  
ISBN 978-3-7315-0263-0
- Band 27 Leonardo Pires Carneiro**  
Development of an Electrochemical Biosensor Platform and a  
Suitable Low-Impedance Surface Modification Strategy.  
ISBN 978-3-7315-0272-2
- Band 28 Sebastian Mathias Schillo**  
Prozessentwicklung für die Automatisierung der Herstellung  
und Anwendung von hochdichten Peptidmicroarrays.  
ISBN 978-3-7315-0274-6



- Band 29** Nicole E. Steidle  
Micro- and Nanostructured Microfluidic Devices  
for Localized Protein Immobilization and Other  
Biomedical Applications.  
ISBN 978-3-7315-0297-5
- Band 30** Jochen Heneka  
Prozessentwicklung eines industrietauglichen Verfahrens  
zur Fertigung von vereinzelt LIGA-Mikrobauteilen.  
ISBN 978-3-7315-0326-2
- Band 31** Seung-Eun Kim  
Konzeption und prototypische Fertigung einer  
nicht-invasiven mikrofluidischen Plattform für die  
Elektrophysiologie (NIMEP) zur Zellenanalyse.  
ISBN 978-3-7315-0378-1
- Band 32** Elisabeth Wilhelm  
Entwicklung eines mikrofluidischen Brailledisplays.  
ISBN 978-3-7315-0385-9
- Band 33** Viktor Pinneker  
Entwicklung miniaturisierter Aktorsysteme basierend  
auf magnetischen Formgedächtnislegierungen.  
ISBN 978-3-7315-0500-6
- Band 34** Ali Caglar Özen  
Novel MRI Technologies for Structural and Functional  
Imaging of Tissues with Ultra-short  $T_2$  Values.  
ISBN 978-3-7315-0657-7
- Band 35** Anne Bäcker  
Veränderliche 3D Zellgerüstträger auf Cryogelbasis  
zur Kultivierung von Prostatakarzinomzellen.  
ISBN 978-3-7315-0676-8
- Band 36** Frieder Johannes Koch  
X-ray optics made by X-ray lithography:  
Process optimization and quality control.  
ISBN 978-3-7315-0679-9

- Band 37** Tobias Jörg Schröter  
Vergrößerung des Sehfeldes der Röntgen-Phasenkontrast-  
Bildgebung für die klinische Anwendung.  
ISBN 978-3-7315-0731-4
- Band 38** Felix Vüllers  
Bioinspired Superhydrophobic Nano- and Microstructured  
Surfaces for Drag Reduction and Optoelectronics.  
ISBN 978-3-7315-0816-8
- Band 39** Frederik Kotz  
Entwicklung neuer Materialien für die additive  
Fertigung und das Rapid Prototyping von Glas  
und Polymethylmethacrylat.  
ISBN 978-3-7315-0835-9
- Band 40** Michael Oldenburg  
Photon upconversion heterostructures made from  
surface-anchored metal-organic frameworks.  
ISBN 978-3-7315-0863-2
- Band 41** Elisa Kornemann  
Entwicklung einer Röntgenzoomlinse.  
ISBN 978-3-7315-0885-4
- Band 42** Hossein Davoodi  
NMR micro-detectors tailored for multinuclear and electro-  
chemistry lab-on-a-chip applications.  
ISBN 978-3-7315-1118-2



HOSSEIN DAVOODI

NMR micro-detectors tailored for multinuclear  
and electrochemistry lab-on-a-chip applications

Each individual isotope has a certain precessing frequency when exposed to a static magnetic field. Nevertheless, the actual magnetic field, which each nucleus experiences, depends on its chemical and physical environment. Thus, under different environmental conditions, the precessing frequency of the nucleus is slightly different. This feature can be used to “spy” on the chemical and physical properties of the medium. Nuclear magnetic resonance (NMR) relies on this principle to detect the precessing frequency of the nuclei under test. This work offers three solutions tailored to specific applications to overcome NMR challenges in micro-domain:

- One of NMR bottlenecks is the incompatibility of the technique with conductive elements. Because of their shielding properties, conductive elements affect the magnetic field link between the NMR sensor and the sample. As the first sub-topic of this work, different potential electrode designs are suggested and experimentally evaluated in order to overcome this challenge.
- As the second focus point, this work tackles multinuclear detection challenges. Therefore, the detection bandwidth is enlarged. The cost to be paid is lower power transfer between the sensor and transceiver. The penalty is evaluated and the sensor geometry is optimised to reduce the cost.
- In parallel, a low-cost, broadband insert is suggested to enhance the sensitivity of standard NMR coils when a small sample volume is available. This solution employs an add-on which focuses the coil field at the sample volume. Additionally, this insert flips the magnetic field.

ISSN 1869-5183

ISBN 978-3-7315-1118-2

Gedruckt auf FSC-zertifiziertem Papier

